DISSERTATION

Role of the Cu-O Defect in CdTe Solar Cells

Submitted by

Caroline R. Corwine

Department of Physics

In partial fulfillment of the requirements

For the Degree of Doctor of Philosophy

Colorado State University

Fort Collins, Colorado

Summer 2006

COLORADO STATE UNIVERSITY

June 16, 2006

WE HEREBY RECOMMEND THAT THE DISSERTATION PREPARED UNDER OUR SUPERVISION BY CAROLINE R. CORWINE ENTITLED ROLE OF THE CU-O DEFECT IN CDTE SOLAR CELLS BE ACCEPTED AS FULFILLING IN PART REQUIREMENTS FOR THE DEGREE OF DOCTOR OF PHILOSOPHY.

Graduate Committee

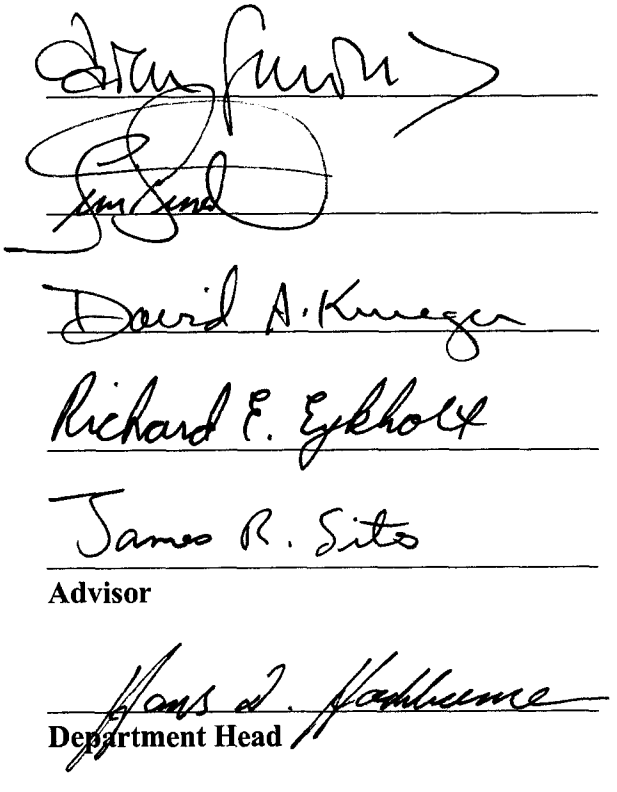

Advisor

Department Head

ABSTRACT OF DISSERTATION

Role of the Cu-O Defect Complex in CdTe Solar Cells

Thin-film CdTe is one of the leading materials used in photovoltaic (PV) solar cells. One way to improve device performance and stability is through understanding how various device processing steps alter defect states in the CdTe layer. Photoluminescence (PL) studies can be used to examine radiative defects in materials. This study uses low-temperature PL to probe the defects present in thin-film CdTe deposited for solar cells. One key defect seen in the thin-film CdTe was reproduced in single-crystal (sX) CdTe by systematic incorporation of known impurities in the thin-film growth process, hence demonstrating that both copper and oxygen were necessary for its formation.

Polycrystalline (pX) thin-film glass/SnO_2:F/CdS/CdTe structures were examined. The CdTe layer was grown via close-spaced sublimation (CSS), vapor transport deposition (VTD), and physical vapor deposition (PVD). After CdTe deposition, followed by a standard $CdCl_2$ treatment and a ZnTe:Cu back contact, a PL peak was seen at ~1.46 eV from the free back surface of all samples (1.456 eV for CSS and PVD, 1.460-1.463 eV for VTD). However, before the Cu-containing contact was added, this peak was not seen from the front of the CdTe (the CdS/CdTe junction region) in any device with CdTe thickness greater than 4 μm. The $CdCl_2$ treatment commonly used to increase CdTe grain size did not enhance or reduce the peak at ~1.46 eV relative to the rest of the PL spectrum. When the Cu-containing contact was applied, the PL spectra from both the front and back of the CdTe exhibited the peak at 1.456 eV.

The PL peak at ~1.46 eV was present in thin-film CdTe after deposition, when the dominant impurities are expected to be both Cu from the CdTe source material and O introduced in the chamber during growth to assist in CdTe film density. Since Cu and/or O appeared to be involved in this defect, PL studies were done with sX CdTe to distinguish between the separate effects of Cu or O and the combined effect of Cu and O. Photoluminescence on the sX samples revealed a unique transition at 1.456 eV, identical to the one seen in CSS thin-film CdTe, only when both Cu and O were introduced simultaneously. Theoretical calculations indicate that this PL line is likely a transition between the valence band and a Cu_i-O_{Te} donor complex 150 meV below the conduction band.

Formation of a Cu_i-O_{Te} donor complex was expected to limit the performance of the CdS/CdTe solar cell. However, this was difficult to observe in the prepared devices, likely because other beneficial processes occurred simultaneously, such as formation of Cu_{Cd} acceptors in the CdTe layer and improvement in the quality of the back contact by including Cu. It was possible to see the theoretical effects of this defect using AMPS-1D numerical simulations. The simulated J-V curves indicated that a donor level 150 meV from the conduction band would reduce the V_{oc}, hence reducing the overall device efficiency. Therefore, despite the lack of direct experimental evidence, it is very plausible that the Cu_i-O_{Te} defect observed with photoluminescence may serve to limit the possible attainable efficiency in CdS/CdTe solar cells.

Caroline R. Corwine
Physics Department
Colorado State University
Fort Collins, CO 80523
Summer 2006

ACKNOWLEDGEMENTS

My thanks go out to the many people who have contributed to this project. First I would like to thank my advisors, Jim Sites at Colorado State University (CSU) and Tim Gessert at the National Renewable Energy Laboratory (NREL), for their guidance during this thesis project. I would also like to thank the other members of my thesis committee for help with the thesis document. I would like to acknowledge Sam Demtsu's contribution to AMPS simulations and Tim Nagle's extra effort in reviewing thesis materials. I am grateful to other fellow graduate students working in photovoltaics at CSU, both past and present: Pam Johnson, Alex Pudov, Markus Gloeckler, Ana Kanevce, Jun Pan, and Alan Davies.

I received a lot of help from the members of the measurement and characterization team at NREL. Many thanks to Pat Dippo and Wyatt Metzger in the photoluminescence laboratory who taught me the intricacies of performing photoluminescence measurements as well as the art of interpreting the results. I would also like to thank Manuel Romero for cathodoluminescence measurements, Glenn Teeter and Craig Perkins for surface measurements, and Sally Asher for secondary ion mass spectrometry (SIMS).

I am grateful to Su-Hai Wei and Jingbo Li, who performed theoretical calculations for this project. They helped interpret the results and enhanced my understanding of how the theoretical calculations are done.

Many different people were involved in sample preparation. Anna Duda at NREL deposited Cu on the single-crystal samples. Thin-film polycrystalline materials were provided by: Ramesh Dhere at NREL, Brian McCandless at the Institute for Energy Conver-

sion (IEC), Chris Ferekides at the University of Southern Florida (USF), and W.S. Sampath, Al Enzenroth, and Kurt Barth in the materials engineering laboratory at CSU.

Funding for this project was provided by the U.S. Department of Energy under Contract No. DE-AC36-99GO10337 and by the NREL Thin Film Partnership under Subcontract No. XXL-5-44205-03.

I would like to thank my family and friends who have provided support and motivation during this long process.

To my husband, Dan: I am grateful for the love and happiness you have brought to my life. I don't know if I would have made it through without having you to go home to every night. Your encouragement and unconditional support have helped me through many rough patches.

To my parents: I am very thankful for your encouragement and emotional support over the years. No matter what happened, you were always proud of me. I think you were even more excited than I was when I got into graduate school and then again when I first became a published author. You have waited a long time for me to earn the title of doctor, and that time has finally arrived. I love you so much.

To Theo, Tiffany, Kristen & Tony, Kristina & Kevin, Sean & Shannon, Jenny & Richard, and countless others: I have valued your friendships over these past few years. You have helped to make my life enjoyable and full. Thank you for the fun times we've had together, and for helping me temporarily forget about physics so that I could relax. Finally, I would like to extend a heartfelt thanks to my "family" at Front Range Baptist

Church in Fort Collins. I was made to feel at home from my first visit, and I have appreciated the continued encouragement during my time in graduate school.

TABLE OF CONTENTS

LIST OF FIGURES

LIST OF TABLES

Chapter 1

Introduction

1.1 The Need for Solar Energy

Over the past two decades, it has become apparent that there is a need for renewable energy sources. The argument for renewables has increasingly focused on global warming caused by carbon dioxide emissions produced when fossil fuels are burned. One model predicts that, even if CO_2 emissions were stabilized at today's levels, the global temperature and sea level would continue to rise for another 50-100 years [1]. The substantial changes in climate are certainly a good reason to look for alternative energy sources. Economic and national security factors also make it desirable to significantly reduce the U.S. dependence on fossil fuels.

Although there are many kinds of renewable energy and each one will play an important role in replacing fossil fuels, one must consider the amount of energy required 50-100 years from now and whether the various technologies will be able to produce that amount of power. In a popular talk by Dr. Nate Lewis of the California Institute of Technology [2], the various renewable energy sources are discussed in terms of the available resource—e.g., land mass for windmills—and technological feasibility. He concludes that only photovoltaics are capable of contributing the required amount of power.

1.2 The Role of Thin-film Solar Cells

The push towards thin-film technology has been driven largely by predictions of future economic viability. Traditional single-crystal solar cells, such as Si and GaAs, demonstrate very high efficiencies (20-30%), but the production of crystalline material is expensive. The original reason thin-film materials were pursued was because they use much less material, which is directly related to the cost of production.

Two of the leading thin-film materials are CdTe and $CuInGaSe_2$, chosen because their direct bandgaps require a smaller absorption length than Si (requires less thickness for optimum performance). Studies during the past 40 years have also indicated that, for reasons not completely understood, these two materials can achieve performance levels in the 15-20% range while still containing significant amounts of impurity as well as numerous grain boundaries.

1.3 Progress in CdTe Solar Cells

Over the last 50 years, much effort has been put into developing high-efficiency, low-cost thin film polycrystalline CdTe/CdS solar cell devices. CdTe is a nearly ideal material for terrestrial solar cell production, as its band gap of 1.45 eV (room temperature) yields the maximum theoretical efficiency for a solar cell, about 29%. The current record one-of-a-kind laboratory research cell was fabricated in 2000 and has an efficiency of 16.5% [3]. The best laboratory cell efficiencies range from 14 to 16.5%, the typical research cells from 10 to 14%, and typical modules from 7 to 10%. Some of the processes that have significantly

raised the efficiencies of these cells include the introduction of O_2 during the CdTe growth, a $CdCl_2$ treatment prior to contacting the CdTe, and a back-contact process that contains Cu. All of these processes are necessary to obtain research cells with efficiencies above 10%. However, there is presently little agreement regarding how these processes, either individually or collectively, affect the defect states in the CdTe layer to enhance device performance.

Thin-film CdS/CdTe solar cells are heteroface photodiodes (see Figure 1.1). CdS is

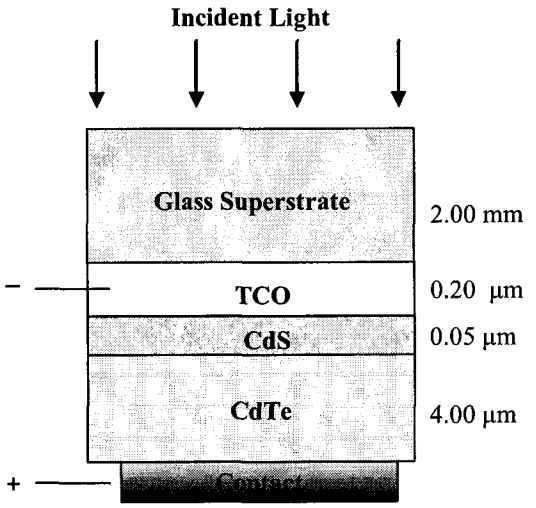

Figure 1.1. Device structure of a CdS/CdTe heteroface solar cell.

chosen mainly because of its high band gap (E_g = 2.4 eV at room temperature) compared to that of CdTe (E_g = 1.47 eV at room temperature). The bulk of the photons from the sun are below 2.4 eV, thus are not absorbed in the CdS layer. These photons pass through to the CdTe layer for collection. Hence, the CdS layer is often referred to as the "window layer." In addition to a high band gap, a good window layer should have lattice constant(s) similar to those in the absorber layer, since lattice mismatch between the window and absorber

layers creates interface defect states, and is a source for losses in device performance. Materials other than CdS have been investigated for use as a window layer to CdTe (such as ZnO and ZnSe [4, 5]), but the devices with CdS performed best. This was somewhat surprising, as the lattice mismatch between CdS and CdTe is 10% (a_{CdS} = 5.82 Å, a_{CdTe}= 6.48 Å) [6], which is a significant amount with respect to formation of recombination sites at the interface. However, the CdS and CdTe layers tend to intermix near the interface during device preparation, which creates a gradient in the film's lattice constant. This has been credited with an improvement in device performance, possibly because the large lattice mismatch is accounted for within a large volume, thereby reducing its detrimental effects [7].

1.3.1 Processing Techniques for CdS/CdTe Solar Cell Fabrication

CdS/CdTe solar cells were originally grown in a substrate configuration, where Molybdenum foil was used as the substrate and acted as the back contact to the device [8] (see Figure 1.2a). In this configuration, the CdTe layer was grown in two stages: a very thin layer of CdTe was deposited onto the Molybdenum via evaporation (0.2-0.5 μm), followed by a thick CdTe layer (10-20 μm) deposited via a high-temperature gas transport method. Then a graded CdS_xTe_{1-x} layer —starting with CdTe and ending with CdS — was evaporated. Finally, an indium grid contact was applied. Two of the major problems with this type of cell fabrication were difficulty in doping the CdTe and a poor back contact formation [8]. One of the major reasons for switching to the superstrate configuration shown in Figure 1.2b was to gain better access to the back contact region with hopes of improving

this contact. Other reasons include: historic availability of glass coated with a Transparent Conducting Oxide (TCO); historic use of solution-grown CdS; and the advantageous formation of CdS_xTe_{1-x} when CdTe is grown at high temperatures onto CdS.

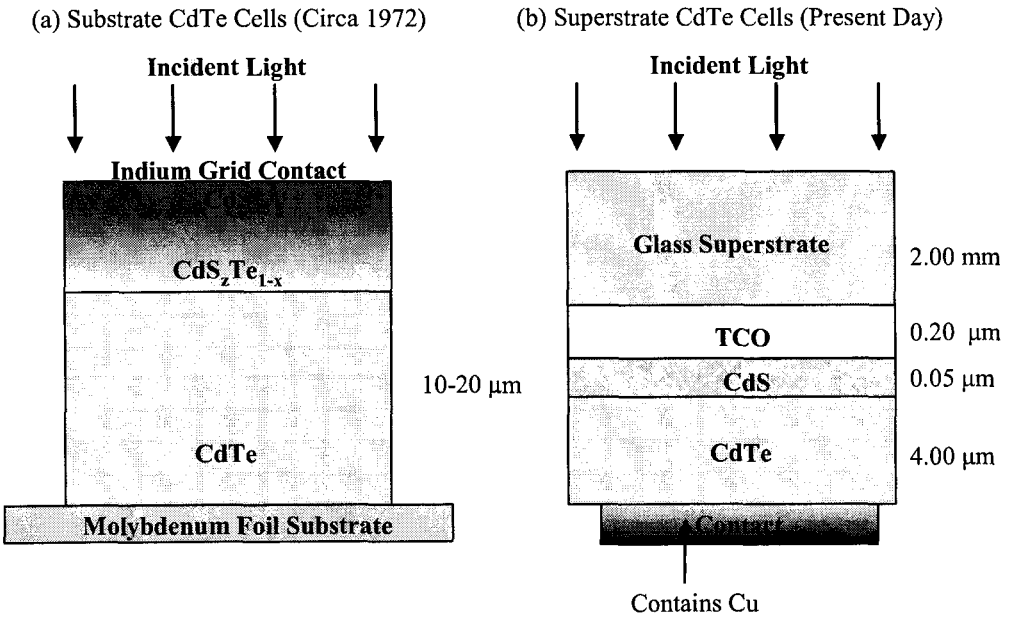

Figure 1.2. Schematic drawing of the CdTe/CdS solar cell structures: (a) Substrate structures used in earlier devices, and (b) superstrate structures used in today's devices.

The currently-used device fabrication technique begins with depositing a TCO, typically SnO_2:F, onto soda-lime glass (many manufacturers buy pre-coated glass). The purpose of the TCO is to collect and laterally transport current at the front side of the device. The n-CdS layer is deposited next, followed by the CdTe layer. Common commercial growth methods of CdS and CdTe are vapor transport deposition (VTD, 600°C), close-spaced sublimation (CSS, 600°C), and physical vapor deposition (PVD, 250°C). A $CdCl_2$ treatment (described below) is performed on the CdTe layer. Finally, a series of processes are used to form the back contact.

The development of particular CdTe, $CdCl_2$, and the back contact processes has primarily been empirical, with the focus on finding processing technique combinations that increase final device efficiency. Efforts to understand the effect of each processing step is complicated because probing the electrical operation of the device is possible only when all process steps are completed. The details of each CdTe processing step, as well as what the community understands about each step, are discussed in the following sections.

1.3.1.1 O_2 Use During Growth of Thin-film CdTe

An oxygen-containing atmosphere is commonly used during the CdTe growth process when making solar cell devices, regardless of the growth method — CSS, VTD, or PVD. For these films, oxygen is not only unavoidable, but is often deliberately introduced to improve device performance. The CSS process is performed with the CdTe source and the glass superstrate near to 600°C (source at 660°C, superstrate at 620°C) [9]. The VTD process holds the source at 800°C and the glass at 600°C. The PVD growth uses the lowest temperatures, with the deposition performed at 200°C.

Studies have shown that O_2 can alter the characteristics of thin-film CdTe during growth. Without O_2, the CdTe grains are very large, and there are gaps between the grains, often called pinholes, that can go from the free CdTe surface to the CdS film [10]. These pinholes are known to create shunt paths during some back contact processes [9]. O_2 produces a denser film by stimulating the growth of smaller grains in the film. Oxygen is also known to provide significant benefit during the post-growth treatment with $CdCl_2$. However, the reason for these benefits are not clear.

1.3.1.2 $CdCl_2$ Treatment of CdS/CdTe Devices

After the CdTe layer has been grown, the $CdCl_2$ treatment is performed. This treatment can be done with either $CdCl_2$ in solution or with $CdCl_2$ vapor. A typical liquid $CdCl_2$ treatment consists of dipping the CdS/CdTe solar cell in a saturated methanol:$CdCl_2$ solution for about 30 s then annealing in an "air-like" ambient (80% N_2 / 20% O_2) at 400–450°C for 30 min [9]. The typical vapor $CdCl_2$ treatment is performed in a vacuum chamber. $CdCl_2$ powder or a glass slide coated with $CdCl_2$ is placed in close proximity to the CdS/CdTe sample, sometimes in a CSS configuration. The $CdCl_2$ slide is heated in a He/O_2 atmosphere for 8 min at 400°C. The vapor $CdCl_2$ treatment is considered more reproducible because the $CdCl_2$ dose and atmosphere can be controlled more accurately. However, the liquid treatment may have industrial advantages because it can be performed at ambient pressure.

The use of a $CdCl_2$ treatment has been shown to be crucial in developing high-efficiency CdS/CdTe solar cells. $CdCl_2$ is unique in its improvement in device efficiency, and other chloride treatments, such as $MnCl_2$, do not have the same positive effect on device parameters as does $CdCl_2$ [11]. One of the commonly reported effects of the $CdCl_2$ treatment is the recrystallization of small-grain films such as those produced by CBD-, PVD-, and MOCVD-grown CdTe [7]. The recrystallized structure has larger grains, which would decrease the effect of grain boundaries and reduce the lattice strain. For larger-grain materials, such as CSS- and VTD-grown CdTe, there are significant changes in grain boundaries, but no evidence of recrystallization [12]. The $CdCl_2$ treatment has also been credited with facilitating the interfacial mixing of the CdTe and CdS layers [7], which may assist with

lattice matching. Recrystallization has been reported in various studies using different growth methods, while the enhanced interfacial mixing of CdS and CdTe have been observed only in PVD-grown devices [7, 13, 14]. Heat treatment alone also leads to improved device performance, but not to the extent observed following the $CdCl_2$ treatment [13, 15].

In one thin-film CdTe study [7], it was noted that the $CdCl_2$ treatment increases the minority carrier lifetime. The minority carrier lifetime, in this case, was measured using time-resolved photoluminescence (TRPL). This increase in minority carrier lifetime was attributed to a decrease in the deep defect levels, although no direct evidence was presented. It is interesting to note that the results from TRPL showed an increased minority carrier lifetime for all samples treated with $CdCl_2$, regardless of whether or not the samples recrystallized. This suggests that the improvement in device performance following a $CdCl_2$ treatment is primarily due to changes in material properties beyond the often-observed structural modifications.

1.3.1.3 Back Contact Processes

Forming a back contact on a CdTe device is complicated by the difficulty in making ohmic metal contacts to p-type CdTe. For the case of simple Mott-Schottky theory, whether a metal contact forms an ohmic contact or a barrier to a semiconductor depends on the work function of the metal, ϕ_m, and the work function and electron affinity of the semiconductor, ϕ_s and χ_s, respectively (note that interfacial reactions and Fermi level pinning may negate these simple rules of Mott-Schottky theory). When a metal is connected to a semiconductor, band bending occurs [16]. Figure 1.3 shows the band bending for a p-type

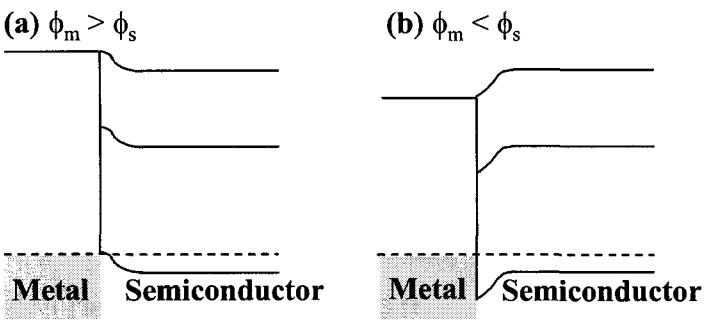

Figure 1.3. Metal-semiconductor (MS) diodes for p-type semiconductors. (a) For the case $\phi_m \rangle \phi_s$ the metal forms an ohmic contact to the seimconductor. (b) For the case $\phi_m \langle \phi_s$ the metal forms a barrier for holes.

semiconductor for the cases $\phi_m > \phi_s$ and $\phi_m < \phi_s$. For the case $\phi_m > \phi_s$ (Figure 1.3a), the bands in the semiconductor bend up, allowing holes to flow into the metal, thus forming an ohmic contact. For the case $\phi_m < \phi_s$ (Figure 1.3b), the bands in the semiconductor bend down, creating a barrier to holes. CdTe has large values of ϕ_s and χ_s, and most metals satisfy the condition $\phi_m < \phi_s$. Hence, most contacts to p-type CdTe are expected to form barriers.

The back contact processes that have been developed for CdTe are designed to reduce the downward band-bending in CdTe so that the barrier to holes is reduced and current can be collected. There are three basic approaches, which are shown pictorially in Figure 1.4: (I) Dope the back of the CdTe with a p-type dopant, such as Cu, which reduces the band bending in the CdTe; (II) Create a layer with a smaller band gap, which narrows the barrier and reduces the barrier height; (III) Create a highly-doped layer of another material with a matching valence band, such that no band-bending occurs in the CdTe layer, but occurs instead in the subsequent layer, producing a narrow but steep barrier to the metal. Strategy (I) can be used alone, but is typically incorporated in conjunction with strategy

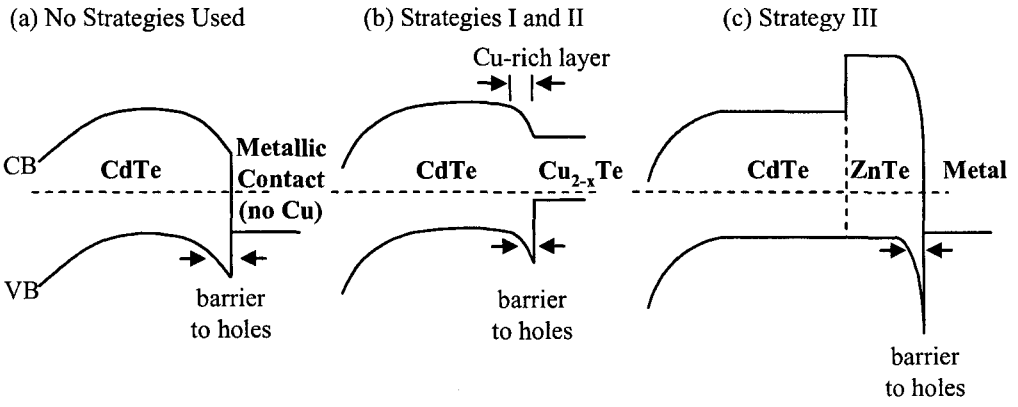

Figure 1.4. Schematic drawing of the band diagram for CdS/CdTe solar cells using different back contact strategies. (a) No strategies used; (b) strategies I and II, to use an etchant and to dope the back; (c) strategy III, to use a material with matching valence band.

(II); for these two strategies, the holes are collected via thermionic emission [17, 18]. In approach (III), holes are collected primarily by tunnelling through the narrow barrier into the metal [19]. Although a wide variety of processes are used to produce psuedo-ohmic back contacts for thin-film CdS/CdTe PV devices, they all fall into method I, III, or a combination of I and II. Representative details of all processes (except for those by the Industrial VTD partner) are listed in Table 1.1, which is reproduced from Reference [20].

The deposited Colorado State University (CSU) and evaporated University of Toledo (UT) contacts are the only methods that rely solely on CdTe doping to create a good contact. For these — and, in fact for nearly all contact processes — Cu is used as the dopant, which can form Cu_{Cd}, a relatively shallow acceptor [21], which can serve to narrow the barrier to holes. The use of Cu as part of the back contact process dates back to work by Nakayama *et al* [22], where the CdTe was dipped into a hot Cu ion solution. Studies have shown that including Cu in the back contact, up to a certain amount, improves device performance,

but "too much" Cu can decrease the device efficiency [23, 24]. This decrease in device performance is presumably due to either formation of shunt paths, an insufficiently wide depletion width, formation of acceptors in CdS, or the formation of compensating defects in CdTe (i.e., formation of Cu-related donor levels in the CdTe) [25, 26].

	Anneal (Post $CdCl_2$)	**Etch**	**Contact**
CSU - deposited (I)	400°C, 2 min	–	Vapor deposition of Cu compound, Spray C/Ni
UT - Evaporated (I)	–	–	Evap. 3 nm Cu, 20 nm Au, 150°C/45 min air
IEC - Evaporated (I, II)	H_2 + Te Vapor	–	Evap. 2 - 10 nm Cu, HT 200°C, C Ink, 100°C anneal
Canrom - Paste (I, II)	420°C	NP	Cu evaporation, Graphite/Ag paste
NREL - Paste (I, II)	–	NP	Paste C:HgTe:CuTe, 260-280°C 25-30 min He, Ag paste
USF - Paste (I, II)	400°C, 25 min	0.01% BrMe	Paste C:HgTe:CuTe, 260-280°C 25-30 min He, Ag paste
CSM - ZnTe (III)	410°C 30 min Ar	0.015% BrMe	0.7 nm Cu, 50 nm ZnTe, 220°C 4 min, 50 nm Au, cool
NREL - ZnTe (III)	–	–	Ar ion beam, RF sputter ZnTe:Cu (360°C), Ti (DC sputter)
UT - ZnTe (III)	–	–	RF sputter ZnTe:N, HCL etch, DC sputter Ni, 200°C in air

Table 1.1. Different back contact processes used at various institutions. Parentheses indicate whether method I, II, or III is used to make good contact.

All paste contacts and the IEC evaporated contact use both CdTe doping and the formation of a thin layer with smaller band gap to improve the back contact collection. The IEC evaporated contact uses an anneal step in H_2 + Te that serves to remove oxides as well as to create an elemental Te layer at the back of the contact. When Cu from the contact step diffuses from the paste, some will create Cu_{Cd} acceptors in CdTe, but some will also combine with the Te layer to create a distinct $Cu_xTe_{(1-x)}$ layer (E_g = 1.3 eV). The paste contact processes also create a CuTe layer, but it is achieved by first chemically etching the CdTe to create a Te-rich layer on the CdTe back surface [9, 27–29], and then applying the

paste, which includes Cu. The commonly-used etches are nitric phosphoric acid (NP) and 0.5 - 3% bromine methanol (BrMe). The thickness of the Te layer (or Te-rich layer) is roughly 10 nm for the BrMe etch [30, 31] and ›100 nm for the NP etch [32]. The NP etch also etches along grain boundaries, leaving them Te-enriched. Many benefits have been ascribed these etches, including a change in the surface pinning of the Fermi level when metals are contacted to CdTe [27], decrease in the contact resistance when the contact is formed after etching [32], removal of $CdCl_2$ residues, and reduction of the CdTe thickness. The NP etch also increases the surface area of the CdTe (increases surface roughness), which reduces the overall resistance of the contact, even when the specific resistance (Ω cm^2) is unchanged.

The ZnTe contact processes make use mostly of the matching valence band strategy, although it is presumed that there is some Cu doping in the CdTe for these processes. The CSM processes uses a light BrMe etch, mostly to remove $CdCl_2$ residues, and the NREL process uses ion beam milling prior to contacting to start with a clean surface.

1.4 Fundamentals of Solar Cell Operation

In solar-cell technology, the key to affordability is the reduction in the cost per kWh. There are two different approaches to reduce the cost per kWh: (1) decrease the cost of production, or (2) increase the efficiency of the solar cell, which increases the kW rating. Ideally, both strategies should be used to minimize cost. Thin-film technology uses thin (2-8 μm absorber layer) polycrystalline materials that are cheaper to produce than their single-crystal counterparts. This reduction in cost, however, is not enough to reduce the

cost per kWh to the point where solar cells can compete with other (nonrenewable) sources of energy. Thus, the efficiency of these devices must be increased such that solar energy can compete in a consumer market.

The efficiency of a solar cell is determined by $\eta = P_{out}/P_{in}$, where P_{out} is the electrical power generated per unit area and P_{in} is the power density of the solar insolation. The value for P_{in} is well-defined for earth-orbiting satellites, but varies considerably for terrestrial applications. In space, the solar insolation outside the earth's atmosphere (at the mean earth-sun distance) is referred to as air mass zero (AM0) radiation, and is shown in Figure 1.5 (from Ref. [33]). This radiation intensity is not quite the same as for the case of an ideal black body emitting at 6000 K. At the earth's surface, the solar radiation intensity is reduced from AM0 due to scattering and absorption that occur in the atmosphere [34]. The amount by which the radiation is reduced will depend on the length of the optical path through the atmosphere, which depends on the sun's location in the sky (this will be determined by the time of day, time of year, and latitude of the observer). When the sun is directly overhead at sea level and without clouds, the radiation will be at a maximum; this is referred to as air mass one (AM1) radiation. When the sun is at other locations in the sky, the air mass is defined as $air\ mass = \frac{1}{\cos\theta}$, where $\theta = 0$ corresponds to the sun being directly overhead. For terrestrial applications, AM1.5 (48° from overhead) has been established as the standard solar insolation (see Figure 1.5), and this corresponds to a power density of $P_{in} = 100$ mW/cm^2 [33].

The output power density, P_{out}, of the solar cell is determined from the current-voltage (JV) characteristics of a solar cell, as shown in Figure 1.6. Note that the maximum P_{out} is

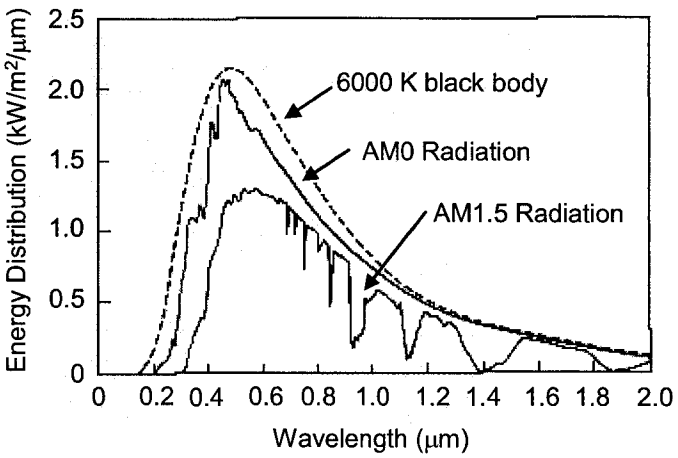

Figure 1.5. Spectral distribution of sunlight for the cases AM0 and AM1.5. Also shown is the radition from an ideal black body at 6000 K.

$P_{\max}$. The maximum power can also be determined by the standard JV parameters J_{sc}, V_{oc}, and FF (fill factor) by $P_{\max} = J_{\max} * V_{\max} = J_{sc} * V_{oc} * FF$, where J_{sc} is the short-circuit current density (V=0), V_{oc} is the open-circuit voltage (J=0), and FF $= J_{\max}V_{\max}/J_{sc}V_{oc}$. The ideal diode equation for solar cells has the form:

$$J = J_o(e^{qV/AkT} - 1) - J_L \tag{1.1}$$

Here, J_L is the photocurrent, or current that is produced when light excites electron-hole pairs close to the junction that can be collected (see Figure 1.7); J_o is the reverse saturation current of the diode; and A is the diode quality factor (or diode ideality factor), where an ideal diode has A = 1 ($1 < A < 2$). Using the definitions that J_{sc} corresponds to V = 0 and V_{oc} corresponds to J = 0,

$$J_{sc} = -J_L \tag{1.2}$$

and

$$V_{oc} = \frac{AkT}{q} \ln\left(\frac{J_L}{Jo} + 1\right) \tag{1.3}$$

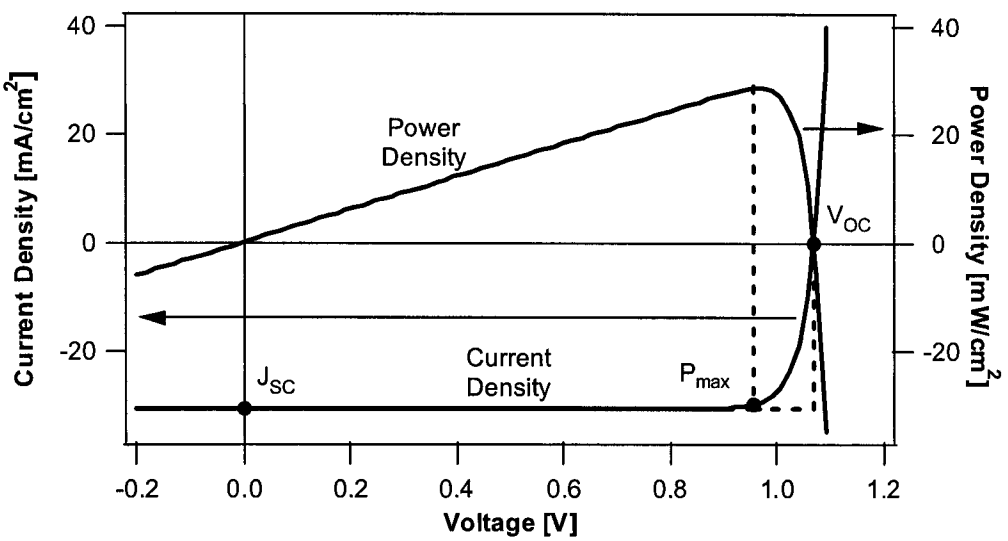

Figure 1.6. Typical J-V curve, showing the standard parameters used for performance evaluation.

When striving to increase efficiency, effort is directed at increasing the photovoltaic parameters J_{sc}, V_{oc}, and FF. All of these parameters are affected by defect states in the solar cell material.

1.4.1 The Impact of Defects on Device Performance

Defects are usually classified as shallow, deep, or intermediate. Shallow defects are defined as defects within a few kT of the band edge, such that a hole [electron] from an acceptor [donor] has a high probability of being thermally excited into the valence [conduction] band at typical device operating temperatures. Deep defects, sometimes called mid-gap defects, are located near the middle of the band gap and typically act as recombination sites for electrons and holes. Intermediate defects are any defect with ionization energy between that for shallow and deep levels.

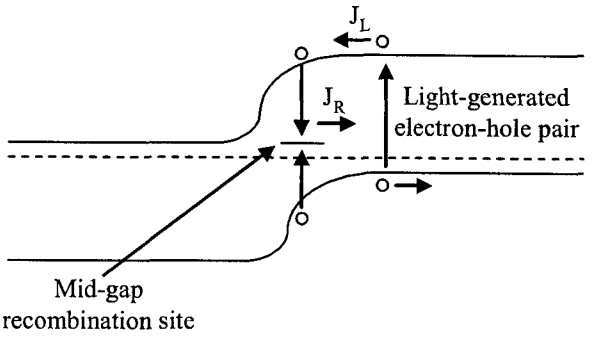

Figure 1.7. Schematic drawing of the photocurrent, J_L, produced when light is incident on a p-n junction. Also represented is the recombination current, J_R, produced when an electron and hole pair recombine at a mid-gap state within the junction.

1.4.1.1 Shallow Defects

When discussing shallow defects, one must look at both donors and acceptors. The relative effects of a donor or acceptor will depend on whether the semiconductor is n- or p-type. For simplicity, consider the case of a p-type semiconductor. An increase in the number of shallow acceptors will increase the number of holes in the valence band and increase the carrier concentration. If all other factors are held constant, this will decrease J_o (the reverse saturation current of the diode). From equations 1.1 & 1.3, a decrease in J_o will increase V_{oc} but leave J_{sc} unchanged, and the efficiency of the device will increase. Conversely, a shallow donor level added to p-type material will increase J_o, which lowers V_{oc}, and reduces device efficiency.

1.4.1.2 Deep Defects

Deep (mid-gap) defects in the junction region act as recombination centers for holes and electrons (see Figure 1.7). This causes a recombination current, J_R, in the direction

opposite to the photocurrent, and this recombination current is added into the ideal expression for total current given in Equation 1.1:

$$J = J_o(e^{qV/AkT} - 1) + J_R - J_L, \text{ where } J_R = J'_o(e^{qV/2AkT} - 1) \tag{1.4}$$

or

$$J = J_o(e^{qV/AkT} - 1) + J'_o(e^{qV/2AkT} - 1) - J_L \tag{1.5}$$

where

$$J_L = -J_{sc} \tag{1.6}$$

Note that $J_R = 0$ at $V = 0$, so in theory J_{sc} is not affected by the recombination current (in reality, however, there may be a change in the depletion width, which would affect J_{sc}). The V_{oc} will be slightly affected by the presence of a recombination current. Solving Equation (1.5) when J=0:

$$0 = J_o e^{qV_{oc}/AkT} - J_o + J'_o e^{qV_{oc}/2AkT} - J'_o - J_L \tag{1.7}$$

$$0 = e^{qV_{oc}/AkT} * (J_o + J'_o e^{-qVoc/2AkT}) - J_o - J'_o - J_L$$

$$e^{qV_{oc}/AkT} = \frac{J_L + J_o + J'_o}{J_o + J'_o e^{-qVoc/2AkT}}$$

Hence, the expression for V_{oc} with recombination current is:

$$V_{oc} = \frac{AkT}{q} \ln\left(\frac{J_L + J_o + J'_o}{J_o + J'_o e^{-qVoc/2AkT}}\right) \tag{1.8}$$

It is important to note that, while J_L is the order of 10 mA/cm^2, J'_o and J_o are typically the order of 10^{-7} - 10^{-11} mA/cm^2. Thus, the numerator of the parentheses changes very little with increasing J'_o, but the denominator increases as J'_o increases, which slightly lowers the overall V_{oc}.

The current-voltage parameter that will be most effected by the recombination current arising from deep (mid-gap) defect states is the FF. The shape of the bend in the JV curve (Figure 1.6) is influenced by the diode ideality factor, A. For A values close to 1, the bend of the curve is fairly "square," producing large values for J_{max} and V_{max}. However, larger values of A will cause the curve to be less "square" and the values for J_{max} and V_{max} will be smaller. The A factor is governed by the types of recombination occurring in the device. As the amount of recombination via mid-gap states increases, the value for A will also increase, which will cause losses in FF (FF = $P_{\max}V_{\max}/J_{sc}V_{oc}$).

1.4.1.3 Intermediate Defects

Defects with activation energies intermediate to the shallow and deep defects have some probability that they will ionize to the band, adding to the V_{oc} and J_{sc}, and some probability that they will act as recombination centers, decreasing V_{oc}. Although both ionization and recombination can occur for intermediate defects, the relative probability of the two mechanisms will depend on the ionization energy of the defect. A defect with energy closer to that of a shallow defect (smaller ionization energy) will be more likely to ionize than to act as a recombination center. Conversely, a defect with energy closer to mid-gap (larger ionization energy) is more likely to act as a recombination center than to ionize to the band, and would tend to lower FF and V_{oc}.

Defects in a solar cell can greatly influence its efficiency, and hence identification of such defects is important. Identifying a defect is a key step to potentially increasing device efficiency. This defect must also be related to solar-cell performance and linked

to the process that introduced this defect. If the defect proves to be detrimental to device operation, then it may be necessary to change the process to eliminate or mitigate that defect. Although it is nontrivial to change the processing techniques to remove a defect without harming performance through some other mechanism, it is important to take that first step and identify the defects introduced by that process.

Chapter 2

Photoluminescence (PL)

2.1 The Basics of PL

Photoluminescence (PL) is a technique which is commonly used to study defect states in semiconductors, and is the primary measurement used in this thesis. Although the interpretation of PL can be quite complicated, the basic concept of how it works can be explained using conservation of energy and momentum. CdTe is a direct band gap semiconductor, which means that its conduction band minimum (CBM) and valence band maximum (VBM) both occur at $k = 0$, as shown schematically in Figure 2.1, where $\hbar k$ is momentum. When light with energy $E > E_g$ is incident on a semiconduc-

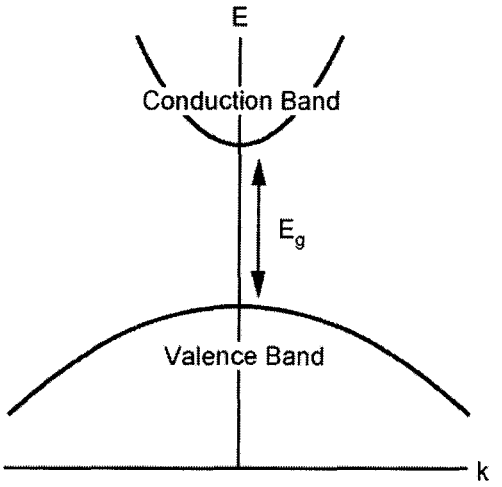

Figure 2.1. Energy versus momentum plot of the conduction and valence bands for a direct band gap semiconductor.

tor, the energy from one photon may be transferred to one electron. The energy from the photon gives the electron enough energy to be excited into the conduction band, leaving a hole in the valence band. The electron in the conduction band and hole in the valence band are collectively referred to as an electron-hole pair. After the electron-hole pairs are excited, they will recombine in order to obtain a lower-energy state. This recombination can occur via a variety of paths, the simplest of which is band-to-band recombination. However, let us consider the case where an electron moves from the conduction band to a state within the gap. As the electron makes this transition, the electron loses energy. This energy must be transferred to some other particle, typically either a photon or a phonon. Transitions that emit photons are referred to as radiative processes, and transitions that emit only phonons are nonradiative processes. Additionally, there are some transitions that emit both photons and phonons.

Because CdTe is a direct-bandgap material, the electron transitions will occur at $k = 0$ (see Figure 2.1), thus the total momentum of all particles created during the transition must add to zero. At energies on the scale of 1 eV, a photon has momentum $\hbar k = E/c \sim 10^{-27}$ kg*m/s and a phonon has momentum $\hbar k = E/v_{sound} \sim 10^{-22}$ kg*m/s. Since the photon momentum is 5 orders of magnitude smaller than that for a phonon, its momentum can be approximated as zero, and the phonon will have non-zero momentum. Hence, any transition that emits phonons must create more than one phonon to satisfy $k_{net} = 0$, whereas only one photon is required to conserve both energy and momentum. The energy of this one photon is equal to the change in energy, or transition energy, of the electron:

$$E_{photon} = \Delta E_{electron} \tag{2.1}$$

where $\Delta E_{electron}$ is the transition energy. Examples of these types of transitions are band-to-band recombination and band-to-defect recombination. Band-to-band transitions, as the name suggests, occur when an electron in the conductions band moves *directly* to the valence band to recombine with a hole. Using Equation 2.1, the photon energy of band-to-band recombination is:

$$\text{Band-to-band: } E_{photon(BB)} = E_g \tag{2.2}$$

where E_g is the band gap of the material at the measurement temperature.

Band-to-defect transitions occur when either an electron in the conduction band transitions to an acceptor state (CB-A) or when an electron from a donor state transitions into the valence band (D-VB). The photon energy for these transitions can be written as:

$$\text{CB-A: } E_{photon(CBA)} = E_g - E_A \tag{2.3}$$

$$\text{D-VB: } E_{photon(DVB)} = E_g - E_D \tag{2.4}$$

where E_A and E_D are the activation energies of the donor and acceptor (energy measured from the valence and conduction band, respectively). These donor and acceptor states can be due to a single defect, such as the direct substitution of Cu on Cd in CdTe (written as Cu_{Cd}), or they can be what are referred to as defect complexes. A defect complex is comprised of at least two defects that are formed in neighboring lattice sites and have a strong binding energy, such that it is difficult to separate the two defects. When this occurs, the two bound defects will act as one defect. These strong binding energies usually require that one defect have a net negative charge and the other have a net positive charge. However, isovalent defects can also combine with other species to form a complex, provided

the atomic radius of the substituting species is much different than the atom for which it is substituting. One example of a defect complex seen in CdTe is what is commonly referred to as the chlorine A-center, or V_{Cd}-Cl_{Te}. If these two species acted separately, V_{Cd} would act as an acceptor (net positive) with $E_A = 130$ meV and Cl_{Te} would act as a donor (net negative) with $E_D = 350$ meV [21]. The resulting complex is expected to be an acceptor state with $E_A = 140$ meV [21,35].

A transition between a donor and an acceptor has a slightly different energy than that in Equation 2.1. In this case, there is an energy arising from the coulomb interaction between the negatively-charged donor and the positively-charged acceptor states, and this must be accounted for with energy conservation. For a donor-acceptor pair (DAP) transition,

$$E_{photon(DAP)} = E_g - E_D - E_A - \frac{q_A q_D}{4\pi\epsilon r} \tag{2.5}$$

where q_A and q_D are the charge of the acceptor and donor, respectively, and r is the spacing between the charges. Note that $q_D < 0$ and $q_A > 0$, making the coulomb interaction energy term add to the transition energy, which usually increases the energy of the PL transition by a few meV. Since the coulomb interaction energy depends inversely on the spacing between defects r, this term will play a larger role when the two defects are closer in proximity to one another.

Another type of transition is the exciton. Excitons are formed only at low temperatures, and can be free or bound to an atom in the lattice. A free exciton (FE) is created when a hole from the valence band and an electron from the conduction band begin to orbit one another, which reduces the energy between the electron and hole by the energy of

the coulomb interaction between the two. The exciton state is unstable, and the electron and hole will quickly recombine, giving off a photon. The principle behind a bound exciton (BE) is similar, except that either the electron is bound to a neutral donor or the hole is bound to a neutral acceptor. In the case of a donor-related BE, a hole orbits around the neutral donor and electron. In the second case, an electron orbits around the neutral acceptor and hole, creating an acceptor-related BE. In both the donor-related and acceptor-related cases, the bound exciton would have a transition energy this is lower than that for the free exciton. This occurs because there is also some binding energy between the atom and the electron or hole orbiting it, and the free exciton energy will be reduced by this amount. The general expression for an exciton transition is:

$$\text{Exciton: } E_{photon(Exc)} = \Delta E_{exc} \tag{2.6}$$

The value for ΔE_{exc} for a free exciton can be calculated rather easily since it is simply the difference between the band gap and the coulomb interaction between the hole and electron. Using a quasi-hydrogenic model (see Appendix A), the calculated coulomb interaction energy between the electron and hole in CdTe is 12 meV, so that $E_{FE} = 1.593$ eV at 4 K (CdTe E_g = 1.606 eV at 4 K). It is not as straightforward to calculate the transition energy of bound exciton states since many lattice points exist for binding.

Photoluminescence measures the spectrum of photons produced when the excited electrons recombine with holes, and the energy at which the peaks occur is an indication of the types of transitions taking place during this recombination process. Figure 2.2 shows the possible types of PL transitions. The types of transitions seen in PL depend greatly on the temperature at which PL is taken. For example, at room temperature, the PL is typically

dominated by band-to-band recombination because all the shallow impurities are ionized [36]. The resulting room-temperature PL would show a broad peak centered at approximately the room-temperature band gap. However, at sufficiently low temperatures, carriers are frozen on impurities, making it possible to observe transitions to and/or from these defects in the PL signal. There are certain transitions, including one discussed at length in this thesis, that are only seen at temperatures of less than 40 K.

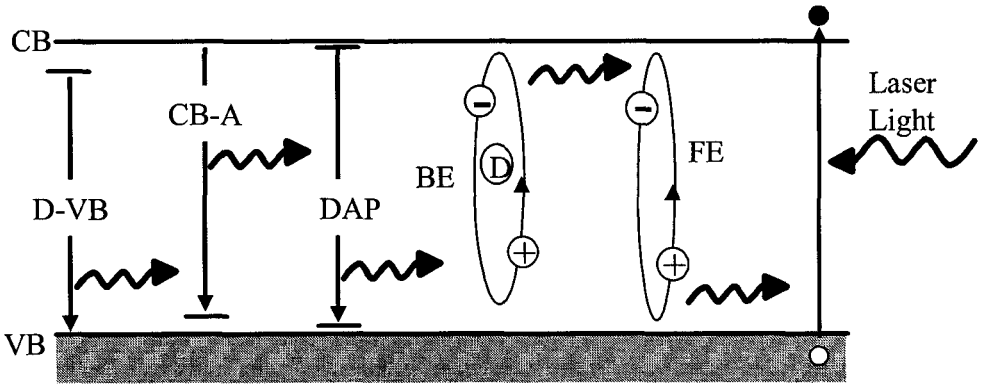

Figure 2.2. Schematic drawing of possible radiative transitions that can occur when excited electron-hole pairs recombine.

Figure 2.3a shows examples of the types of transitions that may be observed in PL. Each transition has a Gaussian-like distribution centered at the PL energy. This shape arises from the fact that each defect is not discrete, but has a Gaussian distribution of possible energies. PL measures the photon energies given off during the various transitions that occur after laser excitation. The excitonic PL transitions FE and BE are close to the band gap of 1.606 eV (at 4 K in CdTe), whereas the transitions involving a donor and/or acceptor have energies significantly less than the band gap. In general, the D-VB, CB-A, and DAP transitions could have any energy less than that for excitons, and the peaks in the PL signal

are not necessarily in the order shown in Figure 2.3a. Note that the D-VB transition in this figure exhibits peaks shifted by an integral number of longitudinal optical (LO) phonon energies. These shifted peaks are referred to as LO phonon replicas (see Section 2.2). In principal all transitions could have phonon replicas. For clarity, they are only shown here for one transition. The main transition, labeled as D-VB, is often referred to as the zero phonon line (ZPL). Figure 2.3b is the PL signal corresponding to the transitions shown in Figure 2.3a, and is the sum of all Gaussian distributions.

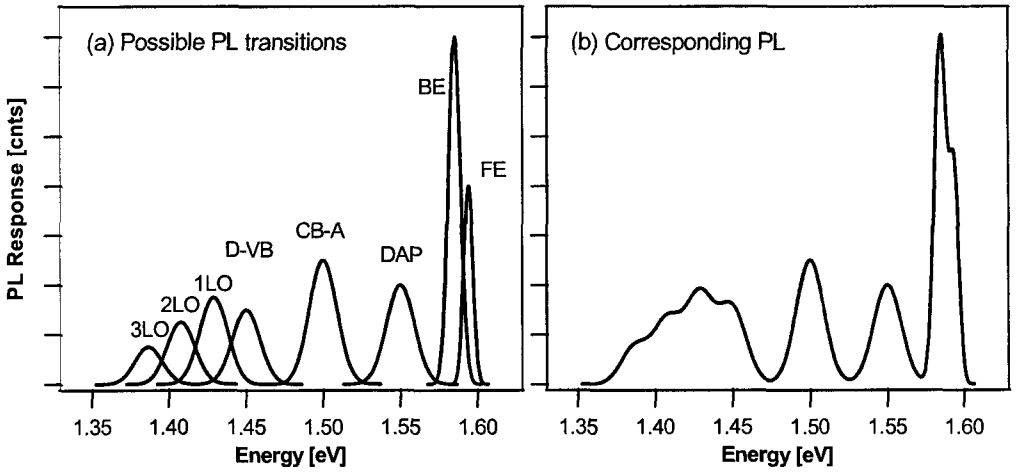

Figure 2.3. Simulated PL transitions: (a) Gaussian distributions of the phonons produced during possible PL transitions and (b) the corresponding PL spectra.

2.2 Phonon Replicas and the Huang-Rhys Factor

Phonon replicas are manifestations of longitudinal optical (LO) or transverse optical (TO) phonons produced during the PL process. The exact value of an LO or TO phonon is characteristic of the lattice parameters of a particular material. In CdTe, only LO phonons

are observed in PL, with an experimentally-determined energy of $E = \hbar\omega_{LO} = 21$ meV [37]. At extremely low temperatures, the only phonons observed in the PL spectrum are those created during the PL-induced transitions, and therefore the phonon replicas will appear only at lower energies than the zero phonon line (ZPL), or main transition. To put this another way, at low temperatures, the lattice contains insufficient phonons to allow the transition to "absorb" a phonon.

The shape of the ZPL and its LO phonon replicas, as well as their relative intensities, can be quantified by the Huang-Rhys factor, S, which measures the coupling between the defect and the crystal lattice (see Figure 2.4) [38]. The Huang-Rhys factor is usually indicative of the type of transition. A small value of S ($S \lesssim 1$) results in a very sharp ZPL and phonon replicas, and the ZPL has the highest intensity. Small S values are characteristic of excitonic and shallow defect transitions. Transitions with intermediate S values ($1 \lesssim S \lesssim 10$) still have distinguishable ZPLs and LO phonon replicas, but they are not as sharp and some of the phonon replica peaks may have greater intensity than the ZPL. These transitions generally involve defect complexes or intermediate-level defects. For large values of S ($S \gtrsim 10$), the ZPL and LO phonon replicas are not distinguishable, and the result is a broad, smooth peak. Identification of the location of the ZPL for these transitions is usually not possible. Deep defect states typically have large S values. Another plausible explanation for a broad, smooth peak is that there are several ZPLs very close together, and the resulting sum of Gaussian waves is indistinct.

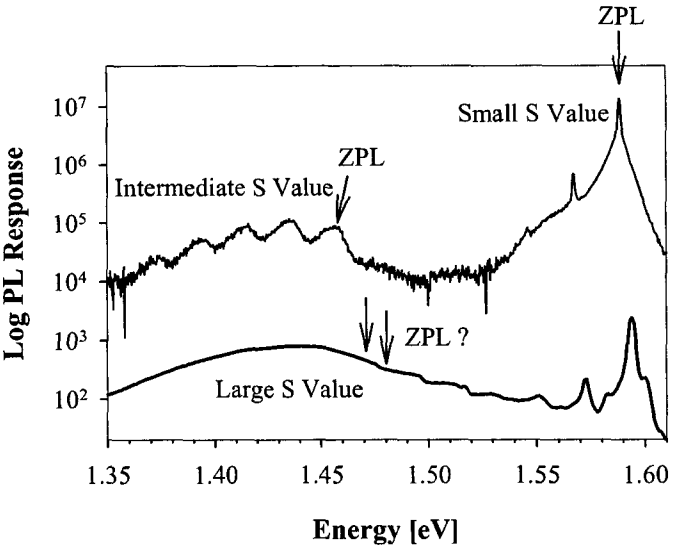

Figure 2.4. The value for the Huang-Rhys factor, S, determines the sharpness of the zero-phonon line (ZPL) and its phonon replicas. The two curves have been offset for clarity.

2.3 Intensity-Dependent Photoluminescence

As the intensity of the incident laser is changed, the intensity of the PL signal will respond, but not necessarily linearly. Theoretical modeling shows that the mathematical relationship between PL intensity and laser intensity is characteristic of the type of transition involved [39]. There is often a basic power-law dependence on the laser intensity:

$$I_{PL} \backsim I_{laser}^{p} \tag{2.7}$$

The value of p indicates the type of transition. If $1 < p < 2$ the transition is likely excitonic. However, if $p < 1$ the transition is likely related to a donor and/or acceptor. These values of p follow from the fact that transitions related to donors and/or acceptors are constrained by the density of the defect (saturation forces $p < 1$), whereas excitons

form almost independent of defect concentration (thus $p > 1$), although it is interesting to note that bound excitons will have some dependence on defect concentration and thus $p_{FE} > p_{BE}$. Although the power law dependence may help eliminate certain types of transitions, it is not a definitive indicator. Excitonic transitions include both free exciton and bound exciton transitions. Transitions related to donors and/or acceptors can involve a DAP, CB-A, D-VB, or countless donor or acceptor complexes. This power-law dependence holds over laser intensity ranges of roughly 2 orders of magnitude.

Although the power law dependence in Equation 2.7 does not make it possible to distinguish between a DAP and a CB-A or D-VB transition, there are other ways that the intensity-dependent PL can suggest the type of transition. A DAP peak will shift to higher energy with increasing laser intensity. As the laser intensity increases, the number of photons per area increases, and these photons will tend to excite donors and acceptors that are closer to each other in the crystal lattice. As this occurs, the distance r in Equation 2.5 ($E_{photon(DAP)} = E_g - E_D - E_A - \frac{q_A q_D}{4\pi\epsilon r}$) will decrease, causing the entire fourth term to increase. Since this fourth term actually adds to the transition energy ($q_D < 0$ and $q_A > 0$), the PL peak energy will increase with increasing intensity. This shift to higher energies with increasing laser intensity is often referred to as a "blue-shift." The CB-A and VB-D transitions do not have a coulomb interaction, so the PL peak should not shift to higher energy within a reasonable increase in laser intensity. Hence, the presence of an energetic shift in a peak with intensity can help support the assignment of a transition to a DAP rather than a CB-A/D-VB.

Relevant points of this discussion are shown schematically in Figure 2.5 (log scale), which is derived from the data in Figure 2.3. In this simulated PL, the p values are as follows: FE $p = 1.5$, BE $p = 1.2$, DAP $p = 0.7$, CB-A $p = 0.6$, D-VB $p = 0.65$. Note that, with increasing laser intensity, the intensity of the PL signal grows faster for excitonic transitions ($p > 1$) than for the donor and/or acceptor transitions ($p < 1$). Since the FE has a higher p value than the BE (recall that bound excitons require a defect, and will rely to some extent on defect concentration), there is some point where the relative intensities switch position. For the DAP transition, there is a shift to higher energies with excitation, while the CB-A and D-VB transitions do not exhibit this shift.

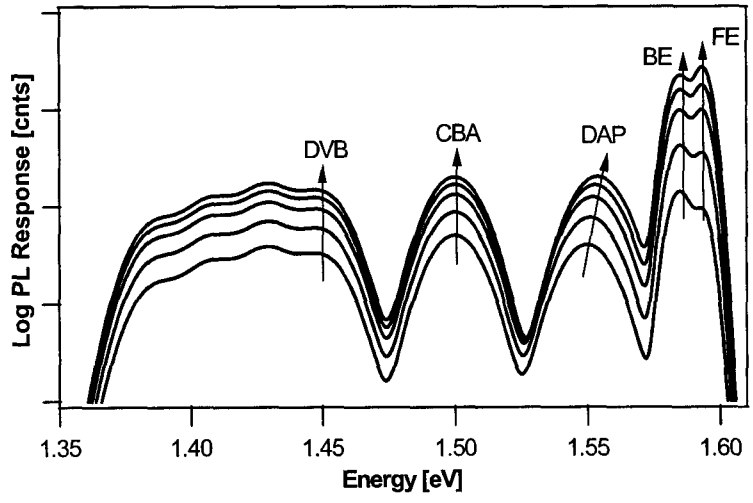

Figure 2.5. Simulated PL for laser intensities of 1, 2.5, 5, 7.5, and 10 W/cm^2. DAP PL energy shifts with excitation intensity.

In some instances, a red shift (shift to lower energies) may be observed in intensity-dependent PL. This can occur when a defect becomes completely saturated and some of these defects may trap two electrons or holes (doubly excited), which increases the

activation energy. One example of this is the V_{Cd} defect: for V_{Cd}^{-}, $E_a = 130$ meV and for V_{Cd}^{2-}, $E_a = 210$ meV [21].

2.4 Temperature-Dependent Photoluminescence

Temperature-dependent PL can give supportive information as to the type of PL transition. In general, a PL transition would be expected to shift to lower energies (red shift) as temperature increases because the band gap is decreasing. Hence a red shift would be expected for excitonic and band-to-defect transitions. The DAP PL transition is one exception to this trend. For the case of a DAP, at sufficiently high temperatures the shallower defect (donor or acceptor) is ionized, and the DAP transition suddenly becomes a band-to-defect transition, which has a higher PL transition energy than a DAP transition [40, 41]. This is often referred to as a blue-shift, but it occurs abruptly, unlike the gradual blue-shift seen with increasing laser intensity (see Figure 2.6, from Ref. [40]). Since hydrogenic donor levels are shallower than hydrogenic acceptor levels (Appendix A), it is generally believed that the donor level ionizes first, such that the DAP transition becomes a CB-A transition. For example, a blue shift with increasing temperature is generally ascribed as a donor-acceptor pair (DAP) transition.

Many have used temperature-dependent PL to determine activation energy levels. The intensity of a PL peak is related to the probability that a particular transition will occur. Probabilities that transitions will occur at certain temperatures can be found by adapting the equations for the Fermi-Dirac distributions. When only one trap is involved, i.e., CB-A

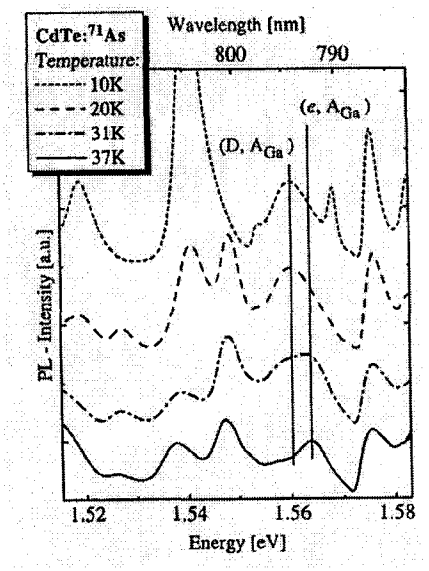

Figure 2.6. Example of a DAP that experiences a blue-shift when the donor levels are thermally ionized at higher temperatures.

or VB-D, this is fairly straightforward.

$$\frac{I(T)}{I_o} = \frac{1}{1 + Ce^{-\frac{E}{K_B T}}} \tag{2.8}$$

I and I_o are the values of the integrated intensity under the ZPL (I_o is the reference value). The coefficient C and the activation energy E are used as fitting parameters. The best fit will yield the value of E. When two traps are involved, such as for a DAP, equation 2.8 is modified to contain two activation energies [42,43]

$$\frac{I(T)}{I_o} = \frac{1}{1 + C_1 e^{-\frac{E_1}{k_B T}} + C_2 e^{-\frac{E_2}{k_B T}}} \tag{2.9}$$

The energies E_1 and E_2 must be constrained by the Equation 2.5 ($E_1 + E_2 = E_g - E_{photon} + \frac{q^2}{4\pi\epsilon r}$). Although the coulomb interaction term may not be known exactly, it is usually on the order of a few meV. The smaller of the two energies is generally ascribed to a donor level. This follows from the hydrogenic defect model, where the activation energy

is directly related to the effective mass, and the hole effective mass is generally larger than the electron effective mass.

Recent studies, however, have shown that Equations 2.8 & 2.9 are not accurate for CdTe at low temperatures (T < 80 K) [44]. In Figure 2.7, taken from Ref. [44], the slope of the arrhenius plot of three different PL transitions (bands) with temperature is almost the same, although the activation energies must be very different. Since the slopes in Equations 2.8 & 2.9 are governed by the activation energies used, it is obvious that these simple equations do not work for fitting the data in this low-temperature regime. Instead, all have a slope close to 3/2. A simple change in Equation 2.8 would give:

$$I(T) = \frac{I_o}{1 + C_1 T^{3/2} + C_2 T^{3/2} \exp(-E/kT)} \tag{2.10}$$

Note that the $T^{3/2}$ in this equation not only improves the experimental fit to the data, but it would also correspond to reasonable approximations of real quantities. The temperature dependence is governed by the probability of electron or hole capture on an empty site. This probability is the product of thermal velocity, v (~$T^{1/2}$), and capture cross section, σ. At low temperatures it is reasonable to approximate that the capture cross section for electrons and holes will vary as T^{-2} [45–47].

When dealing with "deep" levels, where $\exp(-E/kT) \ll 1$ or E $\gtrsim$ 50 meV, Equation 2.10 is dominated by the capture cross sections ($T^{3/2}$ term), and the fit should result in a line with $T^{3/2}$ dependence. This explains why only shallow defects can be fit accurately with temperature-dependent PL techniques. Therefore, the temperature-dependent PL data for transitions with defects > 50 meV will not be fit, but will be examined for general trends.

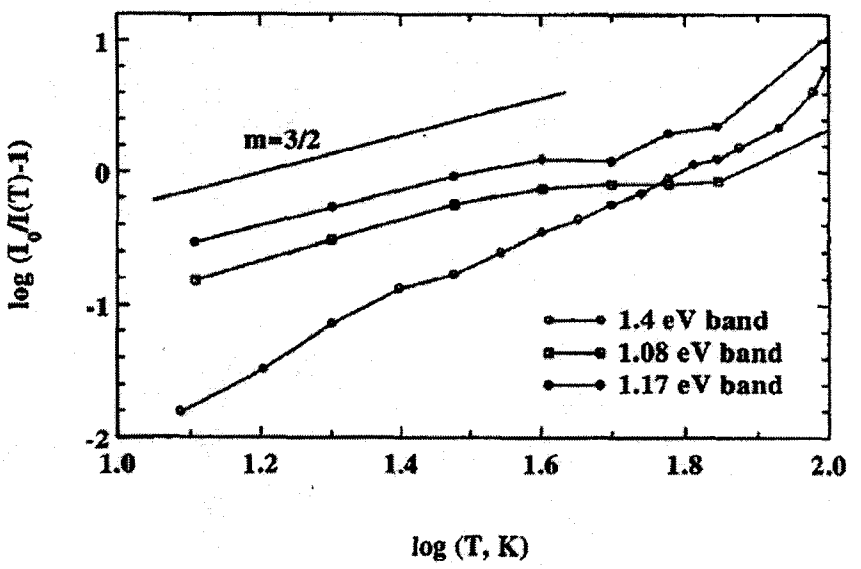

Figure 2.7. Measured temperature dependence of the PL intensity for peaks at 1.08 eV, 1.17 eV, and 1.4 eV in CdTe, plotted as $\log[I_o/I(T) - 1]$ vs. log(T). The lines through the experimental points are drawn as visual aids only. The straight line with slope m = 3/2 is included for comparison.

2.5 Luminescence Studies on CdTe

The first photoluminescence study on CdTe was published in 1959 by D. de Nobel [48, 49]. These measurements utilized a Hg lamp as a light source, which was passed through a $CuSO_4$ solution to select infrared radiation for the excitation beam. The PL spectrum was taken using a quartz monochromator in conjunction with a photomultiplier tube. All measurements in that study were performed at 77 K.

In the nearly 50 years since the first PL studies, technology has advanced so that these experiments are much easier and less time-consuming to perform. The wide-spread availability of lasers makes it possible to use excitation light of a well-known wavelength. Electronics such as charge collection devices (CCDs) in conjunction with computer interfacing have made the collection of the PL spectrum very simple and fast. In addition, improve-

ments to the closed-cycle gaseous helium expander/compressor have made low temperature measurements much more convenient. Although the technology surrounding PL has changed, the basic approach used by de Nobel is still being used today.

2.5.1 Single-Crystal CdTe Studies

Since Cu and Cl are routinely incorporated into single-crystal IR detectors as well as thin-film CdTe solar cells, there have been many photoluminescence and cathodoluminescence (CL) studies on Cu and Cl defects in single-crystal CdTe (CL will be discussed in Chapter 3). However, few of these studies that examined the intermediate-level ($1.3 - 1.55$ eV) and deep-level (< 1.3 eV) PL regions are conclusive. Instead, many of the more thorough studies focus on the excitonic levels and shallow defects [42, 50]. These tend to be easier to interpret, as these transitions are sharp and well defined, whereas the lower-energy peaks tend to be broader and involve many phonon replicas, which makes it difficult to identify the primary transitions. Additionally, reported CL studies on Cl-related deep acceptor states [35, 51, 52] were performed at 77-80 K. This temperature range was used for these studies because historically it was convenient to take PL and CL at liquid nitrogen temperatures. PL on CdTe has been routinely measured at liquid helium temperatures for only the last 10-15 years, and CL has only recently been performed at these low temperatures. As will be shown later, PL measurements at liquid helium temperatures are crucial to observing certain PL transitions.

There is much confusion in the literature over the defect assignment of intermediate-level defects in crystalline CdTe. One example is the assignment for a peak near 1.45 eV

in the low-temperature (2-10K) PL spectrum. This peak is typically seen as a broad defect band centered at 1.45 eV, with phonon lines indistinguishable from the ZPL. This peak centered at ~1.45 eV has been seen in Cu-containing samples, indicating that this peak may be caused by a Cu-related acceptor state [42, 53]. Some publications suggest that the 1.45-eV peak originates from recombination at oxygen-related acceptors [54, 55]. Others claim that there is more than one emission that contributes to the PL signal in the 1.3 to 1.5 eV region [56, 57]. This peak has also been attributed to the acceptor complex Cl_{Te}-V_{Cd}, often referred to as the Cl A-center. Yet another study claims that a peak at 1.454 eV is a donor-acceptor pair (DAP) involving both Cu and Cl [58]. Resolution of these conflicting interpretations has been a motivating factor for the current work.

The relatively unknown link between PL peaks and defect-related transitions in CdTe is in stark contrast to other materials, such as GaAs, where the single-crystal PL has been so well characterized that there are reference books published with the known peaks and their related transitions. The difference is in part due to the difficulty in growing very pure CdTe. Since there are a large number of impurities in CdTe, it is difficult to distinguish between changes in PL that arise from something done intentionally and those arising from an unintentional activation of impurities present in the as-grown crystal. Another problem is that CdTe is a material that forms compensating defects during doping. This means that, as CdTe is doped with a species designed to make it p-type, unintentional defects spontaneously form, which can be n-type or, more typically, mid-gap and act as recombination sites rather than as current carriers [21, 59]. These complications are likely one reason why very few systematic studies are available in the literature. In some studies, more than

one variable has been introduced. One example of this is the study by Grecu *et al.*, in which the Cu diffusion was performed in an oxygen-containing atmosphere, but the study did not separate the role of oxygen during defect assignment. And yet another problem is that many people appear to believe that PL from CdTe is well understood and thus believe that there is little more work to be done on single-crystal CdTe. However, a review of the literature shows that many of the peak assignments are tentative at best if they are given at all. In most cases, the authors have made no attempt to identify the locations of the ZPLs of broad-band peaks, let alone make a defect assignment. A systematic study is needed to separate the possible sources of the intermediate-level defects — Cu, Cl, O, or some combination — so that a distinct assignment can be made.

2.5.2 Photoluminescence on CdS/CdTe Solar Cell Materials

Relatively few PL and CL studies have been performed on thin-film CdTe, and virtually all have been done in the context of CdS/CdTe solar cells. Most studies focus on the effects of the $CdCl_2$ treatment on the PL spectra. These studies observe a peak at 1.45-1.46 eV, which has been attributed to the V_{Cd}-Cl_{Te} complex [60–62]. These studies range from looking at the PL after the thin-film CdTe is exposed to Cu, Cl, and O (or some combination) to studies looking at the effect of annealing atmosphere during a $CdCl_2$ treatment. However, none of these studies included untreated samples (i.e., as-grown thin-film CdTe that should contain little Cl).

Figure 2.8 shows the PL signal on as-grown (untreated) pX thin-film CdTe as compared to nominally undoped sX CdTe. One glaring difference between the PL signals is

the presence of a peak at 1.456 eV in the thin-film CdTe that is not readily apparent in the undoped sX CdTe. This peak is almost identical to the PL signal seen by Valdna [60], but it was not necessary to use the $CdCl_2$ treatment to form this PL peak. It is likely that the origin of this transition is a defect formed during the thin-film growth process, which typically includes intentional oxygen as well as unintentional Cu impurities, as was discussed in Chapter 1. This peak at 1.456 eV will be the primary focus of investigation for this thesis.

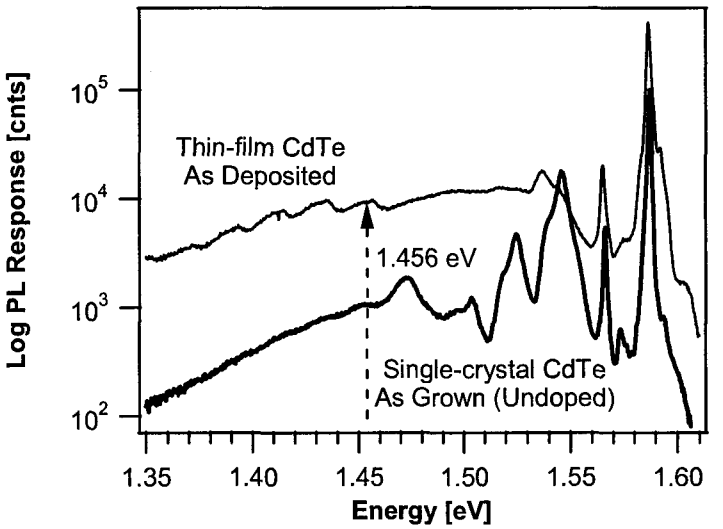

Figure 2.8. PL on nominally undoped single-crystal CdTe (thick line) and on as-grown thin-film CdTe (thin line).

To understand the complicated phenomena occurring during device processing, one should look at the possible species present during the thin-film processes and then attempt to recreate these PL signatures in carefully controlled single-crystal CdTe samples. When this is done in a systematic way, it is possible to make reasonable defect assignments.

2.6 PL Experimental Setup

PL measurements were performed at 4.5 K in a closed-cycle He cryostat. A schematic of the experimental setup is shown in Figure 2.9. The 632.8 nm line of a HeNe laser were used for excitation (beam size: d = 500 μm, A = 0.2 mm^2). The intensity of the laser line was varied from 0.5 – 10 W/cm^2 using a neutral density (ND) filter wheel. A 695-nm long-pass filter was used to avoid second order lines from the laser. PL data were collected with a spectrograph (500-μm slit and 600-grooves/mm diffraction grating) and a CCD with 512 pixel resolution. ND filters were used to avoid saturating the spectrograph, and the data were later corrected for the ND filters as well as for the response of the spectrograph. Spatial-variation PL was done on several samples to examine how PL varies across the surface of the sample. Additionally, intensity-dependent PL was performed at 4.5 K and

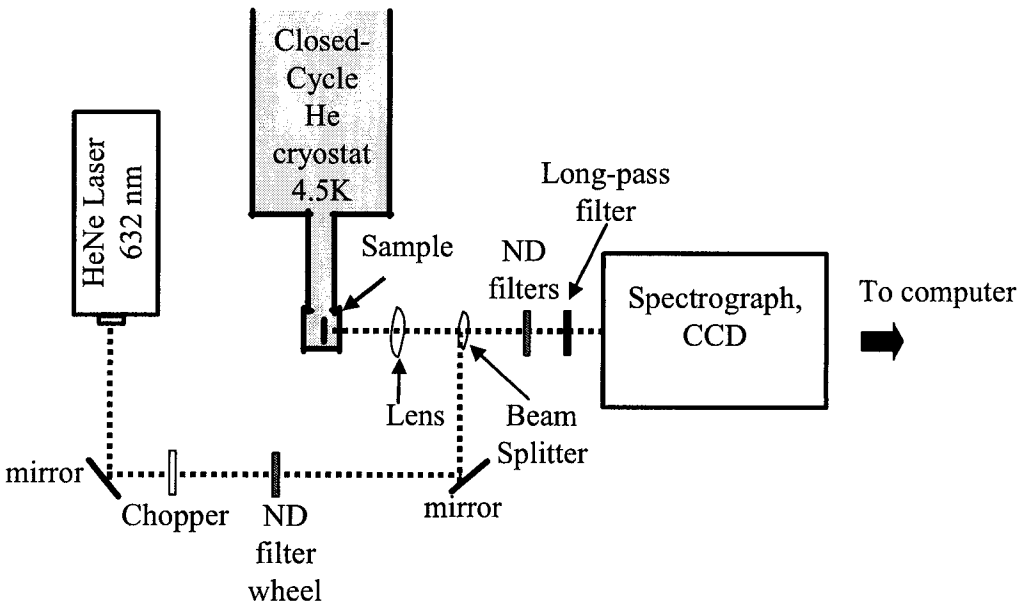

Figure 2.9. Schematic drawing of PL setup.

temperature-dependent (10 – 100 K) PL data were taken with a laser intensity of 0.5 W/cm^2.

All PL data were fit using multiple-peak-fitting algorithms available in Igor Pro. When PL peaks are sharp, the fit results can be as accurate as ± 1 meV. Transitions red-shifted by integer values of 21 meV from the next highest transition are generally ascribed as phonon replicas, and the transition with highest energy in these series is assigned as the zero phonon line (ZPL), as can be evidenced in Figure 2.4 from Section 2.2. All cited energetic peak locations are given based on results from the best fit to PL data.

2.6.1 PL Counts: Using Absolute Versus Arbitrary Units

Most papers publishing PL data display the PL counts as arbitrary units rather than as absolute numbers. Others even use one of several normalization methods, one of which is to set the free exciton peak intensity to 1000. The problem with using arbitrary units and/or normalization methods is that some PL changes relating to different sample preparation may be obscured. The main argument in favor of using arbitrary units is that PL variation over the sample is so large that it is almost impossible to state the correct PL signal with any accuracy. This idea was tested by taking PL at various spots on the CdTe sample (spatial-variation PL).

Spatial variation PL data was taken on single-crystal CdTe that was either as-received or had received a BrMe etch (Figure 2.10). The data show that the response of a particular peak may vary by a factor of 2-3 across a sample. The intensities of the excitonic and near-band edge transitions tend to vary more across the sample than those from the lower-energy transitions. The reason for this difference is unclear, although it may be that excitons and

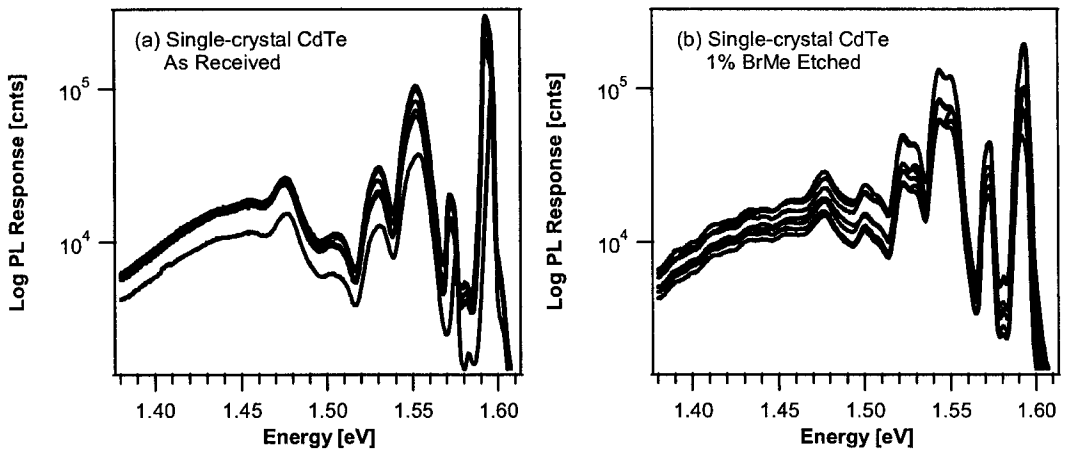

Figure 2.10. Variation of PL over the surface of one single-crystal CdTe sample: (a) as received and (b) with a 1% bromine methanol etch.

shallow defects are more surface-dependent than the intermediate and deep levels. These results cast doubt on the method of normalizing the PL signal to the exciton peak, since it varies more over the sample. It is apparent that for all types of transitions the difference of a peak's intensity across a surface is less a factor of 5. Since this is true for PL signals the order of 10^4 - 10^5, this is a relatively low noise-to-signal ratio. As long as this variation over one sample is taken into consideration, then absolute units can be used for PL counts. For all PL data shown in subsequent chapters, shifts in peak intensity from separate samples that differ by less than half an order of magnitude are considered not of appreciable significance, and results that differ by one order of magnitude or more are considered to be due to differences resulting from the experimentally controlled parameters.

Chapter 3

Supplementary Experimental Techniques and Theoretical Calculations

3.1 Cathodoluminescence (CL)

Cathodoluminescence is a technique that is similar in many ways to photoluminescence. It utilizes a scanning electron microscope (SEM) that sends a beam of high-energy electrons into the sample. Because each high-energy electron can produce many electron-hole pairs, the CL signal is much more intense than a PL signal. The electron-hole pairs recombine via similar pathways as those discussed in Section 2.6. The unique capabilities of CL include its ability to spatially map the radiative recombination over the sample (mapping CL) and to probe different depths in the sample (depth-profiling CL).

Depth profiling can be performed by varying the energy of the electron beam when it is incident on the top of the sample (plan-view) or by performing a scan along a cleaved edge of a sample (edge-view), as shown pictorially in Figure 3.1. Increasing the energy of the electron beam enlarges the size of the probing region, represented as an oval in Figure 3.1, while scanning along a cleaved edge is generally performed at a constant e-beam energy and thus a constant probing region size.

Plan-view CL (varying the energy of the electron beam) is the most commonly-used configuration of CL measurement, and there are several advantages to this method.

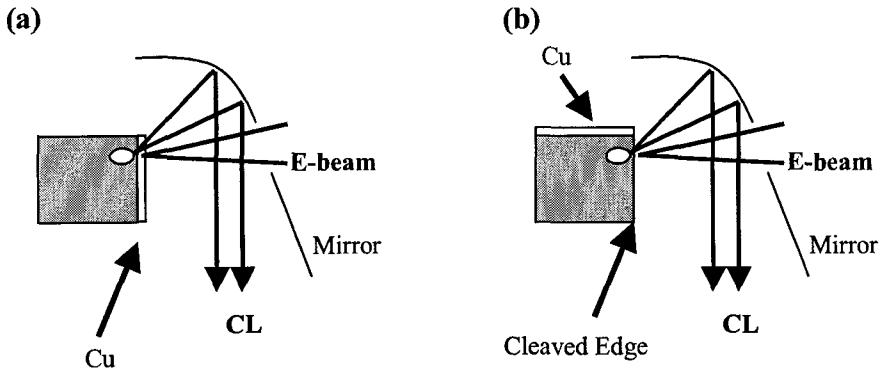

Figure 3.1. Schematic drawing of depth-profiling cathodoluminescence: (a) plan view and (b) edge view CL.

First, plan-view CL is not inherently destructive, although it would require a free film surface. Second, this is the orientation used for mapping, so it would be possible (although tedious) to measure the depth profile over the entire surface of the sample and examine variations with, for example, grain boundaries. Unfortunately, there are some challenges in interpreting data taken in the plan-view configuration. As the energy of the electron beam increases, the relative size of the CL probe region increases. This larger sampling region would include some near-surface transitions as well as those deeper in the sample, and it would be difficult to separate these in the CL spectrum. An additional challenge comes when interpreting intensity-dependent CL data. With higher energies (intensity of the signal), the CL will change based on two factors: (1) the CL signal should increase due to the higher intensity of the signal, similar to intensity-dependent PL; and (2) the CL will not be probing the same regions as at lower energies because of a larger sampling region.

Edge-view CL has the advantage that CL can be taken at different depths without changing the energy of the electron beam. However, there is the drawback that the sample must be cleaved in vacuum to reveal a clean edge (destructive to solar cell devices). An additional problem was revealed in the single-crystal CdTe studies related to this work. Figure 3.2 shows spatially-resolved CL over a mechanical defect caused by cleaving. The CL response is displayed at energies corresponding to peak locations in the line-scan CL, which looks similar to a PL spectrum. The response of these peaks varies widely, and is dependent on whether or not there is a mechanical defect present. Note that at some wavelengths, there is a PL response within the mechanical defect. This difference is not apparent in all semiconductors. In GaAs, for example, there is no CL signal from a mechanical defect, regardless of wavelength. Although this variation in CL response is interesting and has some other possibly useful applications (such as distinguishing phonon replicas), the implication is that depth-profiling scans via edge-view CL are not a wise way to track diffusion parameters in single-crystal CdTe since there are likely to be many mechanical defects along a cleaved edge. Thus, the method of taking CL from the top of the sample (Figure 3.1a) and increasing the electron-beam energy is the better method of probing deeper into single-crystal CdTe.

3.2 Surface Analyses

Since photoluminescence is sensitive to the first 0.5 μm and strongly affected by surface conditions, surface analysis techniques were performed collaboratively (see acknowl-

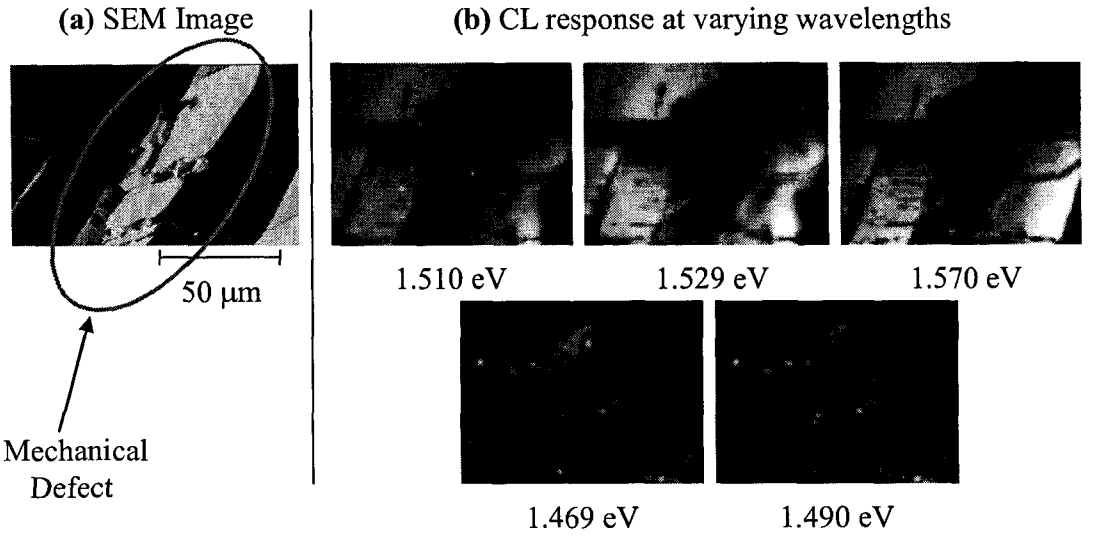

Figure 3.2. Spatially-resolved CL for single-crystal CdTe. (a) SEM image of cleaved CdTe with mechanical defect. (b) CL response of specific wavelengths over the same area displayed in the SEM image.

edgements) as complimentary techniques to help understand changes in the surface chemistry and morphology and how this might relate to the changes in the PL signal. Techniques used in this study include: x-ray photoelectron spectroscopy (XPS), ultraviolet photoelectron spectroscopy (UPS), Auger electron spectroscopy (AES), scanning electron microscopy (SEM) and atomic force microscopy (AFM). All techniques except AFM were performed under ultrahigh vacuum (UHV) of 10^{-8} Torr. The surface studies looked not only at the samples prepared exclusively for PL, but also were used to study the thermodynamics of Cu diffusion in UHV.

3.2.1 X-ray and Photoelectron Spectroscopy (XPS)

The techniques of XPS and UPS are very useful in understanding the surface of samples. A diagram of how XPS works is shown in Figure 3.3. An x-ray, generally of energy

1-2 keV, is incident upon the sample surface. The x-ray has such a high energy that one photon can eject an electron from a core level in the sample. The kinetic energy of this electron is measured with the spectrometer. The binding energy is then determined from the kinetic energy of the ejected electron:

$$E_b = h\nu_{Xray} - KE_{electron} \tag{3.9}$$

where ν is the frequency of the x-ray. This value for the binding energy will vary slightly with a change in chemical surroundings.

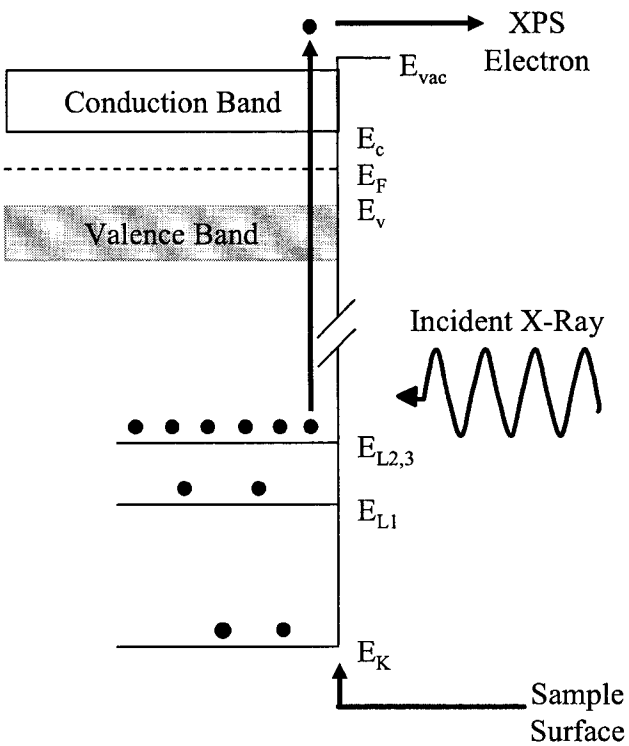

Figure 3.3. Energy diagram showing how XPS interacts with the core levels in materials

Although XPS is often considered a non-destructive measurement technique, it is often used in conjunction with ion beam milling. XPS is good for probing the chemistry of a sample very near the surface, but to probe deeper into the sample the surface can be sputtered away and XPS can be taken again at this new surface. This is referred to as sputtering depth-profile XPS. This is useful in determining the thickness of a surface layer on a sample. Another way to measure the thickness of a layer is via angle-resolved XPS, shown in Figure 3.4. The intensity of the photoemission is governed by the Beer-Lambert Law:

$$I_d = I_o \exp\left(-\frac{d}{\lambda \sin\theta}\right) \tag{3.10}$$

where θ is the photoemission or take-off angle and λ is the mean free path, which is usually on the order of 10Å. Equation 3.10 can be rearranged to find how the angle θ relates to the depth XPS is probing into the sample.

$$d = -\lambda \sin\theta \ln\left(\frac{I_d}{I_o}\right) \tag{3.11}$$

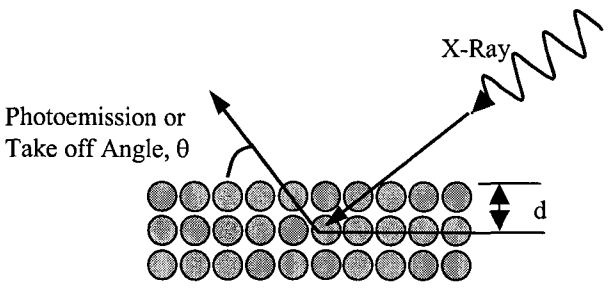

Figure 3.4. Angle-resolved XPS.

3.3 First Principles Band Structure Calculations

In a collaboration with NREL scientists, theoretically-derived defect energy levels were obtained from first-principles-band-structure calculations. First-principles-band-structure calculations, unlike the hydrogenic defect model that gives only an idea of the range of the activation energies for shallow donors and acceptors, can calculate the activation energy for a specific defect. The accuracy of the calculations depends on how well the material properties are known. Previous comparisons between theoretically-calculated and experimentally-determined activation energies have ranged from 0.04 - 0.1 eV apart [21,63].

First-principles-band-structure calculations were used to give an approximate solution to the non-relativistic Schrödinger equation of the defect within the lattice environment. To go from the non-relativistic Shrödinger equation to a value for the activation energy of a defect is a non-trivial process, and is explained in detail in Refs. [21,64]. An overview of this process is as follows: (1) Use the Born-Oppenheimer approximation (the motion of electrons are independent of the motion of the nuclei) to separate the Schrödinger equation such that there is one wave function for the nuclei and one for the electrons; (2) since only electronic properties are being examined, only the equation describing electron motion is considered; (3) the Local Density Approximation (LDA) is applied, which uses a homogeneous electron gas to describe the electron exchange correlation (this is accurate for slowly-varying electron densities); and (4) the supercell approach, which configures an array of multiple unit cells of CdTe with periodic boundary conditions, is used to solve numerically (using VASP code [65]) for the desired quantities. The calculations are typically

performed at 0 K, but the activation energies of defects tend to track the respective band, e.g., the activation energy of an acceptor measured from the valence band approximately stays the same as the temperature increases.

3.4 AMPS-1D Simulations

AMPS-1D was used in collaboration with colleagues at CSU to determine the possible effects on solar cell performance (J-V curves) caused by defects observed with PL in the CdTe layer. AMPS-1D is a simulation software package that was developed at Pennsylvania State University by Stephen J. Fonash and is distributed free of charge. AMPS stands for "Analysis of Microelectronic and Photonic Structures." AMPS-1D solves the following coupled differential equations in one dimension to obtain band diagrams and, subsequently, J-V curves: Poisson and electron and hole continuity equations; carrier transport equations; optical generation equation; and recombination equations for n-type or p-type semiconductors. The details can be found in Ref. [66].

Many parameters must be entered into AMPS-1D, such as device properties, layer properties, and defect states. A baseline case for AMPS-1D has been established using exact values, when known, and reasonably assumptions for parameters [67]. The baseline case uses a carrier concentration of 2×10^{14} cm^{-3} in the CdTe layer, and includes a mid-gap defect (E_C - 0.75 eV) with concentration 2×10^{14} cm^{-3}.

Chapter 4

Single-crystal CdTe Material Studies

The main goal of the single-crystal (sX) CdTe studies is to systematically introduce different impurities in an effort to reproduce the PL at 1.456 eV seen in thin-film polycrystalline CdTe. Since this peak at 1.456 eV was seen in as-deposited CdTe, we identified two possible species, Cu and O, from known incorporants and impurities present in the growth process. Cu is one of the most common impurities present in the CdTe source [68, 69], and O is intentionally incorporated into the growth chamber. Since others have suggested a Cl-related origin for peaks in this area, some sX CdTe samples were treated with $CdCl_2$. Finally, theoretical calculations to determine a possible defect assignment are described.

4.1 Sample Preparation

Undoped single-crystal (sX) CdTe samples (for crystal lattice, see Figure 4.1) were manufactured by Keystone Crystals with 6/9 (99.9999%) purity starting materials using the vertical Bridgman technique [37]. The specification of 6/9 purity is based on manufacturer testing for concentrations of Cu, Fe, Mg, Mn, Zn, Ga, and Ge. The CdTe crystals were cut and received a mechanical polish on the B-side only (Te-rich) by the manufacturer. The mechanical polish was done using progressively smaller AlO_2 grits, down to 0.1 μm. Hall measurements were taken at NREL using the van der Pauw technique [70], with contacts made using an industrial process consisting of a liquid Cu-

containing solution applied to each of the four corners, followed by applying indium solder after the solution had dried. These measurements determined the sX CdTe was p-type, with carrier concentration $3 - 5 \times 10^{14}$ cm^{-3} and hole mobility $30 - 60$ $cm^2/V\text{-}s$.

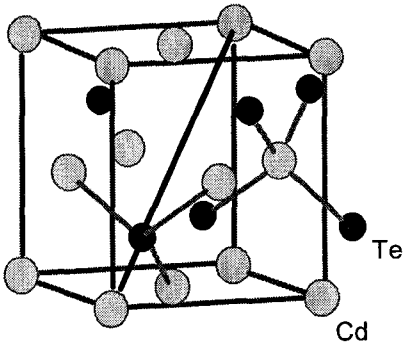

Figure 4.1. CdTe crystal lattice (zincblende structure).

Initial studies focused on the effect of surface preparation on the subsequent treatments, including Cu diffusion and a $CdCl_2$ treatment. Many publications refer to the use of bromine methanol (BrMe) in various concentrations either prior to or after anneals, but the literature is not conclusive on the physical processes involved. The effect of BrMe alone and with subsequent treatments was examined with PL, AFM, and XPS. The results of these studies led to the decision *not* to use a BrMe etch in the Cu diffusion studies. Studies on BrMe etching of CdTe without other treatments are discussed in Appendix B. The effects of etching on the PL for $CdCl_2$-treated and Cu-diffused CdTe samples are discussed within this chapter.

Cu diffusion was studied under various annealing ambients at atmospheric pressure that ranged from reduction to oxidation. Samples with and without 10-nm electron-beam-deposited Cu were annealed at 400°C for 1 h in either 10% H_2 + 90 % N_2 (forming gas),

pure N_2 gas, 20% O_2 + 80% N_2 (air-like), or pure O_2. In each case, the quartz tube was purged with the selected gas and the total gas flow rate was ~3 ℓ/min. It is important to note that because the annealing tube was not evacuated prior to the purge/anneal sequence, it was difficult to obtain a completely oxygen-free N_2 anneal in this configuration. The experimental matrix can be found in Table 4.1. There were samples with Cu or O, and a set with both species. For each type of sample, this entire procedure was repeated multiple times to verify the reproducibility of the results.

Cu	Anneal Atmosphere
None	10% H_2 / 90% N_2
None	N_2
None	O_2
10 nm	10% H_2 / 90% N_2
10 nm	N_2
10 nm	20% O_2 / 80% N_2
10 nm	O_2

Table 4.1. Matrix of single-crystal CdTe samples.

4.2 $CdCl_2$ Treatment of Single-crystal CdTe

PL data for $CdCl_2$-treated single-crystal CdTe are shown in Figure 4.2. The $CdCl_2$ treatment affects the PL signal differently in the high- and low-energy regions. In the high-energy region, the PL intensity increases by 2-3 orders of magnitude and the peaks shift to lower energies after the $CdCl_2$ treatment. For these peaks, etching prior to $CdCl_2$ has no effect. This increase in intensity is reminiscent of the effects caused by BrMe etching alone (see Appendix B), but the $CdCl_2$ further enhances the near-band gap PL signal. This

could also be due to a change in band bending or a reduction in the amount of Cd near the surface.

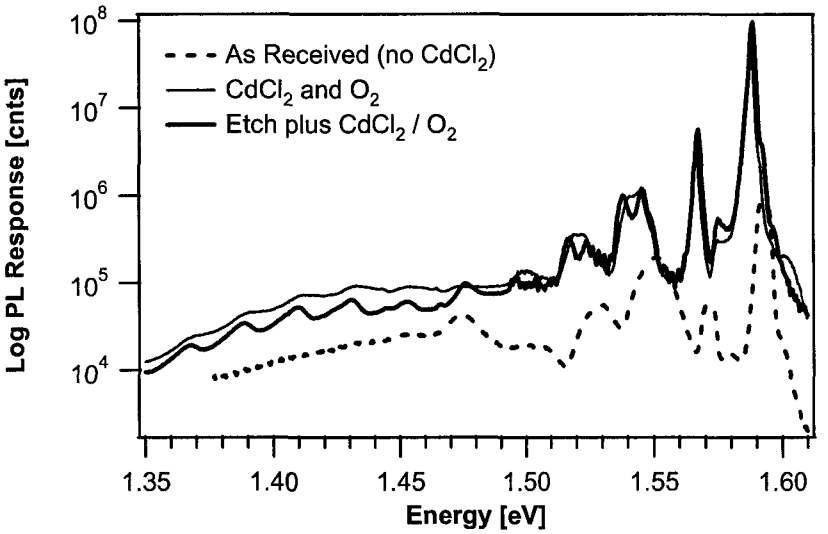

Figure 4.2. Effect of $CdCl_2$ treatment on CdTe single crystals with and without a preceding BrMe etch.

In the 1.3 - 1.5 eV region of the PL in Figure 4.2, small peaks form after $CdCl_2$ at ~1.45 eV and below, and this PL region has an intensity increase of less than one order of magnitude. For etched samples, this peak and its phonon replicas are shifted to slightly lower energies. This new PL transition may result from the Cl in the $CdCl_2$ treatment, but Cl is not the only impurity introduced since $CdCl_2$ treatments typically include O_2 in the ambient and Cu can be present as a $CdCl_2$ source impurity.

There is a question whether sufficient Cl diffusion from the $CdCl_2$ treatment enters the PL-probed region of the CdTe. The diffusion constant of Cl in single-crystal CdTe at 400°C (D_{Cl} = 7.5 x 10^{-14} cm^2/s) [71] suggests a long diffusion time. It would therefore take the order of a month for Cl to diffuse through a 10 μm sample of single-crystal

CdTe at standard $CdCl_2$ treatment temperatures [72]. Since the $CdCl_2$ treatment time in our study was only 8 min, Cl should not have diffused very far into the bulk CdTe and would not be expected to alter the PL signal. The possible effects of Cl will be addressed further in Chapter 5 where one would expect faster diffusion (along grain boundaries) with polycrystalline material.

4.3 Cu Diffusion in Single-crystal CdTe

4.3.1 Effects of Etching on Cu-Diffused Samples

PL was taken on single crystal samples with different surface preparation prior to the Cu diffusion step. For the samples represented in Figure 4.3, the anneal is in N_2 at 200°C for 1 hr. The sample that received an etch prior to Cu diffusion shows a reduced PL response compared to the sample that did not receive an etch. Additionally, the discernible peaks are not the same for the two samples. In the literature, it is assumed that the broad peak centered near 1.45 eV is Cu-related, possibly Cu_{Cd} [42]. If this peak is Cu-related, then one could assert that the BrMe etch inhibits Cu diffusion into CdTe. This has been observed with other techniques, which show that the Te-rich layer formed during a BrMe etch getters Cu, possibly forming a CuTe layer [73]. Regardless of whether the PL peak centered near 1.45 eV is related to Cu or not, it is obvious that the BrMe etch does affect the formation of defects in this PL region, and the resulting PL signal looks much altered. Hence, subsequent studies involving Cu diffusion did not use a BrMe etch prior to Cu diffusion.

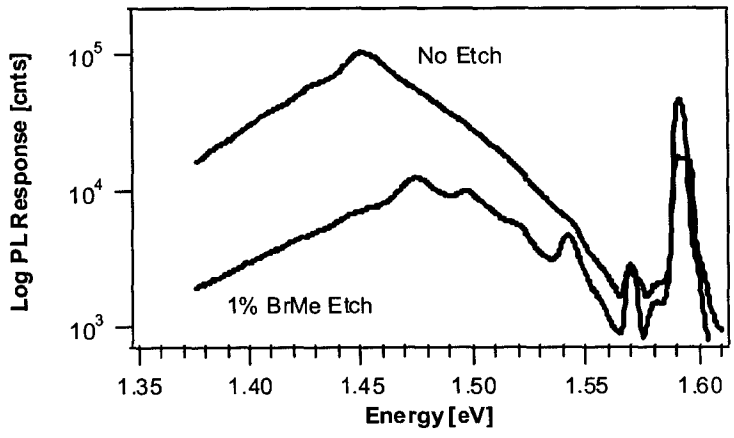

Figure 4.3. PL on samples with or without a BrMe etch prior to Cu evaporation and anneal at 200°C.

4.3.2 Diffusing Cu under Different Ambients

Figure 4.4a shows photoluminescence on CdTe samples without Cu, annealed in atmospheres ranging from reducing (forming gas) to oxidizing. A non-annealed sample is also shown for comparison. None of these non-Cu samples showed structure in the region of interest below 1.46 eV. There was, however, a set of peaks between 1.535 and 1.550 eV with two phonon replicas. The excitonic transitions in the N_2- and O_2-annealed samples were very similar to those for the non-annealed sample. There was a dominant peak at 1.587 eV and a "shoulder" at 1.591 eV. When CdTe was annealed in forming gas, however, the 1.587 eV peak disappeared, and the 1.591 eV peak became dominant. Because an anneal in forming gas should make the surface more stoichiometric, the 1.587 eV excitonic peak is likely related to an off-stoichiometry defect. The non-annealed and N_2-annealed samples also exhibited a peak at 1.475 eV, which was previously identified as a Y-dislocation [74].

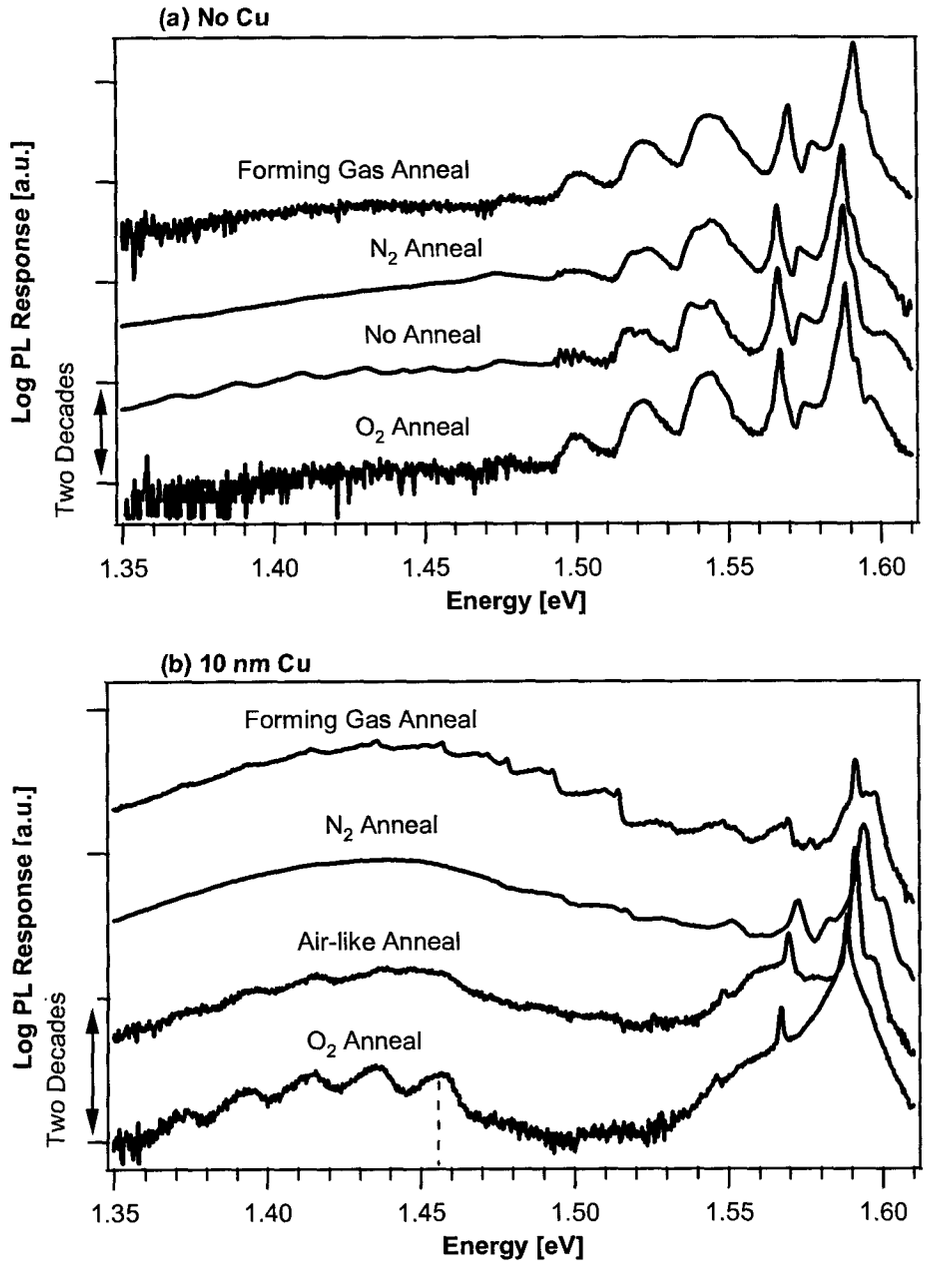

Figure 4.4. Single-crystal CdTe samples annealed in different ambients. Curves offset for clarity. (a) CdTe without Cu annealed in forming gas, nitrogen gas, or oxygen gas; a non-annealed sample is also shown. (b) CdTe with 10 nm Cu annealed in forming gas, nitrogen gas, air-like gas, or oxygen gas.

The PL spectra changed dramatically when Cu was deposited prior to annealing, with the biggest difference in the PL band from 1.35 – 1.53 eV (Figure 4.4b); these anneals also eliminated the 1.535 - 1.55 eV peaks seen prior to annealing. The nitrogen-annealed sample had a broad, smooth peak in this region, whereas the other samples had distinct zero phonon lines (ZPLs) and phonon replicas. This suggests a large Huang-Rhys factor for the N_2-annealed sample, possibly suggesting a deep defect state. The O_2-annealed and forming gas-annealed samples are more indicative of intermediate Huang-Rhys factors, which suggests an intermediate defect level or a defect complex.

Only the Cu samples annealed in an oxygen or air-like ambient had the PL feature of interest with ZPL at 1.456 eV (Figure 4.4b: Note that the forming gas anneal has a phonon replica in this region, but the ZPL is at ~1.51 eV). This PL transition is not seen in any of the sX samples that did not include Cu (Figure 4.4a) or in the Cu samples annealed in forming gas (reducing atmosphere) or in oxygen-free nitrogen. This peak was only seen when both copper and oxygen were incorporated in the CdTe. It is important to note that no Cl was introduced into these samples, hence Cl is not necessary to form the PL peak at 1.456 eV. Thus, this peak is likely associated with a defect complex involving Cu and O. Relating this PL peak to a defect complex is certainly consistent with its intermediate Huang-Rhys factor.

Further annealing experiments were performed to determine the importance of annealing ambient on the formation of the 1.456-eV PL peak in Cu-coated CdTe samples (Figure 4.5). The sample that had first received an O_2 anneal was later annealed in forming gas for one hour Figure 4.5b. The results indicate that the PL signal was almost identical

to the case where the Cu was deposited, followed by a forming gas anneal (Figure 4.5a). Forming gas is a reducing atmosphere, i.e., it removes oxygen from the crystal. Since the 1.456-eV PL peak disappears with the removal of oxygen, this is additional evidence that O_2 is required to form this PL peak. In contrast, the sample that was originally annealed in forming gas was later exposed to air, and the resulting PL signal looks very similar to the initial case of 10 nm Cu and an O_2 anneal. Although no anneal was performed in this case, it is likely that the forming gas anneal creates dangling bonds that rapidly capture oxygen when the sample is exposed to air, and the oxygen may penetrate below the surface of the sample. Thus, it is feasible that the oxygen could be available for defect formation.

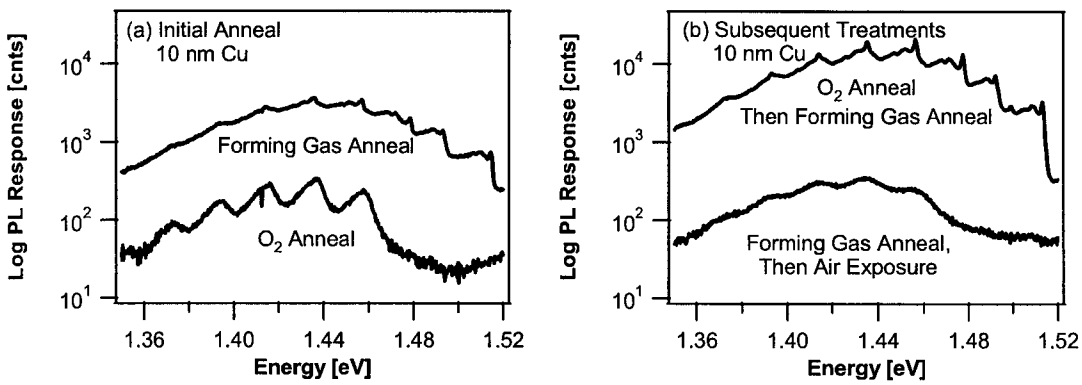

Figure 4.5. PL in the 1.35 - 1.52 eV region for samples with 10 nm Cu. (a) Initial anneals in O_2 only or forming gas only; (b) the O_2-annealed sample receives a subsequent forming gas anneal, and the forming-gas annealed sample is exposed to air.

Intensity-dependent and temperature-dependent PL were performed on the O_2-annealed Cu sample (Figure 4.6) to determine the type of transition for the 1.456 eV. The energy of the peak at 1.456 eV is independent of intensity, suggesting a band-to-defect transition (D-VB or CB-A). Also, as the temperature increases, the peak at 1.456 eV experiences a slight red-shift and becomes indistinguishable above 40 K. The red shift of the PL peak suggests

a band-to-defect transition. This type of transition would require the activation energy of the donor or acceptor to be 150 meV from the respective band (E_g = 1.606 eV, E_{PL} = 1.456 eV, E_g - E_{PL} = 150 meV).

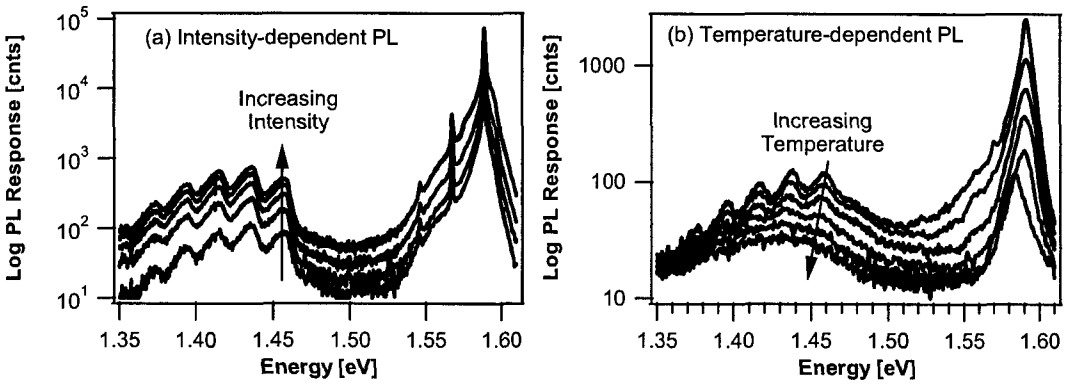

Figure 4.6. PL on sX CdTe with 10 nm, annealed in O_2 at 400°C at (a) different intensities (0.5 - 9.5 W/cm^2) and (b) different temperatures (10, 20, 30, 40, 50, and 77 K).

Although annealing Cu into CdTe in an O_2-containing ambient can create a CuO layer, it is unlikely that this is what is seen in the PL. First, any CuO layer formed would be much thinner than the $1/e$ absorption length of ~200 nm for a 632.8-nm laser in CuO [75]. The real clue, however, is the LO phonon spacing. The LO phonon spacing of the peak at 1.456 eV is 21 meV, consistent with reports for the CdTe LO phonon energy [37]. In contrast, the reported LO phonon energy for CuO is 68 meV, which is 3 times larger than that observed. Hence, the defect at 1.456 eV must originate from the CdTe, and it is most likely due to a complex involving both Cu and O.

4.4 Theoretical Calculations

From the experimental evidence, it was determined that the 1.456-eV peak was related to a complex involving Cu and O and that this donor or acceptor had an ionization energy of 150 meV. First principles band structure calculations were performed to determine the specific complex involved in this PL transition. The scenarios of a defect-free crystal, the two separate cases of Cu or O defects, and the combined case of Cu and O were considered.

The defect-free crystal was first studied to determine the points of low potential - the preferential locations in the crystal where any interstitial defects will form. The results of this calculation (shown pictorially in Figure 4.7) indicated that there are two points of low potential, and both are located along the (111) direction between the Te and Cd ions.

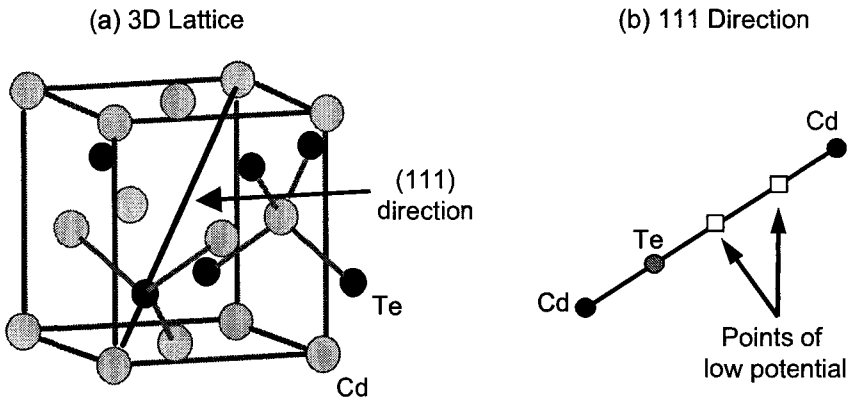

Figure 4.7. Crystal Lattice for defect-free CdTe: (a) 3D lattice and (b) 2D lattice along the (111) direction.

When Cu is incorporated into CdTe, the two most likely defects to form are the acceptor Cu_{Cd} and the donor Cu_i. The formation enthalpy of these two defects is related to the fermi level position by:

$$\Delta H^{D,q}(E_f) = qE_f \tag{4.1}$$

where $\triangle H$ is the enthalpy, q is the electronic charge of the defect, and E_f is the fermi level energy [59]. This relationship is true for compensating materials such as CdTe. As the material becomes more n-type, it is more likely that acceptor levels will form, and as the CdTe becomes more p-type, it is more probable that donors will form. The CdTe used in this study was measured to be p-type, and thus the donor defect Cu_i is more likely to form than the acceptor level of Cu_{Cd}. Therefore, the complex involving both Cu and O will most likely involve a Cu_i ion rather than the Cu_{Cd} substitution. From the first principles band structure calculations, the activation energy of the Cu_i defect by itself is ~10 meV below the conduction band minimum (CBM), and the Cu_i atom is preferentially located next to the Te site along the (111) direction, as seen in Figure 4.8.

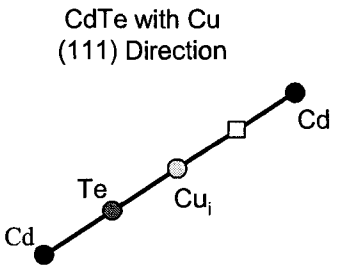

Figure 4.8. Schematic representation of where Cu_i ions preferentially locate in the CdTe lattice.

When oxygen is introduced into CdTe, one of the most easily formed defects is O_{Te}. This is an isovalent defect, i.e., O and Te have the same number of valence electrons. However, an O atom is more tightly bound to its valence electrons than a Te atom, and this

creates a lattice distortion. The isolated O_{Te} defect has an calculated energy of ~200 meV above the CBM.

A Cu_i-O_{Te} defect complex was investigated numerically by placing an O_{Te} defect at the center of a 512-atom supercell and a Cu_i initially placed next to it (the preferred location of Cu_i in the case without O). In this scenario, the Cu_i defect was allowed to move within a 64-atom subcell in the center of the supercell. The results were very similar if the Cu_i were instead allowed to move within the entire 512-atom supercell. The Cu_i defect preferred

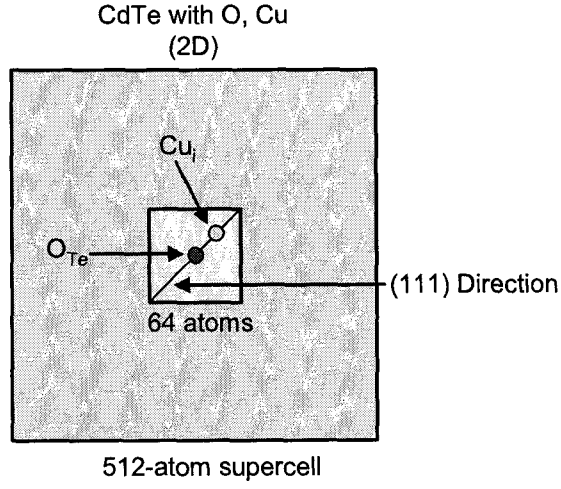

Figure 4.9. Representation of supercell approach used to calculate the activation and binding energies of the Cu_i-O_{Te} donor complex.

to locate next to the O_{Te} (similar position as without O) with a binding energy between the two of about 0.96 eV, indicating that the formation of a defect complex is likely. The calculated activation energy for a Cu_i-O_{Te} donor complex converges to a value of about 125 meV below the CBM. This value is in good agreement with experimental results yielding a defect with energy of 150 meV from the band.

Chapter 5

Detailed Photoluminescence on Polycrystalline Thin-film CdTe Material

The samples used in the thin-film CdTe studies consisted of a glass/SnO_2:F/CdS/CdTe stack, the same structure commonly used in CdTe/CdS solar cells. The samples vary by the type of CdTe deposition—close-spaced sublimation (CSS), vapor transport deposition (VTD), or physical vapor deposition (PVD)—as well as by the fabricating institution. PL was taken on CSS materials from the National Renewable Energy Laboratory (NREL), University of Southern Florida (USF), and the Colorado State University Materials Engineering group (CSU). NREL and USF used small-scale laboratory processes, while CSU used large-scale industrial production processes. VTD samples came from the Institute for Energy Conversion (IEC) and industrial partner "A" (IPA). PVD samples were prepared by IEC.

PL on these samples (no back contact) can be taken from the film side (CdTe surface) or glass side (CdS/CdTe junction region), as shown in Figure 5.1. A baseline was first established on as-deposited CdTe after a 1-hr anneal at 400°C in flowing N_2, with PL taken from the free film surface. The CdTe thin-films were also examined without the anneal, then after a $CdCl_2$ treatment. Finally, some devices were studied with both PL and J-V (current-voltage analysis) after a back contact was applied to complete the device. Some complete cells used ZnTe for the back contact, which allowed PL to be

taken from both the glass and film sides, and others received an evaporated metallic contact that only allowed PL from the glass side.

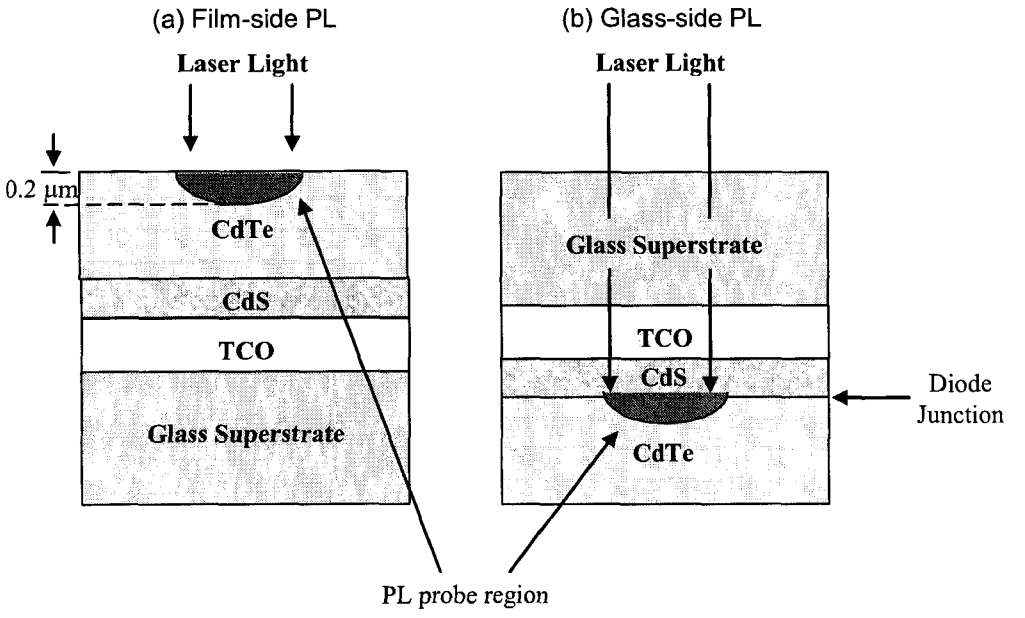

Figure 5.1. Schematic showing the PL probe region for (a) film-side and (b) glass-side (junction-side) excitation.

5.1 Baseline Thin-film CdTe

Figure 5.2a shows the PL at 4.5 K from the film surface of NREL CSS material after the N_2 anneal. The graph denotes the prominent fundamental PL peaks, labeled A-G. The origin of PL peaks are generally determined by studying single-crystal (sX) CdTe, so these peaks will be discussed in terms of what has been seen in sX PL studies. Peaks A and D are commonly seen in single-crystal (sX) CdTe. Peak A, with photon energy 1.588 eV, is assumed to be exciton-related; peaks near 1.588 eV have been previously identified as

an exciton bound to a neutral acceptor (X,A) [53, 76]. Peak D is also similar to a peak seen in single-crystal CdTe at 1.555 eV, which has been identified as a bound exciton (BE), where the binding is to a Cu-related complex, specifically (X, $(Cu_i - V_{Cd})^0$) [42]. Peak B (1.580 eV) and peak E (1.535 eV) have rarely been observed, and little attempt has been made to identify the defects causing these transitions. It has been suggested that peak B is a donor-hole transition (D^0, h) [77], and peak E may be due to residual copper impurities [78]. Peaks C and F (1.567 eV) have, as far as can be determined, not been observed in sX CdTe. They may arise either from differences in the growth method of thin films or may be related to a type of grain-boundary or dislocation defect present in thin-film CdTe.

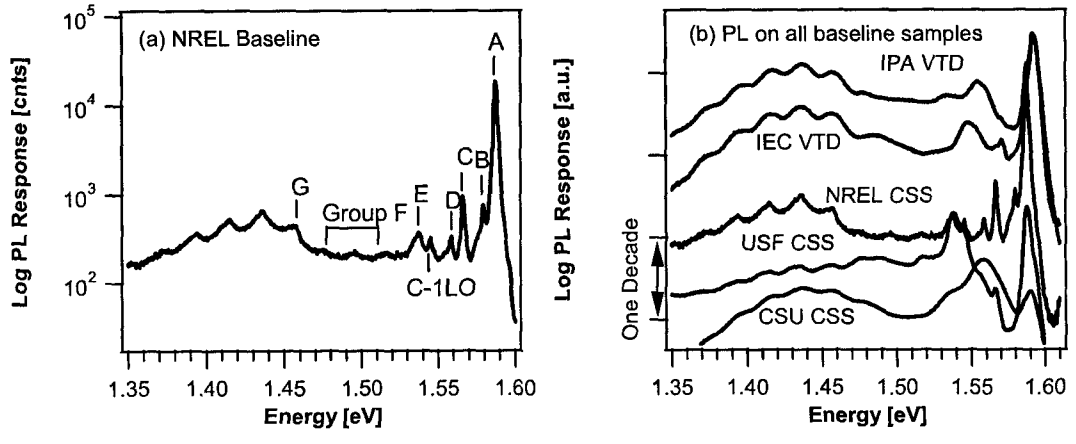

Figure 5.2. Film-side PL on as-deposited thin-film CdTe annealed in N_2 at 400°C for 1hr: (a) Baseline sample produced at NREL; (b) PL on all thin-film samples. Curves offset for clarity.

The peak labeled "G" is the one that will be studied extensively in this thesis. This peak has a photon energy of 1.456 eV and has several distinct LO phonon replicas. Peaks in this general region (1.3 - 1.5 eV) have often been seen in single crystal (sX) CdTe, and the origin of these peaks have been under debate. The two major schools of thought have

either ascribed transitions in this region to Cu_{Cd} acceptors or to the complex Cl_{Te} - V_{Cd}, commonly referred to as the chlorine A-center. In the sX CdTe experiments from Chapter 4, the PL peak at 1.456 eV was only seen after the CdTe has received a "doping" treatment that included both Cu and O, and this defect was assigned as a Cu_i - O_{Te} donor complex. In the thin-film CdTe material, the peak at ~1.46 eV is present from the film side in all samples as deposited (Figure 5.2b) and, as will be seen, persists throughout device fabrication.

	A	B	C	Group D	E	Group F	G
NREL CSS	1.588	1.580	1.567	1.558	1.538	–	1.456
USF CSS	1.587	–	1.566	1.554, 1.544	1.537	1.517, 1.491, 1.476	1.456
CSU CSS	1.590	–	–	1.559	1.538	1.479	1.457
IEC VTD	1.591	1.577	1.570	1.550	–	1.479	1.458
IPA VTD	1.591	–	–	1.554	1.535	–	1.463
IEC PVD	1.589	–	1.570	1.554	1.531	1.475	1.456

Table 5.1. Energy of the ZPLs (in eV) in the PL spectra for CdTe grown at various research institutions

PL from all samples after an N_2 anneal are shown in Figure 5.2b, and the energetic locations of peaks A-G are catalogued in Table 5.1. The PL signatures for the two VTD samples are nearly identical, with only minor differences in the energetic locations in peaks B-F. The PL signatures for the CSS-grown devices vary much more from one institution to the next. All CSS samples share peaks A and G, although the relative intensity of peak A in the CSU CSS sample is reduced by about one order of magnitude. The NREL and USF samples have similar zero-phonon lines for peaks A, C, E, and G (within experimental error); peak group D of the USF sample has one peak shifted by 4 meV from the NREL sample, plus an extra peak at 1.544 eV; and the USF sample exhibits peaks in group F whereas the NREL sample does not. The CSU CSS sample differs from both the NREL

and USF samples in that peak D is the prominent one between peak A and G, and peaks B and C are missing.

Figure 5.3 shows a close-up of Peak G and its phonon replicas for all N_2-annealed thin-film samples. Note that these curves have been offset for clarity. Peak G for the two VTD processes has a similar PL signature, while the overall shape of the PL for the three CSS processes shows quite a bit of variation. However, all samples have a peak at 1.457 ± 0.002 eV. The CSU sample exhibits an additional peak at 1.479 eV. That this peak is unrelated to the 1.457-eV peak will be more clearly seen from intensity-dependent PL.

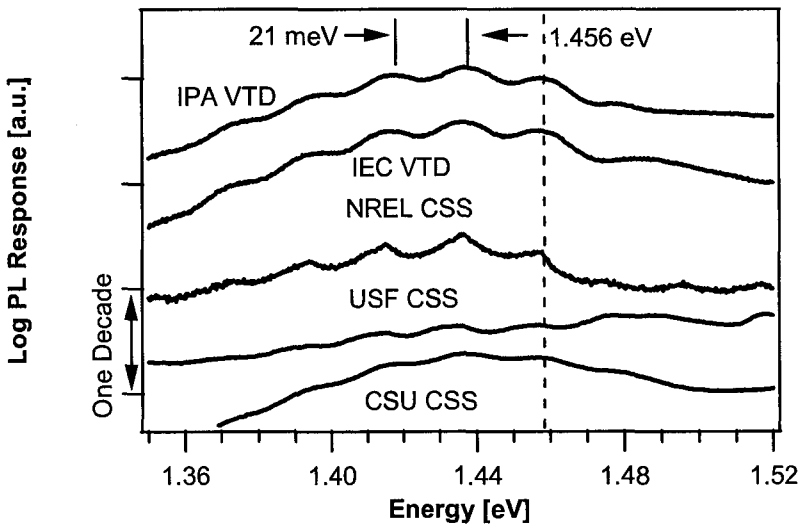

Figure 5.3. Thin-film CdTe after an N_2 anneal. PL taken from the film surface at 4 K with laser intensity 0.5 W/cm^2. Curves offset for clarity.

5.2 PL of CdTe After $CdCl_2$ Treatment

PL was taken for as-deposited CdTe samples, as well as for two types of post-processing conditions: an N_2 anneal at 400°C for 1 h, and a $CdCl_2$ treatment performed at 400°C in

an oxygen-containing ambient. An anneal in N_2 is not a typical process used during device fabrication, but it does allow one to separate the effects of temperature from the effects of the $CdCl_2$ treatment on the PL signature. Figure 5.4 shows PL for these three conditions for the NREL CSS and the Industrial VTD materials. These two materials show the general trend for all the samples, as well as a typical variation. The N_2 anneal in general reduces the overall PL signal. The $CdCl_2$ treatment, on the other hand, increases the overall PL response, indicating that the number of radiatively-recombining transitions has increased. The effect of $CdCl_2$ is more dramatic for the NREL material than for the industrial VTD sample, although this is likely due to the fact that the NREL material has a lower initial response. The fact that the $CdCl_2$ treatment increases the overall PL signal, rather than selectively increasing the 1.456-eV peak (Peak G), suggests that chlorine is not likely to be involved in peak G. The $CdCl_2$ treatment, however, introduces a new peak in the 1.53 - 1.55 eV region, which may well be related to chlorine.

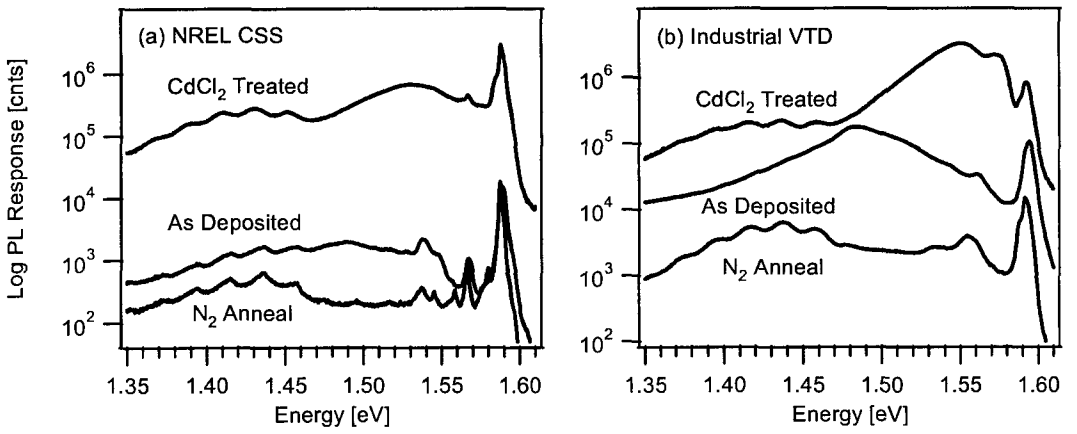

Figure 5.4. PL on polycrystalline CdTe as-deposited, after an N_2 anneal at 400°C for 1 h, and after a $CdCl_2$ treatment for (a) NREL CSS material and (b) an Industrial VTD material.

5.3 Intensity-Dependent and Temperature-Dependent PL

As-deposited thin-film samples were extensively studied using intensity-dependent PL (Figure 5.5). For all the thin-film CdTe samples (examples shown in Figure 5.5), the peak position at 1.456 eV was intensity-independent, which strongly suggests a band-to-defect transition. For VTD-grown samples, the 1.463-eV peak was also intensity-independent. In contrast, the 1.489- and 1.481-eV peaks in the NREL CSS and the VTD samples, respectively, shifted to higher energy with increasing laser excitation. This shift is indicative of a donor-acceptor pair (DAP) transition, and is further evidence that these peaks are not

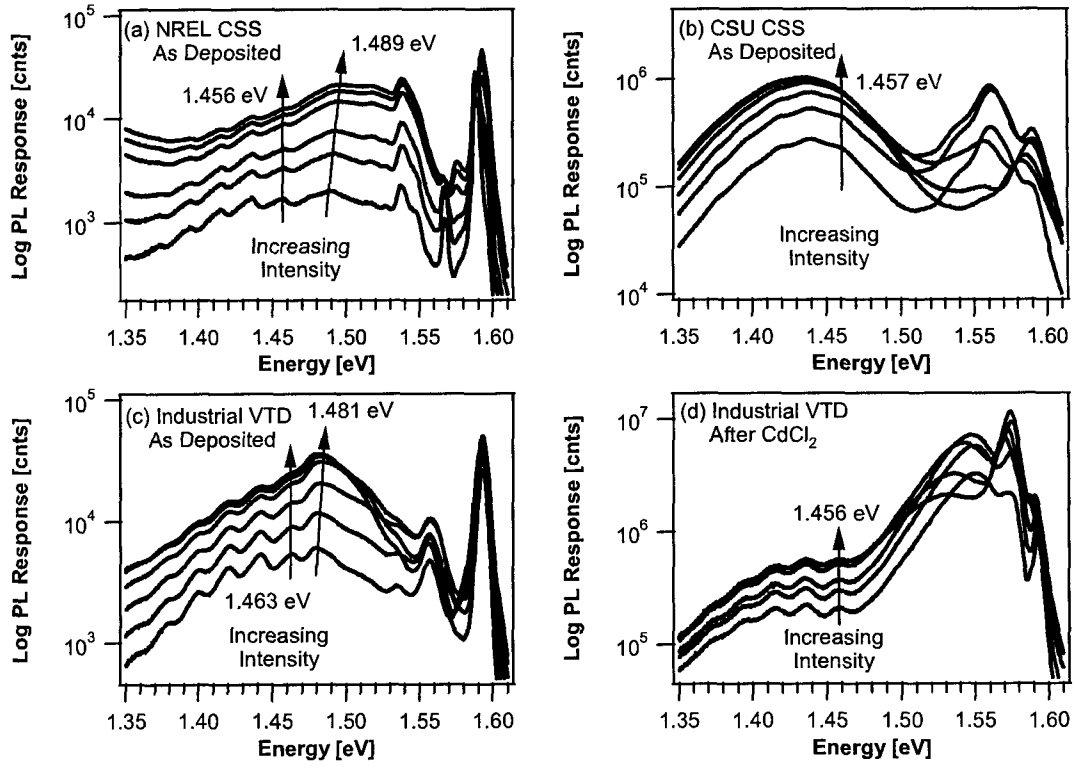

Figure 5.5. Intensity-dependent (0.5 –9.5 W/cm^2) PL at 4.5 K of: (a) as-deposited thin-film CSS CdTe made at NREL, (b) as-deposited thin-film CSS CdTe made at CSU, (c) as-deposited thin-film VTD-grown CdTe, and (d) thin-film VTD-grown CdTe after a wet $CdCl_2$ treatment.

related to the peaks seen at 1.456 and 1.463 eV. The intensity-dependence of the $CdCl_2$-treated sample shown in Figure 5.5d indicated that the position of its 1.456-eV peak also did not shift with increasing power, reinforcing the band-to-defect interpretation.

The intensity-independence argument for the identification of a band-to-defect transition is not completely definitive. Tracking the peak position of these transitions with increasing temperature, however, can help make the interpretation more definitive. Figure 5.6 shows temperature-dependent PL from thin-film CdTe before and after the $CdCl_2$ treatment. The PL peak at 1.456 eV is similar to that for the single-crystal containing both Cu

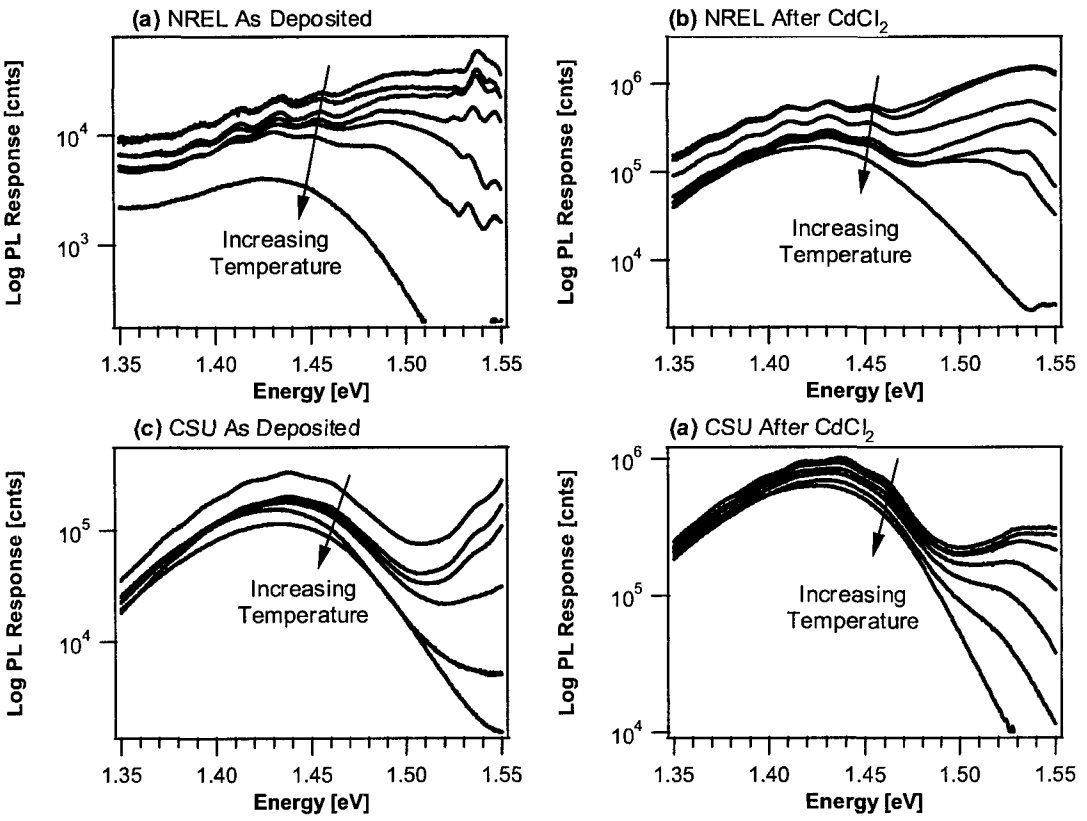

Figure 5.6. Temperature dependence of PL on thin-film CdTe before and after a $CdCl_2$ treatment. (a) NREL CSS as deposited, (b) NREL CSS after $CdCl_2$, (c) CSU CSS as deposited, and (d) CSU CSS after $CdCl_2$.

and O (Section 4.3.2, Figure 4.6), which experienced a red shift and became less distinct with increasing temperature. Again, this is interpreted as a band-to-defect transition.

In addition to possible peak shifts, PL should also show an intensity dependence with temperature, and one would expect the functional form (see Section 2.4, Equation 2.10):

$$I(T) = \frac{I_o}{1 + C_1 T^{3/2} + C_2 T^{3/2} \exp(-E/kT)}$$

where the intensities $I(T)$ and I_o are the area under the curve of the ZPL obtained by fitting the PL spectra. Recall, however, that for defects with ionization energies greater than ~50 meV, the above equation reduces to a dependence only on $T^{3/2}$ ($I_o/I - 1 = C_1 T^{3/2}$). Figure 5.7 shows the fit to the PL intensity changes with temperature for the 1.456 eV peak in NREL as-deposited sample (from data in Figure 5.6a); as expected, it follows the $T^{3/2}$ curve, indicating that the activation energy of this defect is greater than 50 meV. Also, it was not possible to accurately fit the data in Figure 5.7 with either Equations 2.8 or 2.9.

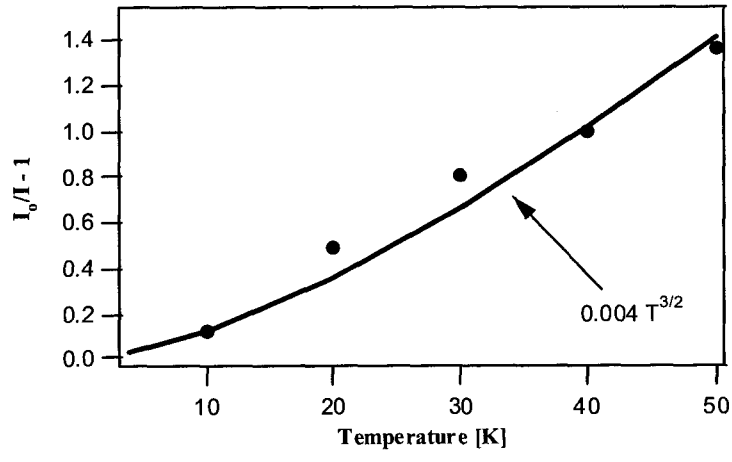

Figure 5.7. Fit to temperature-dependent PL data for the 1.456-eV peak seen in the NREL as-deposited sample. Data points: dots; theoretical fit: line.

The intensity-dependent and temperature-dependent data certainly support the identification of a D-VB transition for the 1.456-eV PL peak in pX thin-film CdTe. This peak is nearly identical to the one seen in sX CdTe only when both Cu and O are incorporated, the PL peak has similar dependence on laser intensity and temperature as for the sX case with Cu and O, and both Cu and O are available in the thin-film CdTe. Hence, it is likely that peak G is caused by the same defect identified in Chapter 4, namely the Cu_i - O_{Te} donor complex.

5.4 CL on Thin-film CdTe

Complementary cathodoluminescence (CL) measurements were taken on an NREL film before and after a $CdCl_2$ treatment. Figure 5.8 shows the CL collected from the film surface (CL scan size 100 nm x 100 nm). The CL was taken at 19 K using 4-pA excitation beam. This is the threshold of sensitivity for this measurement, and is a lower excitation intensity than the PL measurements with laser excitation of 0.5 mW/cm^2. This data has peaks in locations similar to the PL data, with an excitonic peak at about 1.6 eV and a peak near 1.45 eV. Note that the peak near 1.45 eV has a much stronger intensity after the $CdCl_2$ treatment. Also note that the CL signal is somewhat reversed from the PL signal in that the 1.45-eV peak has a greater intensity than the 1.55-eV peak. A final thing to note is that the non-$CdCl_2$-treated sample has a peak at 1.30 eV that was not observed in the PL.

CL maps of the 10000-nm^2 area are shown in Figure 5.9. The response to a specific photon energy can be compared with its corresponding SEM image, allowing one to determine if there are any correlations between the topography and a specific CL transition.

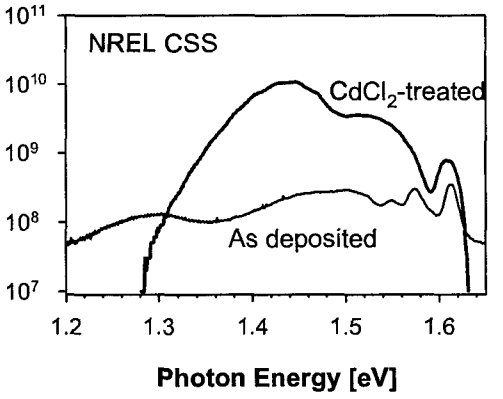

Figure 5.8. Cathodoluminescence over a 100-nm region on NREL CSS material before and after $CdCl_2$ treatment.

Both before and after the $CdCl_2$ treatment, the response of the excitonic peak near 1.6 eV is from the bulk, and very little comes from the intergrain regions. This is expected, since excitons responsible for near band gap peaks are characteristic of bulk CdTe. The response at ~1.45 eV, however, changes dramatically with $CdCl_2$ treatment. Although there is considerable response from the grains at this wavelength, some of the grain-boundary regions also show response that is greater than that from the bulk while other grain boundaries have no response at all. Finally, the CL maps of the 1.30-eV peak help explain why this peak is seen in CL but not in PL. In this map, there are striations along the areas that are creating this peak. This is indicative of a time-delay in the photon release that is longer than the scanning time of the measurement. This is likely due to charging of the sample during the measurements. The 1.30-eV peak did not appear in PL because it was not excited when the light-induced electron-hole pairs recombined; however, during CL measurements, this defect is charged and then directly releases its electron to create a photon with energy 1.30

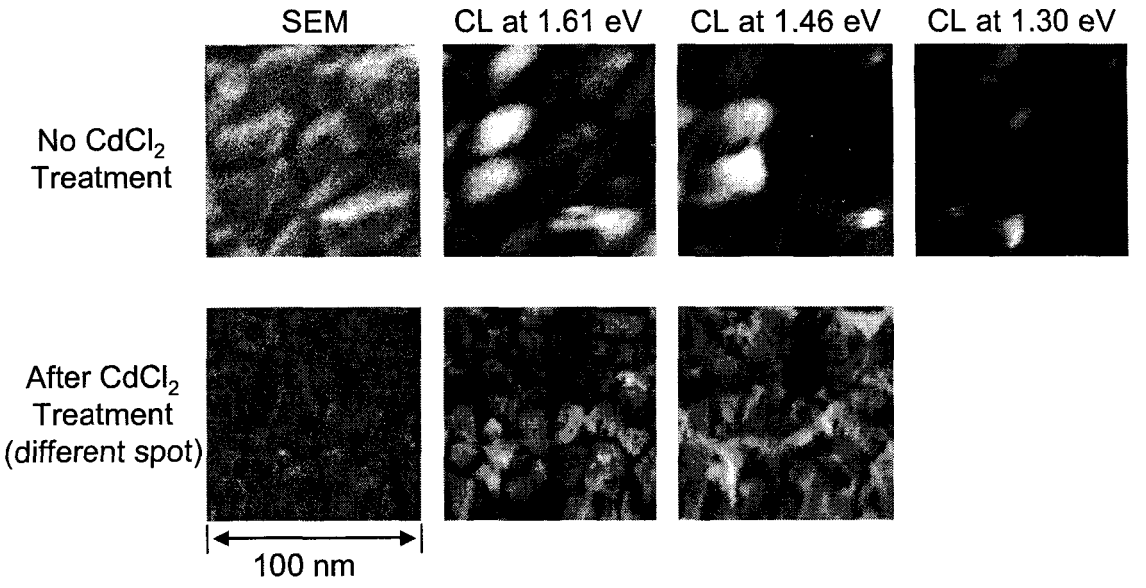

Figure 5.9. Cathodoluminescence maps of selected photon energies and the corresponding SEM images (NREL CSS).

eV. Thus, with CL it is possible to detect an electronically active defect with energy of 300 meV that could not be seen with PL techniques.

5.5 Glass Side Versus Film Side PL

The PL data shown so far in this chapter was taken from the free CdTe (film) surface. PL taken from the glass side (see Figure 5.1) of these samples does not always reveal the same PL signatures as seen from the CdTe film surface. As can be seen in Table 5.2, the peak at ~1.46 eV observed from the film side is not clearly present from the glass side for most samples. Only for the thinnest films (IEC PVD and CSU CSS) is the ~1.46 eV peak observed when PL is taken from the glass side of the sample. In general, the $CdCl_2$ treatment further obscures the PL peak from the glass side for all samples.

	Process	CdTe Thickness	Film Side G (eV)	Clarity of G through Glass
IEC PVD	As Deposited	1.5 μm	1.456	Strong
CSU CSS	As Deposited	2 μm	1.457	Strong
IPA VTD	As Deposited	4 μm	1.463	Weak
IEC VTD	As Deposited	6 μm	1.458	Weak
USF CSS	As Deposited	8 μm	1.456	Obscure
NREL CSS	As Deposited	8 μm	1.456	Obscure
IEC PVD	$CdCl_2$-treated	1.5 μm	1.456	Strong
CSU CSS	$CdCl_2$-treated	2 μm	1.456	Weak
IPA VTD	$CdCl_2$-treated	4 μm	1.456	Obscure
IEC VTD	$CdCl_2$-treated	6 μm	1.456	Obscure
USF CSS	$CdCl_2$-treated	8 μm	1.456	Obscure
NREL CSS	$CdCl_2$-treated	8 μm	1.456	Obscure

Table 5.2. PL transitions seen from the free film surface are not always apparent from the glass side.

Also, thicker devices tend to show weaker PL transitions from the CdTe layer. There are two possible explanations for this trend: (i) the defect at ~1.46 eV has a higher concentration at the free film surface than at the junction region, and the concentration at the junction region is not sufficient to produce a PL signal; or (ii) samples with thicker CdTe form a thicker CdSTe layer that obscures the PL signal. This obscuring of the PL from the intermixed CdS_xTe_{1-x} layer occurs because, for certain values of x, the band gap is smaller than that for CdTe (see Figure 5.10, taken from Ref. [79]). Thus, this mixed layer will participate in the PL taken from the glass side of the device, and band gap variations will be reflected in the PL energies. Hence, laser light absorbed in the intermixed layer may complicate analysis of the PL signal from the CdTe layer. Glass-side PL will be revisited when looking at contacted samples (complete CdTe devices), where it is not usually possible to take PL through the contact.

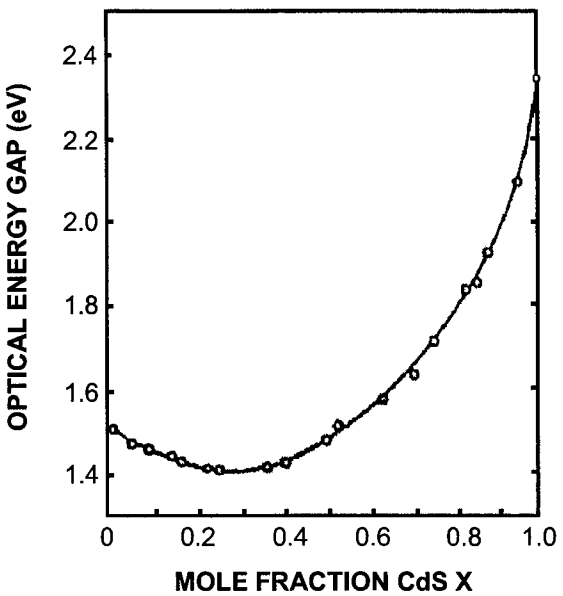

Figure 5.10. CdS_xTe_{1-x} band gap as a function of x at 300 K.

5.6 PL on CdTe Devices and Links to Performance

When PL is taken on completed devices, the preference is to take data from the glass side. One practical reason is that most back contacts are opaque, making PL from the back of the film impossible. An exception is the ZnTe contact, which can be made transparent by removing the outer Ti layer. A more important reason for taking PL from the glass side of completed devices is that this allows one to take PL in the region where the junction forms, and any insight gleaned from looking at defects in this region has the possibility of directly correlating to device performance. As discussed in Section 5.5, for the samples thicker than 3 μm (after $CdCl_2$), it is more difficult to resolve the ~1.46 eV peak when PL is taken through the glass. However, this changes once the sample receives a back contact, and hence more Cu in the sample. Figure 5.11 shows the differences between film-side

and glass-side PL for the industrial VTD sample (CdTe thickness: 4 μm). Note that, from the film side, the peak at 1.456 eV is present in all stages of sample preparation; however, the scale used does not clearly bring out the distinct phonon replicas for the as-deposited and contacted samples. From the glass side (Figure 5.11b), there is no evidence of a peak at 1.456 eV after deposition. After $CdCl_2$ (low-purity $CdCl_2$ / O_2 treatment), glass-side PL reveals a shoulder in the 1.4 - 1.45 eV region, and contacting brings out this peak. Figure

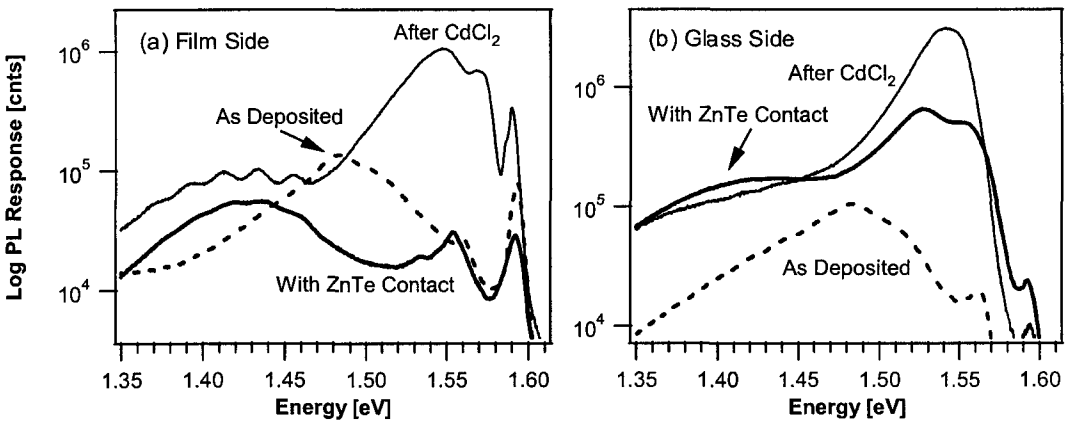

Figure 5.11. PL on Industrial VTD material as deposited, $CdCl_2$-treated, and ZnTe-contacted CdTe, with Ti removed (a) from the film side and (b) from the glass side.

5.12 represents the same data, with the focus on comparing the glass-side and film-side PL from the contacted sample. Note that the peak from the glass side in the 1.4 - 1.45 eV region lines up reasonably well with the 1.456-eV peak seen from the film side. In this and most samples, there are no distinct phonon replicas from the glass side; however, in the few cases where phonon replicas are visible from the glass side, they line up perfectly with the film-side PL peak at 1.456 eV. Hence, it is fairly certain that this broad peak seen from

the glass side PL after contacting is, in fact, the 1.456-eV peak that was seen from the film side after deposition.

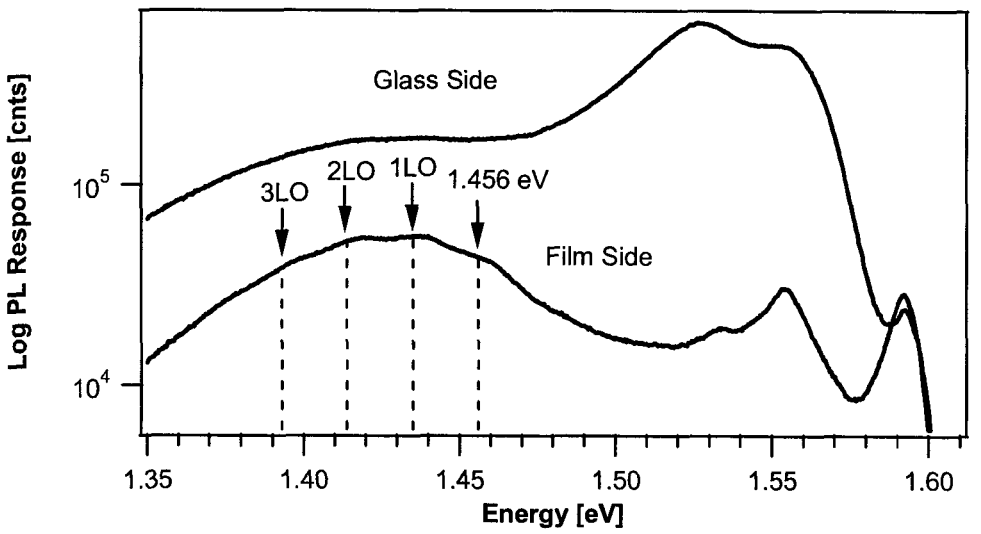

Figure 5.12. Film-side and glass-side PL on ZnTe-contacted Industrial VTD material (outer Ti layer removed).

Figure 5.13 shows side-by-side comparisons of J-V and glass-side PL (junction region) from devices with a ZnTe back contact; the amount of Cu included in these contacts was varied from approximately 0.1 - 1 nm. For the 2-μm-thick CdTe device (CSU CSS), the PL shows the 1.456-eV peak prior to contacting. After contacting, the overall PL intensity decreases, but the relative intensity of the 1.456-eV peak is unchanged. The reduced PL intensity could result from an increase in the junction field, which would serve to sweep carriers out of the junction region very quickly, reducing the number of radiative PL transitions that might occur. The corresponding J-V indicates that adding Cu, up to a certain amount, improves device performance, but "excessive" Cu reduces the efficiency of the device. The initial increase in performance could be due to the formation of a better

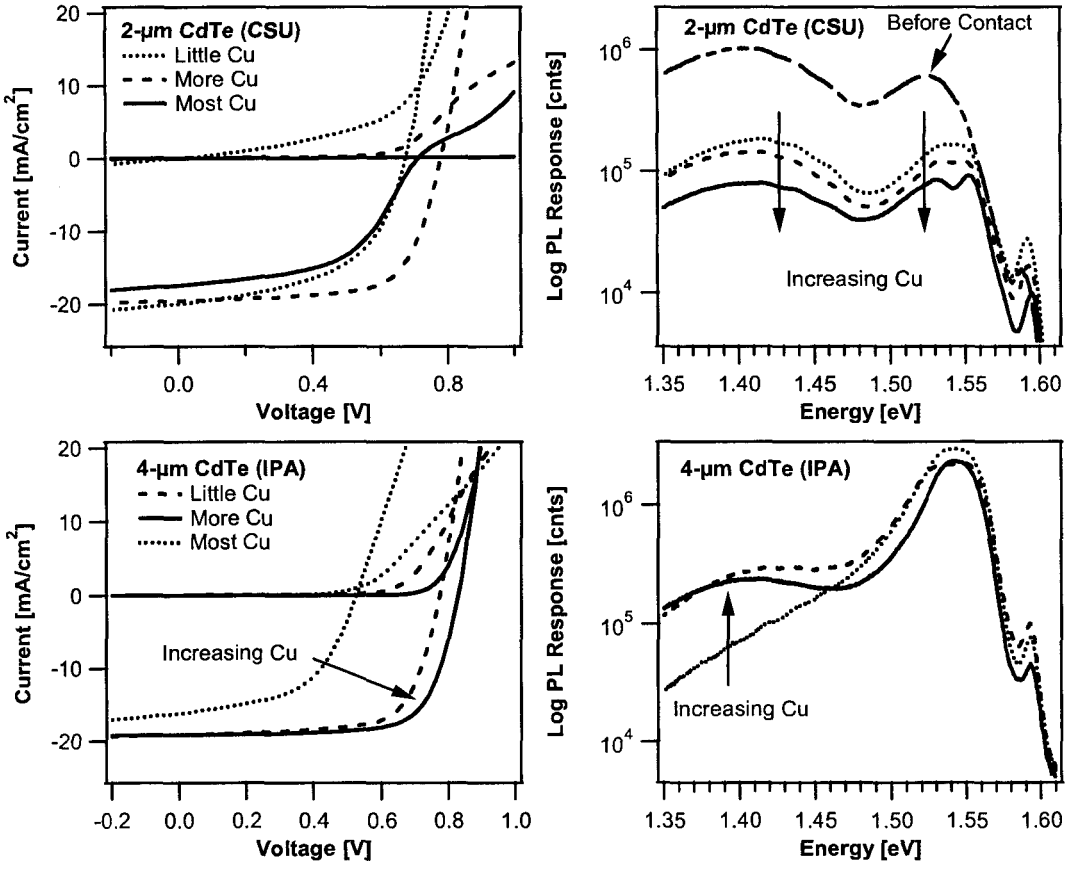

Figure 5.13. J-V and glass-side PL for ZnTe-contacted devices with CdTe thickness of 2 and 4 μm. Approximately 0.1 - 1 nm Cu were included in the back contact process.

back contact by incorporating Cu, or by the formation of Cu_{Cd} acceptors in the CdTe. These explanations, however, do not account for the decrease in efficiency when there is "excessive" Cu. In the case of the thin-CdTe device (2 μm), there is no clear link between the 1.456-eV peak and device performance; however, this could be because the peak is visible from the glass side immediately after deposition (see Table 5.2 in Section 5.5). In the case of the 4-μm-thick CdTe device (IPA VTD), there is a very strong correlation between the 1.456-eV PL peak and the J-V performance. Note that, as Cu is added to the

back contact, the 1.456-eV peak increases in relative intensity, and the J-V curve improves in both V_{oc} and FF. The 4-μm-thick CdTe device does not exhibit a decrease in device efficiency after more Cu is added. However, recall that the amount of Cu being added is very small (maximum of 1 nm Cu), and it is likely that more Cu would be required in the 4-μm-thick device than in the 2-μm-thick device in order to see the same trend.

Figure 5.14 shows J-V versus PL on NREL evaporated-contact devices. In this study, one contact was evaporated without Cu, and other contacts received 5, 20, and 40 nm Cu. For these devices, the most dramatic changes in both PL and J-V occur when the contact changes from no Cu to 5 nm Cu. Once Cu is added to the contact, the PL experiences a drastic reduction in overall PL intensity, again consistent with an increase in the junction field, and the J-V performance increases, mostly in V_{oc} and FF. In the PL signal, the 1.456-eV peak is not discernible until after Cu is added. As more Cu is added, the PL spectra does not change appreciably, and the J-V performance decreases, mostly through a loss in V_{oc}.

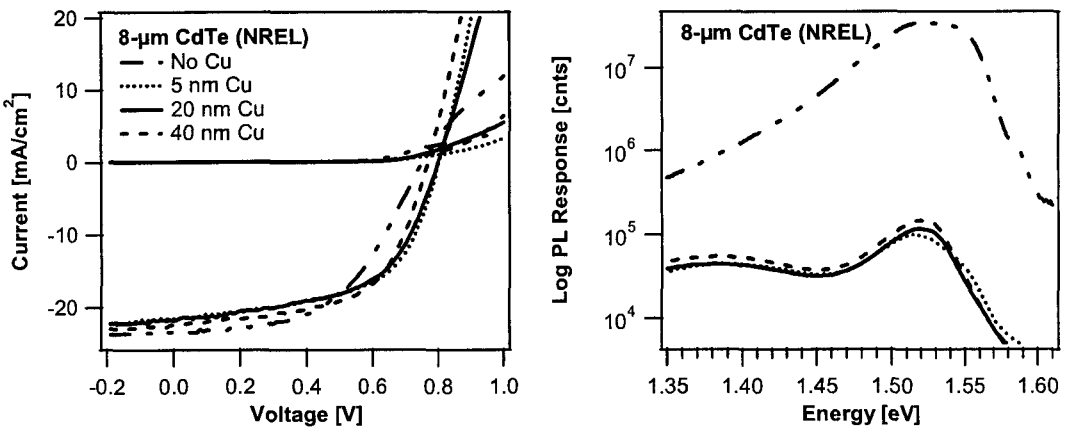

Figure 5.14. J-V and glass-side PL for NREL evaporated-contacted devices with CdTe thickness of 8 μm.

Note that the trend for the 8-μm-thick device is similar to that for the 2-μm-thick device in Figure 5.13a, but the 8-μm-thick device had about an order of magnitude more Cu than the 2-μm-thick device. This suggests that the amount of Cu considered to be "excessive" may vary with CdTe thickness.

It is apparent that the effect of the 1.456-eV PL peak on device performance varies with the thickness of the CdTe layer. For 4- and 8-μm devices, the formation of the peak (from the glass side) correlates with higher-performance devices, specifically to an increase in V_{oc} and FF. For the 2-μm device, the link between the 1.456-eV PL peak and device efficiency is not as strong. However, this link may be more difficult to see since the peak is already visible from the glass side prior to contacting.

The increase in device efficiency for a compensating donor in the junction region of a device is counter-intuitive. There are several possible explanations for this trend: (1) Including Cu in the contact improves the electrical contact of the device; (2) Cu from the contact forms Cu_{Cd} acceptors in the CdTe that are not necessarily seen in the PL; (3) the Cu_i - O_{Te} donor complexes takes the place of a worse defect. In all likelihood, all three processes are occurring, but the following discussion focuses on the last one.

During CdTe growth, it is believed that V_{Te} defects form easily. This vacancy is a nearly mid-gap defect at room temperature (E_C - 0.71 eV [63]) that acts as a recombination site for carriers, preventing them from being collected. As the Cu_i - O_{Te} complexes form, it is energetically favorable for the O to locate on the vacant Te sites rather than to replace occupied Te sites. Thus, it is likely that the Cu_i - O_{Te} donor complex is partially replacing the mid-gap V_{Te} defects, as shown in Figure 5.15.

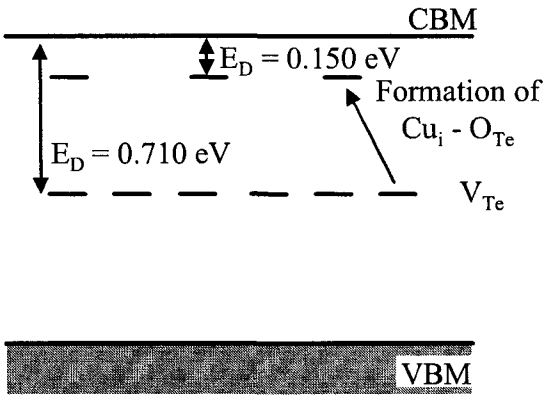

Figure 5.15. Representation of the locations of V_{Te} and Cu_i - O_{Te} defects within the CdTe band gap (Room Temperature).

The scenario that Cu_i - O_{Te} donors are replacing mid-gap V_{Te} defects was investigated using AMPS-1D simulations. The starting point was the baseline case for CdTe [67], which has a mid-gap defect [E_D = 750 meV] with concentration N = 2 x 10^{14} cm^{-3} and no donor-level defects at E_D = 150 meV. Two different cases were investigated: In Case I, the mid-gap defect concentration was decreased from 2 x 10^{14} cm^{-3} to 0 (varied across 10^{14} range), and no other donor-level defects were introduced; in Case II, the concentration of the mid-gap defect was decreased while the concentration of the donor at 150 meV increased, and the sum of the concentrations of the two defects was fixed at 2 x 10^{14} cm^{-3}.

Simulation results, shown in Figure 5.16, indicated that decreasing the concentration of the 750-meV defect (N_{750meV}) improves V_{oc} and FF (ΔV_{oc} = + 10 mV, ΔFF = +9 %), which improves the overall device efficiency. However, transferring an equal amount of defects to the donor level at 150 meV as the 750-meV defect concentration decreases (Case II) dramatically reduces the V_{oc} and limits the increase in FF (ΔV_{oc} = - 90 mV, ΔFF = +5 %). The increasing FF from the mid-gap defect and the decreasing V_{oc} from the 150-meV

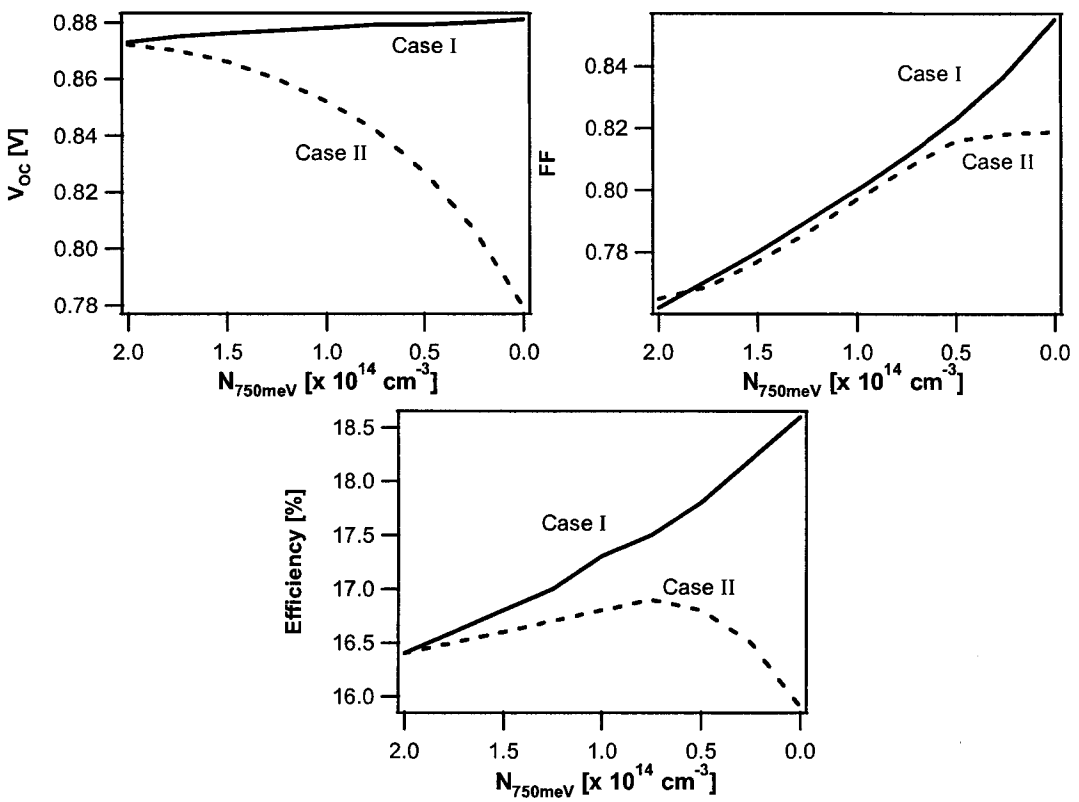

Figure 5.16. J-V parameters from AMPS simulations. Case I decreases the concentration of a 750-meV defect from 2 x 10^{14} cm^{-3} to 0 without introducing other defects. Case II decreases the concentration of a 750-meV defect while increasing the concentration of a 150-meV donor level by an equivalent amount.

donor level act as competing mechanisms: initially, there would be a slight increase in efficiency (from increase in FF), then the efficiency would decrease at a rapid rate (from a decrease in V_{oc}).

It is worth noting that although the simulation results would explain the trends for the cases of "excessive" for the 2-μm and 8-μm devices in Figure 5.13 & Figure 5.14, the initial device efficiency increases (all thicknesses) is not qualitatively the same for the simulations and actual devices. In the simulations, the device efficiency comes primarily from an

increase in FF (but V_{oc} decreases), whereas in real devices the increase in efficiency comes primarily through an increase in V_{oc} (only slight increase in FF). Thus, the simulation results indicate that the increased device performance is not solely due to formation of Cu_i - O_{Te} defects, but is more complicated, likely involving an improvement in electrical contact by incorporating Cu, the formation of Cu_{Cd} acceptors in the CdTe, and/or a change in the depletion width of the device. Initially the formation of Cu_i - O_{Te} is fairly benign because it replaces mid-gap V_{Te} and there are simultaneous improvements from other mechanisms, but as more Cu is incorporated and the donor-level concentration becomes greater than 1.2 x 10^{14} cm^{-3} (from simulations), it will reduce device efficiency. This trend corresponds to the "excessive Cu" cases where there are significant V_{oc} losses. However, it is possible that the reduction in efficiency (and V_{oc}) is also caused by Cu forming compensating Cu_{Cd} acceptors in the CdS (n-type) layer of the device [26].

For small concentrations, the effects of the Cu_i - O_{Te} defect on the performance of devices is likely small, but for larger concentrations it can dramatically limit the V_{oc} and, hence, device efficiency. It is important to note that, if the V_{Te} vacancy could be neutralized without forming such a compensating donor, then there would be a dramatically increased device performance. It would be ideal to minimize formation of V_{Te}. Alternately, replacing any V_{Te} with an acceptor, such as the chlorine A-center, Cl_{Te} - V_{Cd} (E_V + 140 meV), would be advantageous. In this sense, the presence of the Cu_i - O_{Te} donor complex may limit the possible attainable device efficiency in CdS/CdTe solar cells.

5.7 PVD Devices: Structural Variations

PVD devices, because they are grown at much lower temperatures than either the CSS or VTD process (200°C compared to 600°C), have unique properties, one of which is observed in luminescence. Figure 5.17a shows PL on as-deposited PVD devices from the film and glass sides of the sample. The location of the ZPL for peak G varies slightly from the glass side to the film side; the ZPL on the film side is blue shifted by 4 meV from the glass side location. Note that the spacing between the ZPL and phonon replicas from the glass side is 21 meV, as is expected for CdTe. From the film side, however, the phonon replica spacing is ~24 meV. After a $CdCl_2$ treatment, shown in Figure 5.17b, the glass- and film-sides ZPLs and LO phonon replicas line up perfectly. We believe that the change in LO phonon energy as well as the blue shift in peak location can be attributed to a difference in the phase of CdTe.

CdTe typically grows in the zincblende phase, which is the stable phase at atmospheric pressure (a = 6.482 Å) [37]. However, it has been documented that one or more layers of CdTe can grow in the metastable wurtzite phase (a = 4.58 Å, c = 7.54 Å) [80]. Grazing Incidence X-ray Diffraction (GIXRD) measurements performed at IEC (data not shown) show the existence of a wurtzite layer approximately 1000 Å thick, with the remaining CdTe in the zincblende phase.

The probing depth of the PL measurement at this laser wavelength is also approximately 1000 Å thick, thus it is likely that the film-side PL measurement is probing only CdTe in the wurtzite phase. It is certainly possible that the different phase of CdTe would have a different LO phonon energy. This would also explain why the glass-side PL has the

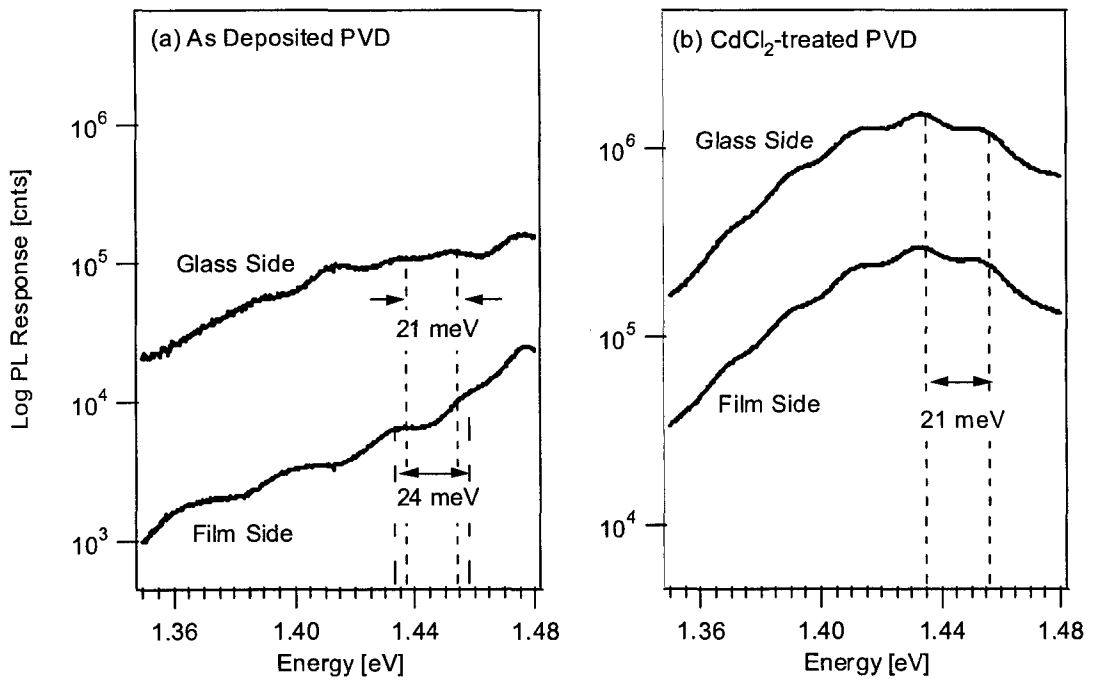

Figure 5.17. PL on PVD samples from the glass and film sides for (a) as deposited CdTe and (b) $CdCl_2$-treated CdTe.

expected value for the LO phonon energy, since it is in the typical zincblende phase. Additionally, the band gap for the wurtzite phase of CdTe is greater than that for the zincblende phase [81], which would account for the blueshift in the PL peaks when going from the glass to film side of the sample. GIXRD further shows that, after a $CdCl_2$ treatment at 400°C, there is no evidence of a wurtzite layer at the CdTe film surface. This suggests a change in phase at the CdTe film surface with the heat treatment, and agrees with the PL data showing that there is no difference in the PL from the glass and film sides after the $CdCl_2$ treatment.

Chapter 6

Discussion and Conclusions

Photoluminescence (PL) studies on as-deposited thin film CdTe samples revealed a peak at 1.46 eV (CdTe film side) that was not seen in as-grown single-crystal (sX) CdTe samples. This peak at 1.46 eV was reproduced in sX CdTe only when both Cu and O were incorporated. The intensity-dependence of the PL suggests a defect-to-band transition. Both the intensity-dependent and temperature-dependent PL for the 1.46 eV peak were very similar for the Cu/O sX CdTe and the as-deposited thin film CdTe samples. The thin-film samples were grown in an O_2 ambient, with Cu as a source impurity during the growth process. Therefore, it is very likely that the peak at 1.46 eV in the thin film samples is caused by the same defect as for the single crystal sample. First-principals-band-structure calculations, taking into account that both Cu and O were necessary to produce the PL peak and that it was a band-to-defect transition, identified the transition as being from a Cu_i - O_{Te} donor complex 150 meV below the conduction band to the valence band.

PL was taken on thin-film CdTe after an anneal in $CdCl_2$ and after a back contact process. The $CdCl_2$ treatment enhanced the entire PL, but did not selectively increase the peak at ~1.46 eV. This is fairly strong evidence that Cl is not responsible for the 1.46 eV peak. Contacting processes including Cu caused a peak similar to the 1.46 eV peak to be seen from the glass side of the solar cell (CdS/CdTe junction region) for samples with CdTe thickness greater than 4 μm. If Cu was not included in the contact process,

this peak did not form in the junction region of the solar cell. This again points to Cu as one of the necessary dopants for the formation of this defect. Although solar cell performance increases as the PL signal of this defect increases, this increase is probably coincidental, with the increase in device performance caused by various changes in the defect spectrum of the CdTe that serve to increasing the acceptor concentration at the back of the CdTe and form a better contact when Cu is incorporated.

Formation of a donor complex would create a limitation on the maximum attainable V_{oc} in CdTe solar cell devices. However, this effect may not have been previously noted since beneficial processes, such as the crystal growth benefits from oxygen, improvement of carrier collection by including Cu in the back contact, and formation of acceptors in the CdTe layer, occur simultaneously. If the Cu_i - O_{Te} donor complex could be eliminated without losing the other beneficial processes, then the overall device efficiency of CdS/CdTe solar cells should be improved.

Suggestions for Future Work

The possibilities for future work fall into three categories: (1) to perform experiments to test the assumptions made when determining the possible effects of the Cu_i - O_{Te} defect on device performance, (2) to perform device simulations, and (3) to take the conclusions about the Cu_i - O_{Te} defect and apply it to device processing.

There were two basic assumptions that led to the conclusion that the Cu_i - O_{Te} defect is detrimental to device performance. The first assumption is that the mid-gap V_{Te} defect is present in thin-film materials. Although there has not been direct evidence of the V_{Te}

defect, XPS data (Appendix B) suggests that single crystals are Cd-rich, which suggests that growth conditions may be appropriate for the formation of V_{Te} in the lattice. Some scientists at NREL have observed, but have not published results, that thin-film CdTe is also CdTe-rich. The second assumption is that Cu_i - O_{Te} replaces the mid-gap V_{Te}. A direct observation of a V_{Te}-related PL transition has not been observed, presumably because mid-gap states tend to act as recombination sites, thus do not produce radiative recombination. Perhaps future studies using other techniques, such as Deep Level Transient Spectroscopy (DLTS) or Drive Level Capacitance Profiling (DLCP), could track the concentration of V_{Te} in CdTe devices with and without Cu (or with and without oxygen) to determine if, in fact, the number of V_{Te} reduce with different processing.

Although some device simulations were made using AMPS-1D, they were limited to exploring the replacement of V_{Te} with Cu_i - O_{Te} instead of simply reducing the number of V_{Te}. A more thorough study could include back contact effects, doping of the back part of the CdTe layer, and simultaneous addition of Cu_{Cd} in the CdS layer. These simulations may provide a better fit to the experimental data, and would more accurately study the quantitative contribution of the Cu_i - O_{Te} defect to device performance.

The assertion that a Cu_i - O_{Te} donor complex exists and is limiting device V_{oc} leads one to the conclusion that it would be desirable to rid the device of these defects. There are at least two possible ways to attack this problem: (1) concentrate on eliminating the oxygen, which takes the place of V_{Te}; or (2) reduce the number of V_{Te} in the as-grown crystal, thereby restricting the number of Cu_i - O_{Te} defects that can form. Although the first method may seem to contradict many studies that show oxygen is necessary for good

cell performance, oxygen was primarily introduced during the growth process to reduces pinhole formation that, if unchecked, lead to contact problems. Since the oxygen decreases the grain size, its use reduces the chance of forming shunt paths when metal contacts were applied. However, recently-developed contact architectures, such as SbTe or ZnTe contacts, may be able to circumvent this problem. Also, it may be advantageous to look at growth methods other than CSS or VTD that do not require oxygen in the ambient to form smaller CdTe grains. These oxygen-free processes may result in a CdTe film that yields more V_{Cd} - Cl_{Te} acceptors (A-center) than oxygen-containing films.

The second strategy, to reduce the number of V_{Te} produced in the crystal during growth, is perhaps more desirable because it would eliminate the mid-gap defect as well as prevent the formation of the Cu_i - O_{Te} donor complex. Improved control of this defect concentration may be achieved by adjusting the Cd/Te ratio, perhaps by using a Te overpressure. This approach has some precedent in $CuInGaSe_2$ technology, where good devices require Se overpressures to reduce the concentration of V_{Se} defects. However, the strategy to passivate V_{Te} would be accompanied by the near certainty that all of the post-growth processes would need to change significantly in order to produce high-efficiency devices. The ability to alter (or eliminate) some of the post-deposition processes could provide significant cost advantages in the next generation of CdS/CdTe production modules. Hence, this may be the route to pursue in order to achieve CdS/CdTe devices with sufficient efficiencies to have a significant role in future solar energy production.

APPENDIX A Using the Hydrogenic Defect Model to Calculate Defect Energies

The hydrogenic defect model treats shallow donors and acceptors as hydrogen atoms, where donors have a positively-charged nucleus with one orbiting electron and acceptors have a negatively-charged nucleus with one orbiting hole. This method can also be used to obtain the energy of the free exciton, and this will be shown after the derivation for the shallow donor and acceptor states. The hydrogenic defect model tends to underestimate the binding energy.

A.1. Shallow Donors and Acceptors

Figure A.1 shows how the nucleus and free electron would be represented in the hydrogenic model, with r as the physical distance between the nucleus and the orbiting electron.

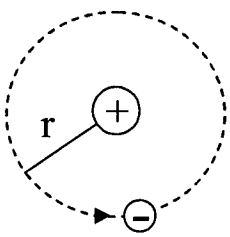

Figure A.1. Schematic drawing of the hydrogenic model for a donor.

The energy of the electron for the donor (or hole for the acceptor) can be written as:

$$E = \frac{\hbar^2 k^2}{2m^*} - \frac{q^2}{4\pi\epsilon r} \tag{A.1}$$

Here, m* is the effective mass of electrons if calculating a donor level or it is the effective mass of holes if calculating an acceptor level, and ϵ is the permittivity of the material. Assuming the net force on the electron is simply the electrostatic force between the nucleus and the electron, Newton's 2^{nd} Law can be written as:

$$-\frac{q^2}{4\pi\epsilon r^2} = -\frac{m^* v^2}{r} \tag{A.2}$$

The speed is $\hbar k/m^*$, so Equation A.2 can be rewritten as:

$$\frac{q^2}{2(4\pi\epsilon r)} = \frac{\hbar^2 k^2}{2m^*} \tag{A.3}$$

If we put this back into Equation A.1, it becomes:

$$E = -\frac{q^2}{2(4\pi\epsilon r)} \tag{A.4}$$

The next step is to calculate the orbital radius, r, in terms of known constants of the material. Since the circumference of the orbit of the electron is an integral number of the wavelength, $2\pi r = n\lambda$, and $\lambda = \frac{2\pi}{k}$, then $k = n/r$. If this is put into Equation A.3 and solved for r, then

$$r = \frac{4\pi\epsilon n^2 \hbar^2}{m^* q^2} \tag{A.5}$$

Substituting this into the the energy expression, the binding energy of the electron to the donor is:

$$E = -\frac{m^* q^4}{2(4\pi\hbar)^2 \epsilon^2 n^2} \tag{A.6}$$

The Rydberg energy, R_H, is

$$R_H = -\frac{m_o q^4}{2(4\pi\hbar\epsilon_o)^2} = -13.6 \text{ eV} \tag{A.7}$$

where m_o is the mas of an electron and ϵ_o is the permittivity of free space. Thus, the binding energy can be written solely in terms of material properties and other constants.

The so-called activation energy of a donor, or the energy to remove an electron from its donor, has opposite sign to the binding energy:

$$E = \frac{m^*}{m_o}\left(\frac{\epsilon_o}{\epsilon}\right)^2 \frac{1}{n^2}(13.6 \text{ eV}) \tag{A.8}$$

In CdTe, $\epsilon \approx 10\epsilon_o$, and the effective mass for electrons (m_e*) and for holes (m_h*) are approximately 0.1 m_o and 0.8 m_o, respectively. The activation energies for the shallow donor and acceptor states in CdTe are:

$$E_D = \frac{0.1m_o}{m_o}\left(\frac{\epsilon_o}{10\epsilon_o}\right)^2 \frac{1}{n^2}(13.6 \text{ eV}) = 13.6 \text{ meV}\frac{1}{n^2} \tag{A.9}$$

$$E_A = \frac{0.8m_o}{m_o}\left(\frac{\epsilon_o}{10\epsilon_o}\right)^2 \frac{1}{n^2}(13.6 \text{ eV}) = 108.8 \text{ meV}\frac{1}{n^2} \tag{A.10}$$

Recall that $n = 1$ corresponds to the ground state of the electron or hole. Note that the activation energy of the acceptor is much higher than for the donor because the effective hole mass is greater than the effective electron mass.

A.2. Free Excitons

Unlike donors and acceptors, the free exciton is not a lattice defect and does not have an activation energy. However, it is possible to use a quasi hydrogenic defect model to calculate the energy difference between the band-to-band energy and the exciton energy. Then this energy difference can be subtracted from the band gap to find the energy of the free exciton.

In the case of the free exciton, both the positive and negative charges are in orbit. The process outlined above can still be used if we change to center of mass coordinates

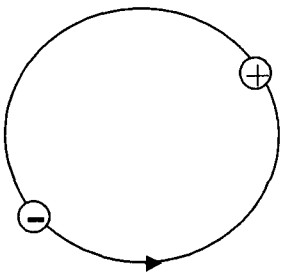

Figure A.2. Schematic drawing of a free exciton.

($r \longrightarrow \vec{r}_e - \vec{r}_h$) and use the reduced effective mass, m_r* ($\frac{1}{m_r^*} = \frac{1}{m_e^*} + \frac{1}{m_h^*}$). Thus, the result from Equation A.8 can be adapted simply by changing m* to m_r*.

$$E_{exc} = \frac{m_r^*}{m_o}\left(\frac{\epsilon_o}{\epsilon}\right)^2 \frac{1}{n^2}(13.6\text{ eV}) = \frac{0.089 m_o}{m_o}\left(\frac{\epsilon_o}{10\epsilon_o}\right)^2 \frac{1}{n^2}(13.6\text{ eV}) = 12.1\text{ meV}\frac{1}{n^2} \quad \text{(A.11)}$$

For a free exciton in the ground state in CdTe, the energy at 4 K is then

$$E_{FE} = (1.606 - 0.0121)\text{ eV} = 1.593\text{ eV} \quad \text{(A.12)}$$

Observations of the free exciton in CdTe show that the energy is actually ~1.597 eV [82].

APPENDIX B Effects of BrMe and Annealing on PL of Single-crystal CdTe

Control samples were fabricated to investigate the effects of annealing and BrMe-etching on PL response, and to determine whether or not the annealing process used here changes the PL of the single crystal CdTe. Since the preparation of Cu-diffusion samples includes an annealing process, it is necessary to show that the anneal itself is not the contributing factor to changes in the PL signal. Data for the non-etched and 1% BrMe-etched samples are shown in Figure B.1.

For most of the PL spectrum, the difference in PL response between annealed and non-annealed samples is less than a factor of 5 and is not an appreciable change. Annealing

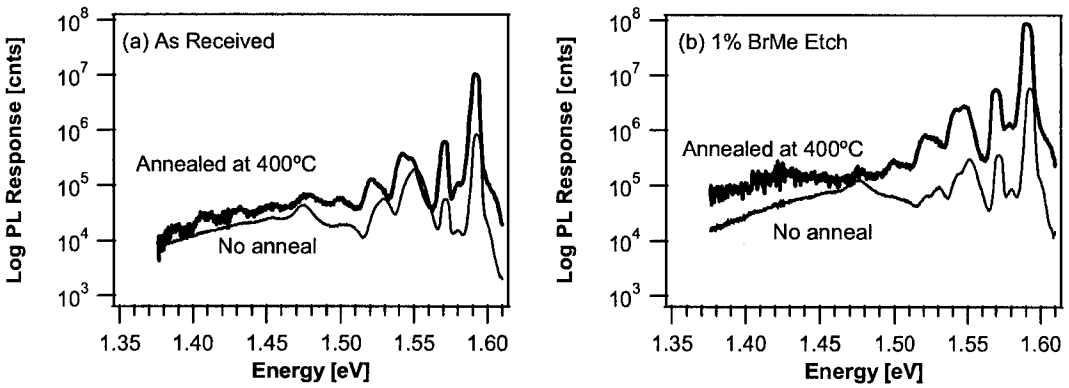

Figure B.1. Etching study samples: PL on (a) non-etched and (b) BrMe-etched crystalline CdTe. Both (a) and (b) were examined before and after a 400°C anneal in N_2.

increases the intensity of the near-band gap peaks by more than an order of magnitude. Annealing also shifts the position of the high-energy peaks in the non-etched samples, but does not introduce any new peaks in the low-energy PL spectrum. Additionally, the

N_2 anneal accentuates the phonon replicas of the peak at 1.475 eV, but the peak does not change its energetic location or increase significantly in intensity. It appears, then, that annealing does not significantly alter the zero-phonon energies of the low-energy PL. AFM data (Figure B.2) show that annealing at 400°C thermally etches the surface, enhancing the surface roughness. This change in surface roughness may help explain the changes in intensity and energetic location of the PL for excitonic and near-band gap transitions. The near-gap PL transitions are typically considered surface-dependent because any near-band edge photons created in the CdTe bulk have a high probability of either re-emitting or absorbing in the CdTe, hence a low probability of being collected in the PL signal. In contrast, transitions in the lower-energy portion of the PL spectrum will primarily come from the bulk, thus the different surfaces would not be expected to significantly affect this region of the PL. However, the surface morphology alone does not explain the increase in PL signal. To explore this phenomenon, the surface chemistry was also studied.

XPS was performed on CdTe single-crystal samples with no intentional Cu to examine the surface chemistry of the as-received sample, an etched sample, and a sputtered sample. For this experiment only, the 1% BrMe etch was performed for 10 s, rather than the standard 5 s etch used for all other sample preparation. The angle-resolved XPS is shown in Figure B.3a. It is clearly seen that the surface of the BrMe-etched sample is, indeed, Te-rich, but approaches stoichiometry below the surface. The sputtered sample is stoichiometric at the surface and into the crystal. The data also show that the surface of the as-received (non-etched) sample is Cd-rich. Sputter depth profiling XPS (Figure B.3b-c) shows the same trends. However, the two measurements give different values for the thickness of the Te-

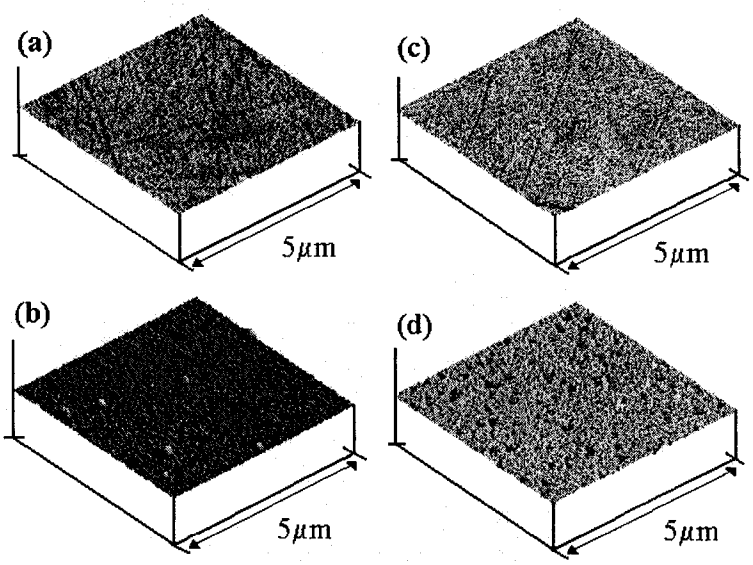

Figure B.2. AFM on single-crystal CdTe: (a) as received, (b) 1% BrMe etch, (c) as received with 400°C anneal, and (d) 1% BrMe-etched with 400°C anneal.

rich layer. The angle-resolved XPS indicates that the Te-rich layer is 30 Å thick, whereas the sputter-depth profiling XPS shows an 80 Å-thick Te-rich layer. The discrepancy in measured thickness likely results from the surface roughness. In the case of angle-resolved XPS, the surface roughness may affect the mean that the actual depth is different from the calculated depth, which assumes a smooth surface. In the case of sputter-depth profiling XPS, the sputtering process will be influenced by the initial surface roughness, such that some areas will sputter away more quickly than others. Since there will be errors between the actual and calculated depths for both procedures, the thickness of the Te-rich layer is likely intermediate to the two obtained values (30 and 80 Å).

The major differences in surface chemistry between etched and non-etched samples may explain why etching the single-crystal CdTe increases the overall PL intensity. Since the XPS results show that as-received CdTe has a Cd-rich surface and etched CdTe has a Te-

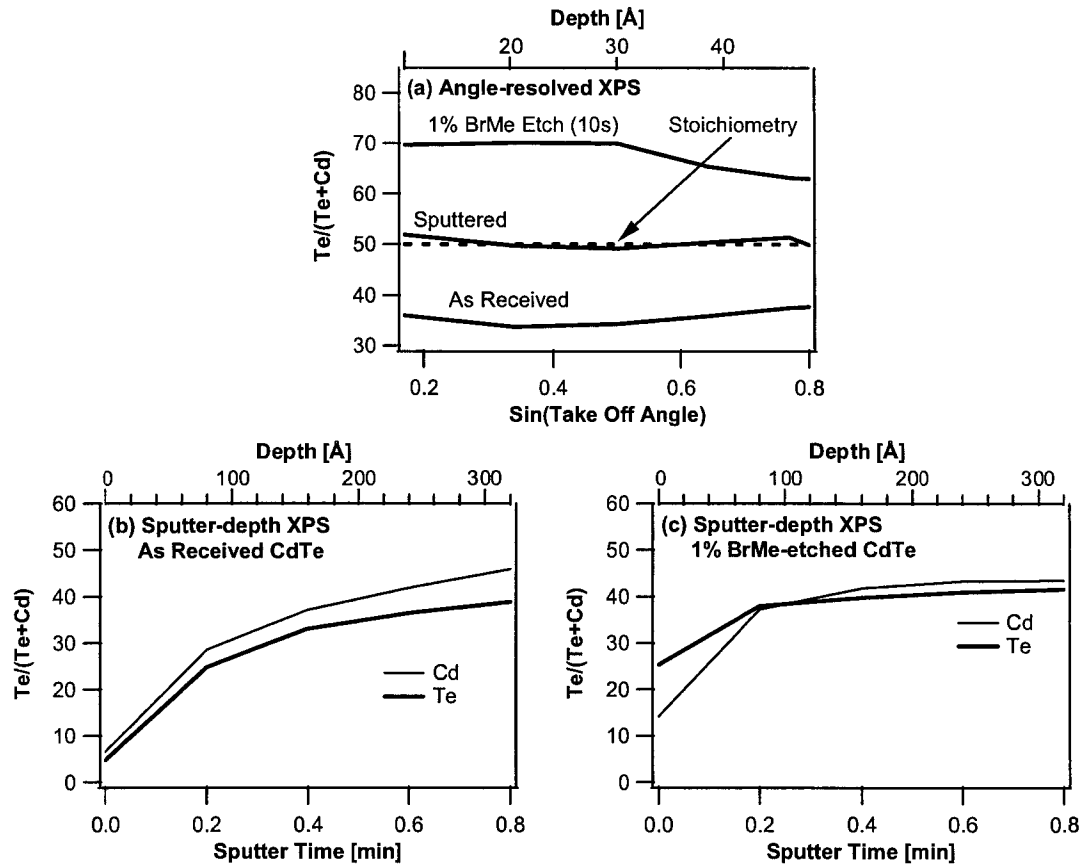

Figure B.3. XPS on as-received, BrMe-etched, and sputtered CdTe single crystals: (a) Angle-scanned XPS, (b) sputter-depth profiling XPS on as-received CdTe, and (c) sputter-depth profiling XPS on BrMe-etched CdTe.

rich surface, there is likely a difference in the surface Fermi levels due to surface pinning (see Figure B.4). The as-received CdTe crystal likely has a surface Fermi level that is pinned far above the valence band. Etching, which creates a Te-rich layer on the surface of the CdTe, would likely change the Fermi level only near the surface; the Fermi level would move from very far above the valence band to some level that is closer to, but still above, mid-gap. The surface Fermi level position and the Fermi level in the bulk determine the width of the depletion region. As suggested pictorially in Figure B.4, the depletion

region is expected to be smaller in the etched samples. In the depletion region, many light-generated electrons would be expected to recombine with light-generated holes rather than making PL transitions between defect states. Outside the depletion region, more of the light-generated electrons would be expected to make radiative transitions. Thus, the BrMe etching, which decreases the depletion region, would effective increase the number of radiative recombinations by increasing the area of the PL probe region where these types of transitions would be expected to occur.

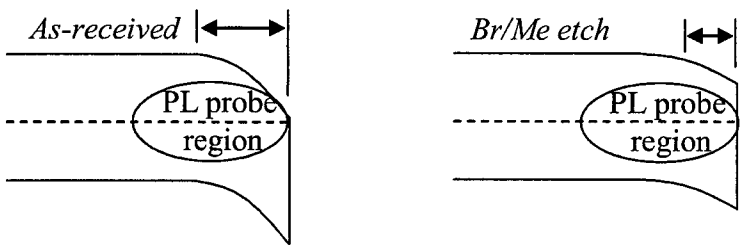

Figure B.4. Possible band alignment in as-received versus BrMe-etched crystalline CdTe.

REFERENCES

[1] G. A. Meehl et al., Science **307**, 1769 (2005).

[2] N. Lewis, The future of power and energy in the world, http://online.itp.ucsb.edu/onlin/colloq/lewis1, 2004.

[3] X. Wu et al., in *17th European PVSEC Vol. I*, page 995, Munich, Germany, 2001, WIP-Renewable Energies, ETA.

[4] J. Aranovich, D. Golmayo, A. L. Fahrenbruch, and R. H. Bube, J. Appl. Phys. **51**, 4260 (1980).

[5] R. H. Bube, A. Fahrenbruch, J. Aranovich, M. Chu, and K. Mitchell, J. Cryst. Growth **86**, 536 (1988).

[6] A. P. Belyaev, V. P. Rubets, and I. P. Kalinkin, Mater. Phys. Mech. **6**, 58 (2003).

[7] H. R. Moutinho, M. M. Al-Jassim, D. H. Levi, P. C. Dippo, and L. L. Kazmerski, J. Vac. Sci. Technol. A **16**, 1251 (1998).

[8] D. Bonnet and H. Rabenhorst, in *IEEE Photovolt. Spec. Conf.*, page 129, Silver Spring, MD, 1972, 9th IEEE PVSC.

[9] D. H. Rose et al., Prog. Photovoltaics **7**, 331 (1999).

[10] D. Rose, *The effect of oxygen on CdTe-absorber solar cells deposited by close-spaced sublimation*, PhD thesis, 1997.

[11] T. Potlog et al., Sol. Energy Mater. **80**, 327 (2003).

[12] H. R. Moutinho, R. H. Dhere, M. M. Al-Jassim, D. H. Levi, and L. L. Kazmerski, J. Vac. Sci. Technol. A **17**, 1793 (1999).

[13] S. A. Ringel, A. W. Smith, M. H. MacDougal, and A. Rohatgi, J. Appl. Phys. **70**, 881 (1991).

[14] H. R. Moutinho et al., in *Proc. Am. Vac. Soc.*, Baltimore, MD, 1998.

[15] J. Fritsche, A. Klein, and W. Jaegermann, Adv. Engin. Mater. **7**, 914 (2005).

[16] E. H. Rhoderick and R. H. Williams, *Metal-Semiconductor Contacts*, Clarendon Press, Oxford, 2nd edition, 1988.

[17] S. M. Sze, *Physics of Semiconductor Devices*, Wiley, New York, 1981.

[18] C. R. Crowell and S. M. Sze, Solid-State Electron. **9**, 1035 (1966).

[19] T. A. Gessert, C. L. Perkins, S. E. Asher, A. Duda, and M. R. Young, in *Mater. Res. Bull. Vol 769*, page 79, Boston, MA, 2004.

[20] T. A. Gessert, in *National CdTe Team Meeting Minutes*, Cocoa, FL.

[21] S. H. Wei, S. B. Zhang, and A. Zunger, J. Appl. Phys. **87**, 1304 (2000).

[22] N. Nakayama, H. Matsumoto, K. Yamaguchi, S. Ikegami, and Y. Hioki, Jpn. J. Appl. Phys. **15**, 2281 (1976).

[23] K. Kuribayashi et al., Jpn. J. Appl. Phys. **22**, 1828 (1983).

[24] T. A. Gessert, M. Romero, R. Dhere, S. Johnston, and A. Duda, in *3rd WCPEC*, Osaka, Japan, 2003.

[25] T. A. Gessert et al., in *31st IEEE PV Spec. Conf.*, page 291, Lake Buena Vista, FL, 2005.

[26] T. A. Gessert et al., in *IEEE 4th World Conf. PV Energy Conv.*, Waikoloa, HI, 2006.

[27] D. W. Niles et al., Prog. Photovoltaics **4**, 225 (1996).

[28] W. J. Danaher, L. Lyons, and G. Morris, Appl. Surface Sci. **22-23**, 1083 (1985).

[29] A. Rohatgi, R. Sudharsanan, S. A. Ringel, and M. H. MacDougal, Sol. Cells **30**, 109 (1991).

[30] K. D. Dobson, P. D. Paulson, B. E. McCandless, and R. W. Birkmire, in *Mater. Res. Bull. Vol 763*, page B2.1.1, San Francisco, CA, 2003.

[31] D. E. Aspnes and H. Arwin, J. Vac. Sci. Technol. A **2**, 1309 (1984).

[32] D. W. Niles, X. Li, P. Sheldon, and H. Hochst, J. Appl. Phys. **77**, 4489 (1995).

[33] M. A. Green, *Solar Cells*, Prentice-Hall, Englewood Cliffs, NJ, 1982.

[34] P. R. Gast, *Handbook of Geophysics*.

[35] A. Castaldini, A. Cavallini, B. Fraboni, P. Fernandez, and J. Piqueras, Appl. Phys. Lett. **69**, 3510 (1996).

[36] P. Y. Yu and M. Cardona, *Fundamentals of Semiconductors*, Springer, New York, 3rd edition, 2001.

[37] K. Zanio, *Semiconductors and Semimetals*, volume 13, Academic Press, New York, 1978.

[38] K. Boer, *Survey of Semiconductor Physics*, Van Nostrand Reinhold, New York, 1990.

[39] T. Schmidt, K. Lischka, and W. Zulehner, Phys. Rev. B **45**, 8989 (1992).

[40] S. Lany et al., Physica B **302-303**, 114 (2001).

[41] C. W. Tang and F. Vazan, J. Appl. Phys. **55**, 3886 (1984).

[42] D. Grecu, A. D. Compaan, D. Young, U. Jayamaha, and D. H. Rose, J. Appl. Phys. **88**, 2490 (2000).

[43] W. Stadler et al., Phys. Rev. B **51**, 619 (1995).

[44] J. Krustok, H. Collan, and K. Hjelt, J. Appl. Phys. **81**, 1442 (1997).

[45] J. Krustok, H. Collan, K. Hjelt, J. Madasson, and V. Valdna, J. Lumin. **72**, 103 (1997).

[46] G. Ascarelli and S. Rodriguez, Phys. Rev. **124**, 1321 (1961).

[47] K. Colbow and D. W. Nyberg, J. Phys. Chem. Solids **29**, 509 (1968).

[48] D. de Nobel, Philips Res. Repts. **14**, 361 (1959).

[49] D. de Nobel, Philips Res. Repts. **14**, 430 (1959).

[50] E. Molva, J. L. Pautrat, K. Saminadayar, G. Milchberg, and N. Magnea, Phys. Rev. B **30**, 3344 (1984).

[51] M. J. Romero, T. A. Gessert, and M. M. Al-Jassim, Appl. Phys. Lett. **81**, 3161 (2002).

[52] U. Pal, P. Fernández, and J. Piqueras, Mater. Lett. **23**, 227 (1995).

[53] J. P. Chamonal, E. Molva, and J. Pautrat, Solid State Comm. **43**, 801 (1982).

[54] D. P. Halliday, M. D. G. Potter, D. S. Boyle, and K. Durose, Mater. Res. Bull. Vol 668 , H1.8.1 (2001).

[55] D. P. Halliday, J. Eggleston, and K. Durose, J. Cryst. Growth **186**, 543 (1998).

[56] D. M. Hofmann et al., Phys. Rev. B **45**, 6247 (1992).

[57] A. Castaldini, A. Cavallini, B. Fraboni, P. Fernandez, and J. Piqueras, Mater. Sci. Eng. B **42**, 302 (1996).

[58] K. J. Price, in *Mater. Res. Bull. Vol 668*, page H1.7.1, San Francisco, CA, 2001.

[59] A. Zunger, Appl. Phys. Lett. **83**, 57 (2003).

[60] V. Valdna, J. Hiie, and A. Gavrilov, Solid State Phenomena **80**.

[61] J. V. Gheluwe, J. Versluys, D. Poelman, and P. Clauws, Thin Solid Films **481**.

[62] M. A. Hernandez-Fenollosa, D. P. Halliday, K. Durose, M. D. Campo, and J. Beier, Thin Solid Films **431-432**, 176 (2003).

[63] S. H. Wei and S. Zhang, Phys. Rev. B **66**, 155211 (2002).

[64] C. Persson, *Electronic structure of intrinsic and doped Silicon Carbide and Silicon*, PhD thesis, 1999.

[65] G. Kresse and J. Hafner, Phys. Rev. B **47**, 558 (1993).

[66] M. Gloeckler, *Device Physics of Cu(In,Ga)Se2 Thin-film Solar Cells*, PhD thesis, 2005.

[67] M. Gloeckler, A. L. Fahrenbruch, and J. R. Sites, in *3rd IEEE World. Conf. PV Energy Conv.*, Osaka, Japan, 2003.

[68] P. Rudolph and M. Muhlberg, Mater. Sci. Eng. B **16**, 8 (1993).

[69] G. Weigel et al., Mater. Sci. Eng. B **16**, 17 (1993).

[70] L. J. van der Pauw, Philips Res. Repts. **13**, 1 (1958).

[71] D. R. Lide, editor, *CRC Handbook of Chemistry and Physics*, CRC Press, Boca Raton, Florida, 76th edition, 1996.

[72] Y. Mahathongdy, Master's thesis, Colorado School of Mines, 1999.

[73] H. F. Schaake, J. H. Tregilgas, J. D. Beck, M. A. Kinch, and B. E. Gnade, J. Vac. Sci. Technol. A **3**, 143 (1985).

[74] S. Hildebrandt, H. Uniewski, J. Schreiber, and H. S. Leipner, J. Phys. (Paris) **7**, 1505 (1997).

[75] E. D. Palik, *Handbook of Optical Constants of Solids II*, Academic Press, San Diego, 2nd edition, 1998.

[76] J. L. M. K. M. James, J. D. Flood and C. E. Jones, J. Appl. Phys. **59**, 3596 (1986).

[77] J. Lee, N. C. Giles, D. Rajavel, and C. J. Summers, J. Appl. Phys. **78**, 5669 (1995).

[78] J. G. M.-A. M. C. O. Zelaya-Angel, M. Garcia-Rocha and J. Aguilar-Hernandez, J. Appl. Phys. **94**, 2284 (2003).

[79] J. S. K. Ohata and T. Tanaka, Jpn. J. Appl. Phys. **12**, 1641 (1973).

[80] Y. Yan, M. M. Al-Jassim, K. M. Jones, S.-H. Wei, and S. B. Zhang, Appl. Phys. Lett. **77**, 1461 (2000).

[81] P. Lefebvre et al., Phys. Rev. B **53**, 15440 (1996).

[82] P. M. Amirtharaj and N. Dhar, J. Appl. Phys. **67**, 3107 (1990).